

Important Notice

This copy may be used only for the purposes of research and private study, and any use of the copy for a purpose other than research or private study may require the authorization of the copyright owner of the work in question. Responsibility regarding questions of copyright that may arise in the use of this copy is assumed by the recipient.

UNIVERSITY OF CALGARY

9C-3D Modelling For Anisotropic Media

by

Ritesh Kumar Sharma

A THESIS

SUBMITTED TO THE FACULTY OF GRADUATE STUDIES
IN PARTIAL FULFILLMENT OF THE REQUIREMENTS FOR THE
DEGREE OF MASTER OF SCIENCE

DEPARTMENT OF GEOSCIENCE

CALGARY, ALBERTA

MAY, 2011

© Ritesh Kumar Sharma 2011

UNIVERSITY OF CALGARY
FACULTY OF GRADUATE STUDIES

The undersigned certify that they have read, and recommend to the Faculty of Graduate Studies for acceptance, a thesis entitled “*9C-3D Modelling For Anisotropic Media*” submitted by Ritesh Kumar Sharma in partial fulfillment of the requirements for the degree of MASTER OF SCIENCE.

Dr. Robert J. Ferguson
Supervisor, Department
of Geoscience

Dr. Larry Lines
Department of Geoscience

Dr. Elise Fear
Department of Electrical
and Computer
Engineering

Date

Abstract

Since multi-component modelling provides an improved image of a target horizon, I present a *9C-3D* numerical modelling approach for comparison with real seismic data, and synthetic data derived from fully elastic numerical methods. This modelling is posed in the slowness domain due to its advantages over the time domain. To accomplish this modelling, I extrapolate the known source wavefield from the surface to the reflector, multiply it by the reflection coefficient, and then extrapolate back to the surface. As the phase shift operator is prerequisite for performing this modelling, I compute the effective ray parameter that is used to obtain vertical slowness, an essential parameter in order to compute the phase shift operator. The presented modelling takes two data acquisition geometries into account. The first corresponds to micro-seismic and walk-away vertical seismic profiling (VSP) and the second corresponds to surface seismic methods. In order to obtain multi-component data, I build a rotation matrix based on azimuth and dip between the grid point and P-wave polarization vector. The implementation of this matrix on the extrapolated wavefield transforms the source polarization into the orientation of multi-component geophone and yields the multi-component data that can be used for analysis. Considering the first data acquisition geometry, the execution of the rotation matrix takes place before the reflection coefficient is multiplied. To execute the proposed modelling for the second data acquisition geometry, it is necessary to obtain the reflection (R) and transmission (T) coefficients in the plane wave domain. To do so, a normal for each individual plane wave based on the local velocity and vector cross product of this normal with the normal to the reflector are computed. This cross product yields a ray parameter that presently is used to compute corresponding R and T coefficients for a given plane wave.

For the sake of simplicity, I first consider isotropic media and follow the procedure de-

scribed in above paragraph for a known SH wavefield. By considering this case, I reveal a problem associated with the data acquisition geometry. Further, as seismic anisotropy plays an important role in exploration field, I perform the proposed modelling for transverse isotropic media (VTI: when axis of symmetry is vertical, HTI: when axis of symmetry is horizontal) in behalf of the generally occurrence of these media in geophysical exploration field. To continue a *9C-3D* modelling for anisotropic media, I obtain the R and T coefficients in plane wave domain for VTI and HTI media. Additionally, the influence of anisotropy on amplitude versus offset (AVO) analysis is also examined. For HTI media, I present two more approaches for avoiding the problems associated with the previously proposed modelling. According to the first approach, I use a relationship between the cosine of any angle with the horizontal axis and the angle of incidence considered with respect to vertical, and azimuth. Further, this relationship leads to the effective ray parameter for HTI media that is an essential component for the implementation of the proposed modelling. In the second approach, I solve the Christoffel equation for obtaining vertical slowness that is used to obtain the phase shift operator for the given media. Authentication of modelling is demonstrated in light of the physical modelling presented by another student of CREWES (Consortium for Research in Elastic Wave Exploration Seismology) for orthorhombic media.

Acknowledgements

First and foremost my heartfelt thanks and sincere gratitude to my supervisor, Dr. Robert J. Ferguson, for his constant guidance, help, timely advice and continuous encouragement all these years. I am grateful to the faculty, staff and students of CREWES (Consortium for Research in Elastic Wave Exploration Seismology) for their support. I would like to express my sincere thanks to Dr. Rob Vestrum for his valuable discussion and comments on this work. I would like thank to the sponsors of the CREWES and NSERC (Natural Science and Engineering Research Council of Canada) for their financial support of this work. I would also like to acknowledge the partial financial support from the Department of Geoscience through FGS (Faculty of Graduate Studies) summer scholarship.

I am indebted to my father (Mr. Surendera Sharma) and mother (Mrs. Usha Sharma) for their affection, encouragement and support. I am also indebted to my brother, Dr. Yogesh Sharma, who is always a constant source of motivation, support and encouragement. I also wish to acknowledge my friends, Mr. Tapes Tyagi and Mr. Ravindra Kumar, for being supportive to me at all time. I thank Mr. Irfan syed for his cooperation. I would like to thank Mr. Satinder Chopra and Mr. Somnath Mishra for their help in Calgary. Above all, I would like to thank the Almighty, for His kindness, grace and blessings throughout my career.

Table of Contents

Abstract	ii
Acknowledgements	iv
Table of Contents	v
List of Tables	vii
List of Figures	viii
1 Introduction	1
1.1 Role of seismic modelling in exploration	1
1.2 Seismic modelling methods	2
1.3 How to formulate RSM in plane wave domain	4
1.4 Importance of different models and multi-component seismic in seismic exploration	5
1.5 Consideration of data acquisition geometry	7
1.6 Organization of thesis	7
2 Plane wave reflection and transmission coefficients for SH-wave.	10
2.1 Summary	10
2.2 Plane wave domain approach to obtain the R and T coefficients	11
2.2.1 3D R and T coefficients for SH waves	13
2.2.2 Dipping interface problem	14
2.3 Examples	16
2.4 Conclusions	22
3 $9C$ - $3D$ modelling for VTI media.	25
3.1 Summary	25
3.2 Introduction	26
3.3 Wave propagation in transversely isotropic media	26
3.4 Theory	30
3.5 Examples	36
3.6 Conclusions	49
4 R and T coefficients in the plane wave domain for VTI media.	50
4.1 Summary	50
4.2 Introduction	51
4.3 R and T coefficients of SH wave for VTI media	52
4.4 Reflection and Transmission coefficients for P-SV wave	54
4.5 Example	58
4.6 Conclusions	75
5 Phase shift modelling for HTI media.	77
5.1 Summary	77
5.2 Introduction	78
5.2.1 Group velocity	79
5.3 Example	86
5.3.1 SV-case	96
5.4 Conclusions	101

6	Phase shift modelling with new proposed approaches.	103
6.1	Summary	103
6.2	Introduction	104
6.3	Theory	104
	6.3.1 First approach	104
	6.3.2 Second Approach	106
6.4	Example	107
6.5	Surface seismic data	108
	6.5.1 HTI media	110
6.6	Conclusions	112
7	Conclusions	118
A	Chapter2	125
A.1	To find the value of slowness at which reflected amplitude would be zero	125
A.2	Energy flux for reflected and transmitted waves	125
B	Chapter3	128
C	Chapter4	129
D	Chapter5	130
D.1	Methodology for obtaining analytic curves	130
E	Chapter6	135
F	Abbreviation and list of symbols	136

List of Tables

C.1	Model parameters for Class 1 AVO	129
C.2	Model parameters for Class 2 AVO	129
C.3	Model parameters for Class 3 AVO	129
D.1	Thomson's Parameters of a medium considered for P and SH waves propagation.	131
D.2	Thomson's Parameters of models considered for SV wave propagation. . .	131
E.1	Model parameters for HTI media	135

List of Figures

2.1	Schematic representation of unit normals to a plane wave and a horizontal interface, the angle of incidence θ_I is the angle between normal $\hat{\mathbf{p}}$ and $\hat{\mathbf{a}}$. $\mathbf{x}_1, \mathbf{x}_2$ are the horizontal coordinate axis and \mathbf{x}_3 is the vertical axis. . . .	12
2.2	Schematic representation of unit normals to a plane wave and a tilted interface, the angle of incidence θ_I is the angle between normal $\hat{\mathbf{p}}$ and $\hat{\mathbf{a}}$. $\mathbf{x}_1, \mathbf{x}_2$ are the horizontal coordinate axis and \mathbf{x}_3 is the vertical axis. . . .	15
2.3	a) Real part b) Imaginary part of reflection coefficient. c) Real part d) Imaginary part of transmission coefficient for a horizontal reflector. 512 in line and cross line traces are used.	17
2.4	a) In line slice b) Cross line slice of the reflection coefficient. c) In line slice d) Cross line slice of the transmission coefficient for a horizontal reflector. 512 in line and cross line traces are used	18
2.5	a) Real part b) Imaginary part of the reflection coefficient. c) Real part d) Imaginary part of the transmission coefficient for a dipping interface. 512 in line and cross line traces are used	19
2.6	a) In line slice b) Cross line slice of the reflection coefficient. c) In line slice d) Cross line slice of the transmission coefficient for a dipping interface. 512 in line and cross line traces are used	20
2.7	a) In line slice b) Cross line slice of reflection coefficient. c) In line slice d) Cross line slice of transmission coefficient for a horizontal interface. 512 in-line and 128 cross-line traces are used.	22
2.8	a) In line slice b) Cross line slice of the reflection coefficient. c) In line slice d) Cross line slice of the transmission coefficient for a horizontal interface. 512 in-line and 8 cross-line traces are used.	23
3.1	A hypothetical $3C$ geophone at a grid point . “I” represents the normal to an incident plane wave and azimuth is measured relative to y axis. Azimuth 0 indicates the in-line direction and the cross-line direction is characterized by 90°	32
3.2	Schematic representation of considered model and positioning of $3C$ geophones at reflecting surface. 1, 2, 3 and 4 describe the four quadrant of a circle whose periphery trace the azimuth from 0 to 360° and has y and x axis as horizontal and vertical axis, respectively.	35

- 3.3 (a) Registered energy versus offset (REVO) analysis of P-wave on H_1 component illustrate that H_1 component is more favorable for energy registration as offset increases. Polarity reversal appear on the either side of zero offset. (b) (REVO) analysis of P-wave on H_2 component illustrate that H_2 component is more favorable for energy registration near to zero offset. Polarity remains stationary on the either side of zero offset. (c) Recorded P-wave energy on vertical component demonstrate that energy registration on vertical component decreases with offset. Polarity follow the stationary behavior on either side of zero offset. 37
- 3.4 (a) Registered energy versus azimuth(REVA) analysis of P-wave at H_1 component indicates that energy registration increases as azimuth increases from 0 to 90. Polarity reversal occur on the either side of a line that bisects the circle along in-line direction. (b) REVA analysis of P-wave at H_2 component indicates that energy registration decreases as azimuth increases from 0 to 90. Polarity reversal occur on the either side of a line that bisects the circle along cross-line direction. (c) REVA analysis of P-wave on vertical component reveal the variation of recorded energy and polarity with azimuth. 39
- 3.5 (a) REVO of SV-wave on H_1 component. The Triplication phenomena occurs in this case. Registered energy decreases with offset. (b) REVO analysis of SV-wave on H_2 component demonstrate that a minuscule amount of energy is registered on H_2 component. (c) REVO analysis of SV-wave on V component indicates that a registered energy increases with offset. Polarity reversal does not occur on the either side of zero offset. 41
- 3.6 (a) In-line slice of the extrapolated SV wavefield by following the supportive approach and it is replica of that obtained by author and shown in (b) part. It shows the authentication of the triplication phenomena. 42
- 3.7 (a) REVA of SV-wave on H_1 component and more than one concentric circle is the counter part of the triplication. Polarity reversal occur on the either side of a line that bisects the circle along in-line direction. (b) REVA analysis of SV energy on H_2 component demonstrate that H_2 component is more favorable for energy registration in the in-line direction. (c) REVA analysis of SV-wave on V component indicates that energy registration on V component follows the stationary behavior. Polarity reversal occur on the either side of a line that bisects the circle along cross-line direction. 44
- 3.8 (a) REVO analysis of SH-wave energy on H_1 component indicates that a small amount of energy is registered on H_1 component. (b) REVO of SH-wave energy on H_2 component. Energy registration decreases with offset and polarity reversal occur on either side of zero offset. (c) Recorded energy of SH-wave on Vertical component and it is null in this case. 45

3.9	(a) REVA analysis of SH-wave energy on H_1 component indicates that energy registration decreases as azimuth increases from 0 to 90. Polarity reversal occur on either side of a line that bisect the circle along cross-line direction. (b) REVA of SH-wave energy on H_2 component. Energy registration increases with azimuth and polarity reversal occur on either side of a line that bisect the circle along in-line direction . (c) Recorded energy of SH-wave on Vertical component and it is null in this case. . . .	46
3.10	The arrival time of the SV- and SH- waves at a geophone located at (a) zero offset (b) medium offset (c) far offset. At medium offset SV energy is arriving at two times (expected, unexpected). The unexpected arrival time of SV energy is supported by the cusps in anisotropic media. The arrival time of the SH-wave is less than that of SV-wave at far offset. . .	47
3.11	The velocity variation of the SV- and SH-waves with the group angle. The velocity curve of the SV-wave shows the cusp phenomena and possesses multiple value at angle near by 45 degree in this case.	48
4.1	a) Real part of reflection coefficient. b) Imaginary part of reflection coefficient. c) Real part of transmission coefficient. d) Imaginary part of transmission coefficient, obtained from the anisotropic algorithm by applying constraint ($\gamma = 0$) on it.	59
4.2	a) Real part of reflection coefficient. b) Imaginary part of reflection coefficient. c) Real part of transmission coefficient. d) Imaginary part of transmission coefficient, obtained from the isotropic algorithm.	60
4.3	(a) The in-line (b) The cross-line slices of the SH wave R coefficients. (c) The in-line (d) The cross-line slices of the SH wave T coefficients. The red line denotes the coefficients obtained by degenerated anisotropic algorithm and the green line shows the isotropic coefficients. The overlapping of these curve endorse the efficacy of the anisotropic algorithm for isotropic media.	61
4.4	The variation of R coefficient with horizontal slowness for the different interfaces illustrates that anisotropy does have a considerable influence on the AVO analysis.	63
4.5	The influence of the Thomsen's parameter γ on the AVO analysis as shown in Figure 4.4 for different model.	63
4.6	(a) The real and imaginary part of the R coefficients for (a) P-P (b) S-S cases. The green line denotes the coefficients obtained by degenerated anisotropic algorithm and the red line shows the isotropic coefficients. The dotted black and magenta lines indicates the imaginary part of the R coefficients obtained by the degenerated anisotropic algorithm and isotropic algorithms, respectively. The overlapping of these curve endorse the efficacy of the anisotropic algorithm for isotropic media.	65
4.7	P wave reflection coefficients computed for three shale/gas-sand interfaces. The solid red lines indicate the exact solutions and the dashed green and black lines show the solutions computed by exact VTI and Rüger's approximated algorithms for isotropic medium, respectively.	67

4.8	The reflection coefficients curves of the P wave for the three models shown in appendix. The thick red line denotes the exact isotropic reflection coefficient, the dashed green and black lines show the exact and approximated reflection coefficients after introducing vertical transverse isotropy into the shale overburden with anisotropic parameters ($\delta = 0.12, \epsilon = 0.133$)	68
4.9	In order to seek the influence of the ϵ on the reflection coefficients, the same reflection coefficient curves of the P wave as the ones shown in Figure 4.8 but for a zero ϵ in the shale layer ($\delta = 0.12, \epsilon = 0$)	69
4.10	The same P wave reflection coefficient curves as shown previously in Figures 4.8 and 4.9 but for a VTI medium characterized by anisotropic parameters ($\delta = 0.12, \epsilon = 0.233$)	70
4.11	P wave reflection coefficient curves for the same three models but for a positive value of δ in the shale layer ($\delta = 0.24, \epsilon = 0.133$)	71
4.12	In order to seek the influence of the δ on the reflection coefficients, the same reflection coefficient curves of the P wave as the ones shown in Figure 4.11 but for a zero δ in the shale layer ($\delta = 0, \epsilon = 0.133$)	72
4.13	The same P-wave reflection coefficient curves as the ones shown in Figure 4.11, but for a negative value of anisotropy (negative δ in the overburden ($\delta = -0.24, \epsilon = 0.133$)	73
5.1	Schematic representation of HTI medium induced by vertical fractures where x axis is the axis of symmetry. The plane which possesses the axis of symmetry is known as symmetry axis plane and a plane normal to the symmetry axis plane is characterized by the isotropy plane (Nadri, 2009).	80
5.2	Schematic representation of the phase and group angles. The angle is measured with vertical axis. The group angle depicts the direction of energy propagation while phase angle determines the direction of wavefront propagation (Tsvankin:2001).	81
5.3	Schematic representation of the relationship between phase velocity and group velocity surfaces. The angles ψ and θ are the group and phase angles, respectively and are measured with horizontal axis. It illustrates that the group velocity surface can be constructed from the known phase velocity surface. Plane-wave fronts are the normal drawn from known points of the phase velocity surface to the group velocity surface and governs the energy distribution for a given direction (Nadri, 2009).	84
5.4	Schematic representation of the relationship between phase-velocity (solid red) and group-velocity (solid black) surfaces and slowness surface (dashed blue). This figure makes it possible to understand the reason for triplication on the SV wavefront (Grechka, 2009). The normals to the slowness-surface are shown by light and dark blue arrows. Red and brown arrows indicate the wavefront normals.	85

5.5	(a) In-line (b) Cross-line slice of extrapolated P wavefield through an anisotropic medium characterized by Thomsen's parameters shown in appendix. The considerable difference between these slices is observed kinematically as well as dynamically. Both slices manifest well known fact that P-wave travel fast in direction of strike with high amplitude.	88
5.6	Time slice of extrapolated P wavefield (a) without (b) with analytic curve. Obtained ellipse is a manifestation of azimuthal anisotropy as expected. More energy is observed in fast direction. The overlapping of the analytic curve (shown in red color) with the obtained ellipse illustrate authentication of proposed phase shift modelling.	88
5.7	(a) In-line (b) Cross-line slice of extrapolated P wavefield for same model as before but for a larger magnitude of anisotropy (higher $\delta=0.29$) in the medium. The large value of δ does have effect on the cross-line while the in-line slice is not influenced.	90
5.8	Time slice of the extrapolated P wavefield (a) without (b) with analytic curve. The large value of δ does have influence on the kinematic and dynamic behaviors of P wave.	90
5.9	(a) In-line (b) Cross-line slice of the extrapolated P wavefield for the same model as considered for above Figure but for large negative value of δ ($\delta=-0.2$). A considerable effect, kinematically as well as dynamically, of anisotropy is observed on the cross-line slice.	91
5.10	Time slice of the extrapolated P wavefield (a) without (b) with analytic curve for the same medium as considered in Figure 5.9. The authentication of the proposed modelling is demonstrated here as analytic curve is analogous to the obtained one.	91
5.11	Time slices of the extrapolated P wavefield (a) with (b) without analytic curve through the medium characterized by Thomsen's parameters chosen randomly. The unexpected behavior, kinematically and dynamically, illustrate that choice of Thomsen's parameters for a medium characterization can not be random.	92
5.12	(a)In-line (b) Cross-line slice of extrapolated SH wavefield for same model as considered in Figure 5.5 with low resolution. The difference, kinematically or dynamically, can not be examined precisely on behalf of these slices.	93
5.13	Time slice of the extrapolated SH wavefield (a) without (b) with analytic curve for same medium as ones shown in Figure 5.12 and demonstrate that SH wave travel fast in direction of fracture strike with high amplitude and illustrate the authentication of the proposed modelling.	93
5.14	(a) In-line (b) Cross-line slice of the extrapolated SH wavefield for the same model as considered above but of large anisotropy ($\gamma = 0.34$) and show the effect of anisotropy on propagation of the SH wavefield.	95
5.15	Time slices of the extrapolated SH wavefield through the same model as ones shown in Figure 5.14. The authentication of the proposed modelling is shown in (a) and (b) kinematically and dynamically, respectively.	95

5.16	(a) Registered energy versus offset (REVO) analysis of P-wave on H1 component illustrate that H1 component is more favorable for energy registration as offset increases. Polarity reversal appear on the either side of zero offset. (b) (REVO) analysis of P-wave on H2 component illustrate that H2 component is more favorable for energy registration near to zero offset. Polarity remains stationary on the either side of zero offset. (c) Recorded P-wave energy on vertical component demonstrate that energy registration on vertical component decreases with offset. Polarity follow the stationary behavior on either side of zero offset.	97
5.17	(a) Registered energy versus azimuth(REVA) analysis of P-wave at H1 component indicates that energy registration increases as azimuth increases from 0 to 90. Polarity reversal occur on the either side of a line that bisects the circle along cross-line direction. (b) REVA analysis of P-wave at H2 component indicates that energy registration decreases as azimuth increases from 0 to 90. Polarity reversal occur on the either side of a line that bisects the circle along in-line direction. (c) REVA analysis of P wave on vertical component reveal the variation of recorded energy and polarity with azimuth.	98
5.18	(a) In-line (b) Cross-line slice of the extrapolated SV wavefield for the same model as considered above for P and SH waves. The in-line slice is analogous to the cross-line slice	99
5.19	Time slices of the extrapolated SV wavefield through the same model as ones shown in Figure 5.18. The authentication of the proposed modelling is shown in (a) and (b) dynamically and kinematically, respectively. The obtained circle illustrate that anisotropy does not have a considerable effect on SV wave propagation.	99
5.20	Time slices of the extrapolated SV wavefield through model2 ($\epsilon > \delta$) as ones shown in Table D.2. The authentication of the proposed modelling is shown as analytic curve overlays with obtained one as shown in (a) and (b). There is no effect of anisotropy for this model.	100
5.21	Time slices (a) and (b) of the extrapolated SV wavefield through model3 with large magnitude of ($\epsilon > \delta$) shown in Table D.2. The authentication of the proposed modelling is shown in (b),kinematically. Still no effect of anisotropy is observed.	100
5.22	Time slices of the extrapolated SV wavefield through the model4 ($\epsilon < \delta$) shown in Table D.2. The cusps phenomena is occurred in the in-line direction. The occurrence of cusps is endorsed by the analytic curve but no overlapping of analytic curve with obtained one is noticed.	101
5.23	Time slices of the extrapolated SV wavefield through model5 ($-\delta$) shown in Table D.2. The cusps is observed near to 45°	102
5.24	Time slices of the extrapolated SV wavefield through the model possesses large negative value of δ (model6) as shown in Table D.2.	102

6.1	Schematic representation of an arbitrary angle α with the horizontal axis, and its associated angle of incidence(θ_I) and azimuth(ϕ)	106
6.2	In-line slice of the extrapolated wavefield (a) obtained by physical modelling. (b) obtained by proposed numerical modelling(second approach). The analogy of these slices authenticate the proposed modelling kinematically.	109
6.3	Cross-line slice of the extrapolated wavefield (a) obtained by physical modelling. (b) obtained by proposed numerical modelling(second approach). The analogy of these slices authenticate the proposed modelling, kinematically.	110
6.4	Data slice of the extrapolated wavefield along 45° azimuthal plane (a) obtained by physical modelling. (b) obtained by proposed numerical modelling(second approach). The analogy of these slices authenticate the proposed modelling, kinematically.	111
6.5	Data slice of the extrapolated wavefield along -45° azimuthal plane (a) obtained by physical modelling. (b) obtained by proposed numerical modelling(second approach). The analogy of these slices authenticate the proposed modelling, kinematically.	112
6.6	The juxtaposition of the in-line slices of the extrapolated wavefield obtained by (a) second approach (b) first approach manifests the analogy of these slice and endorse to the first approach in light of the second approach.	113
6.7	The cross-line slices of the extrapolated wavefield using (a) second approach (b) first approach are analogous to each other and demonstrate the authentication of the first approach too.	113
6.8	(a) Monochromatic extrapolated wavefield in plane wave domain at the reflector. (b) Monochromatic reflection coefficient as a function of horizontal slowness component.	114
6.9	(a) Cross-line slice (b) In-line slice of the extrapolated wavefield at the surface before rotation matrix is applied on it. Registered energy decreases with offset.	115
6.10	(a) Registered energy versus azimuth(REVA) analysis of P-wave at H1 component of $3C$ geophones situated at the surface, indicates that energy registration increases as azimuth increases from 0 to 90. Polarity reversal occur on the either side of a line that bisects the circle along in-line direction. (b) REVA analysis of P-wave at H2 component indicates that energy registration decreases as azimuth increases from 0 to 90. Polarity reversal occur on the either side of a line that bisects the circle along cross-line direction. (c) REVA analysis of P-wave on vertical component reveal the variation of recorded energy and polarity with azimuth.	116
6.11	The obtained P-wave reflection coefficient along symmetry axis and normal to it. The black and blue colors indicate the results obtained numerically while red and green colors are corresponding to Ruger’s approach. . . .	117

Chapter 1

Introduction

In this chapter, I will start from the role of seismic modelling in the exploration field, then I will discuss the available methods for seismic modelling. The reason I have selected the plane wave domain is also described in this chapter. How I accomplish the proposed modelling in the plane wave domain, is also described in the current chapter. Further, this chapter illustrates the importance of chosen models for present modelling. I finish by demonstrating the considered data acquisition geometry and providing an outline of thesis.

1.1 Role of seismic modelling in exploration

In seismic exploration, the main objective of the geo-scientist is to link the geology to seismology. To do so, seismic modelling is one of the basic tools (Benxi et al., 2009). Traditionally, seismic data and data from another sources are used to derive an indirect description of a potential reservoir. Forward (seismic) modelling is a key to success to an explorationist as it aids one in relating what one sees in the seismic data to what one expects to see, based on the assumed geological model (Cameron et al., 1984). In general, forward modelling is used to compare the seismic response of a given geological model with actual data and the try to improve the match between these both data until an acceptable level of accuracy is obtained (Sayersi and Chopra, 2009). Further, the importance of forward modelling resides in the fact that it is employed to design the seismic acquisition parameters, improve the seismic processing approaches and validate the seismic interpretation (Anderson and Cardimona, 1995). It is used to simulate the

seismic field from the sources to scatters to receivers and generate the seismic records.

1.2 Seismic modelling methods

Physical modelling is an effective method to generate a seismic response using a laboratory scale model (Cooper et al., 2007). Considering the inconvenience and cost of a field survey, it may be feasible to design and conduct a small seismic survey in the lab. The assumption underlying the physical modelling is that scale models are built using a real material with the same elastic properties as those of true geologic formations in the Earth (Yang, 2003). After constructing a model, a source (a piezoelectric transducer), is used to emit the seismic energy into the model, and the reflected wave-field is recorded by receiver. The recorded data can then be processed and analyzed to compare with the real field data. Historically, physical modelling was used because of a lack of adequate computing technology for numerical modelling. The limitation of physical modelling resides on the fact that the lab materials can not be exactly the same as the real sediments.

In numerical modelling one attempts to solve the wave equation for simulating wave propagation in different media. Typically, numerical modelling methods are intended to solve the partial difference equation by considering boundary and initial conditions (Krebes, 2004). There are a number of numerical forward modelling methods available and the choice of methods depends on a tradeoff between the accuracy necessary and the desired computing time. Generally, the method that should be used is dictated by the type of data to be modelled throughout, the aspects of the data that need to be accurately modeled and the complexity of the model (Mellmani and Kunzinger, 1992). Ray tracing and wave equation methods are two classes of seismic modelling. Ray tracing methods are limited as these methods work for sufficiently smooth models whereas we encounter with complex models in reality. This limitation can be overcome by using

the wave equation methods that solve the propagation problem over the entire model (Mellmani and Kunzinger, 1992). In this regard, there are many existing wave equation solvers such as Kirchhoff and Born integral methods, finite-difference and finite-element methods, and depth exploration method in frequency space domain (Benxi et al., 2009). Although, finite difference methods can provide very accurate results in the most complex media, these methods have limitations imposed by computing time that is high in two dimensions and very high in three dimensions (Mellmani and Kunzinger, 1992).

Two methods, namely, Rayleigh Sommerfeld(RS) and Kirchhoff methods (Cooper et al., 2008) have been adopted for forward modelling throughout in seismic exploration. Both of these methods originated from optical diffraction theory (Ersoy, 2007).

Rayleigh Sommerfeld Modelling (RSM) is known as a 3D modelling technique and is treated as an alternative to better known modelling techniques such as finite difference and Kirchhoff (Margrave and Cooper, 2007). This modelling provides a high-frequency seismic response that includes diffractor patterns. RSM can be more efficient than Kirchhoff modelling because it operates in frequency-wavenumber domain. In terms of computational time, RSM takes $O(N \log N)$ computing time while Kirchhoff modelling takes $O(N^2)$ for 3D models (Cooper et al., 2008). In the past RSM was used to produce very high frequency response but with no multiples, surface waves. Additionally, RSM was limited to laterally but angle independent R and T coefficient. This work was elaborated by Cooper and Margrave (2008) for RSM with AVO in order to produce a high frequency seismic response that includes diffraction effects. By doing so the objective in modelling in stratigraphic setting is obtained. To accomplish this work, ray tracing was used to compute incident angle at reflecting interface. Presently, an approach is proposed for RSM with AVO in the plane wave domain.

1.3 How to formulate RSM in plane wave domain

Basic geometry and result of Rayleigh-Sommerfeld theory are described by (Margrave and Cooper, 2007). Following this description, Rayleigh Sommerfeld modelling (RSM) can be described in three major steps: 1) Extrapolation of source wave field from the source to a datum reflector. 2) Multiplication of the extrapolated wavefield in step (1) with a reflectivity function 3) Extrapolation of step (2) back to the surface. Presently, an approach of going from spatial frequency domain into plane wave domain without $\tau - p$ transformation, is described. The preceding argument describes the importance of this approach in order to derive RSM in the plane wave domain.

It is known that wavefield extrapolation in the $x - t$ domain involves two dimensional convolution (Berkhout, 1982). Time can be replaced by temporal frequency or angular frequency ω and now convolution, in one dimension only, is involved in the extrapolation process. The space variable x is replaced by the spatial frequency variable k_x by a second Fourier transformation and only multiplication is involved for extrapolation in the $k_x - \omega$ domain. Now, an approach is invoked at this place in order to transform the wavefield from $x - \omega$ domain into plane wave domain.

A monochromatic wavefield can be transformed from space domain into spatial frequency domain as

$$\varphi(\vec{k})_{\omega} = \int \Psi(\vec{x})_{\omega} e^{(i\vec{k} \bullet \vec{x})} d\vec{x}, \quad (1.1)$$

where \bullet is the dot product. Equation (1.1) can be written as

$$\varphi(\vec{k})_{\omega} = \int \Psi(\vec{x})_{\omega} e^{(i\omega \frac{\vec{k}}{\omega} \bullet \vec{x})} d\vec{x}, \quad (1.2)$$

now using relation $\vec{k} = \omega \vec{p}$, where \vec{p} is the slowness vector equation (1.2) is written as

$$\varphi(\vec{p})_{\omega} = \int \Psi(\vec{x})_{\omega} e^{(i\omega \vec{p} \bullet \vec{x})} d\vec{x}. \quad (1.3)$$

Thus using equations (1.1), (1.2), (1.3) a monochromatic wavefield can be described in the plane wave domain without using $\tau - p$ transformation.

The importance of this approach in RSM is described presently. According to Rayleigh Sommerfeld diffraction theory the source wavefield at any observation point can be described as (Margrave and Cooper, 2007)

$$\Psi(x = P) = \frac{1}{4\pi} \int_s \Psi_0(\vec{x}_s) W(\vec{x}_p - \vec{x}_s) \rho(s) ds, \quad (1.4)$$

where P is the observation point and $\vec{x}_p = (x_p, y_p, z_p)$, $\vec{x}_s = (x_s, y_s, z_s)$ are the coordinates of the screen (reflector) and observation point, respectively. W is the z derivative of the Green's function, $\rho(s = (x_s, y_s))$ is the reflectivity function and $d_s = d_x d_y$. Since equation (1.4) is convolution, it can be described in Fourier domain (Margrave and Cooper, 2007) as

$$\Psi(x) = \frac{1}{4\pi} \int_s \hat{W}(k_x, k_y, z_p - z_s) \hat{\Psi}_0 \rho(k_x, k_y, z_s) e^{ik_x x + ik_y y} dk_x dk_y. \quad (1.5)$$

where 'hats' indicate 2D Fourier transform over x and y . As per equation (1.5) Rayleigh Sommerfeld modelling is just phase shift migration backwards (Margrave and Cooper, 2007).

It is revealed from the above equations that Fourier transformation takes place in RSM. Now using transformation by equations (1.1), (1.2), and (1.3), RSM can be described in plane wave domain. Further, to accomplish the RSM it is necessary to obtain the reflection and transmission coefficients in plane wave domain.

1.4 Importance of different models and multi-component seismic in seismic exploration

In seismic modelling, it is extremely important that we know how to synthesize a seismic response that is as close as possible to what we measure in the real world (Anderson

and Cardimona, 1995). Historically, Earth was treated as isotropic media for the sake of simplicity but increasing demand for oil in world compels geoscientists for considering the complexity of Earth. In reference to this, anisotropic models represents the Earth at its most complex and play an important role in oil and gas exploration field in order to improve the image of a target horizon (Grechka, 2009). Thus, it is reasonable to expect anisotropic models to become the norm in future exploration. On considering anisotropy, the anisotropic models discussed presently are transverse isotropy with a vertical axis of symmetry (VTI media), used to describe thinly layered media and shale sequences (Thomsen, 2002), and with a horizontal axis of symmetry (HTI media). Conventional seismic surveys record primarily P-waves using vertical component geophones while multicomponent seismic surveys record compressional and shear waves using multicomponent geophones. Once the multicomponent data is recorded, the processing of this data is the next step and it may be several times more intensive than conventional P-wave analysis. The reward of this great effort is an improved understanding of the subsurface image. Using multicomponent seismic, there have been encouraging results in imaging through gas-obscured areas, finding sand-rich zones in clastic sequence, and determining fractures zones and orientations (Chopra and Stewart, 2010). Beyond these, multicomponent measurements provide improved imaging, direct hydrocarbon and lithology indication in the exploration stage, and facilitates improved reservoir illumination and characterization in development stage (Hardage, 1983). Thus, considering the importance of multicomponent seismic, presently *9C-3D* modelling has been taken into account.

1.5 Consideration of data acquisition geometry

In order to perform the forward modelling, the relationship between the seismic sources and receivers must be known. Presently, two major data collection geometries have been taken into account for the proposed modelling. The surface seismic method, which includes the reflection method in which both seismic sources and receivers reside on the surface, is the first data collection geometry. The second geometry is used to measure seismic wavefield directly at the reflecting interface while the source is at the surface. This can be referred to walk-away vertical seismic profiling or VSP and can be used for Micro-seismic modelling.

1.6 Organization of thesis

The thesis proceeds as:

- As it is required to obtain R and T coefficients in the plane wave domain for accomplishing RSM in that domain, Chapter 2 is devoted to isotropic media and demonstrates how to obtain R and T coefficients in the plane wave domain for SH wave field for the sake of simplicity. This chapter yields the basic concept behind the way of determining an effective ray parameter that is used for obtaining R and T coefficients in the plane wave domain. The problem of a special case of dipping interface has been solved in current chapter. As forward modelling plays an important role to design the seismic acquisition parameters, the problem associated with data acquisition is also revealed.
- Chapter 3 describes the implementation of our proposed $9C-3D$ modelling for VTI media. This Chapter introduces the method of building rotation matrix that is based on azimuth and dip between the grid point and polarization vector of P-

wave source and is applied on the extrapolated wavefield for obtaining the multi-component data. The acquisition geometry for the multi-component data, and registered energy versus offset and azimuth (REVO,REVA) analysis of a known surface seismic source has been revealed in this chapter.

- In Chapter 4, I obtain the R and T coefficients in the plane wave domain at a boundary between two transverse anisotropic media with the vertical axis of symmetry (VTI) due to the importance of these coefficients for numerical computations. As Thomsen's parameters are essential for understanding the seismic waves signature in anisotropic media, the way of describing R and T coefficients in terms of these parameters by following Graebner's approach, has been delineated in current chapter. Further, as the dependency of the reflected waves amplitude on offset has proven to be a valuable exploration tool for direct hydrocarbon detection, I have demonstrated the influence of anisotropy on P-wave reflectivity by considering the three models characterized by the Class 1, 2 and 3 type of Gas-sand anomaly in this chapter. A test of accuracy of the popular Rüger's approximation is also delineated here.
- Fractures play an important role in hydrocarbon production as they determine the pathways and volume of crustal fluid movement. The horizontal transverse isotropic (HTI) is the simplest effective model of a formation that contain a single fracture system. Further, in the continuation of $9C-3D$ modelling for VTI medium, I present phase shift modelling for HTI medium by considering the first data acquisition geometry in order to seek the dynamic and kinematic signature of the seismic waves in HTI media. These analysis can be useful for fracture analysis. This modelling is delineated in Chapter 5. However, in order to perform seismic modelling for HTI media while considering the surface data acquisition geometry, I have implemented

constraint by using only P-wave in my studies. This constraint depends on the fact that compressional data generally have better quality and are cheaper to acquire and process than shear wave data.

- In order to perform phase shift modelling for HTI media, I have implemented a constraint on a layer of infinitesimal thickness above the HTI media that its velocity is the maximum velocity of the lower HTI medium. To avoid this constraint, I have presented two more approaches and these are described in Chapter 6. According to first approach, I use the relationship between the cosine of any angle with the horizontal axis and the angle of incidence considered with respect to vertical and azimuth. This relationship yields the effective ray parameter for HTI media. After obtaining this parameter the vertical slowness is computed using Thomsen's parameters of equivalent VTI media of HTI media and effective ray parameter. In the second approach, I solve the Christoffel equation for obtaining vertical slowness that is used to obtain the phase shift operator for anisotropic media. Following the second approach, I have described seismic modelling for an orthorhombic media to test the accuracy of my modelling in reference to the physical modelling presented by another student of CREWES. Further, numerical method of calculating the R and T coefficients in the plane wave domain for HTI and orthorhombic media is discussed in this chapter.
- Chapter 7 summarizes the conclusions of all chapters.

Chapter 2

Plane wave reflection and transmission coefficients for SH-wave.

2.1 Summary

The calculation of R and T coefficients at any interface is an important problem of elastodynamic theory. Historically, the R and T coefficients have been obtained in several domains according to their importance. It is known that for the isotropic case the R and T coefficients depend on the acoustic impedance contrast and angle of incidence. The angle of incidence can be computed by using cross product of two known unit normals. In this approach, derived R and T coefficients will be in the plane wave domain. By deriving R and T coefficients in the plane wave domain for 3D media, determination of the dip and azimuth of the interface are avoided, and thereby, we avoid ray tracing and exposure to caustics especially in anisotropic media. The problem that I solve, in this regard, is problem of a special case of dipping interface and how to rotate the plane wave coordinate system from that determined by the computational grid, and the system determined by a dipping interface. Classical R and T coefficients in the plane wave coordinates are worked out for reflectors aligned with the computational grid. For non-aligned reflectors, those with dip and azimuth, computation of effective R and T coefficients is not straight forward, for this the coordinate system must be rotated. To do this, a normal for each individual plane wave based on the local velocity and vector cross product of this normal with the normal to the reflector are computed. This cross product yields a ray parameter that presently is used to compute the corresponding R and T coefficients for a given plane wave. The importance of this approach is the automatic adaptation of the R and T coefficients expression to the special case of a

dipping interface. These coefficients can then be used to scale the amplitude component of plane wave extrapolation across a reflector as is done in seismic forward modelling. Another importance of the R and T coefficients in the plane wave domain, is their use in Rayleigh Sommerfeld Modelling(RSM) of seismic data. In line and cross line traces are required in order to model the plane wave inputs. Presently, the problem associated with data acquisition is studied here by changing the number of cross line traces. Further, it reveals the problem associated with data acquisition and the requirement of proper data acquisition.

2.2 Plane wave domain approach to obtain the R and T coefficients

Historically, the calculation of R and T coefficients for plane waves on a free surface and at a welded contact interface was obtained by Zeoppritz (Borejko, 1996). This work was elaborated by Aki and Richards (Aki and Richards, 1980). The analytic expressions of the R and T coefficients are known in term of the incident angle. The angle of incidence is the angle, that of the incident and scattered plane make with the normal to the plane reflector. The plane of incidence can be represented by the unit normal vector to the plane wave in the propagation direction and can be computed as (Ferguson and Margrave, 2008)

$$\hat{\mathbf{p}} = \frac{p_1 \hat{\mathbf{i}} + p_2 \hat{\mathbf{j}} + q \hat{\mathbf{k}}}{\sqrt{p_1^2 + p_2^2 + q^2}}, \quad (2.1)$$

where p_1, p_2 are the input plane wave parameters and q is the vertical slowness in the incident medium. p_1, p_2, q are coupled according to a relation derived from the dispersion relation as

$$q = \frac{1}{v} \sqrt{1 - (vp_1)^2 - (vp_2)^2}. \quad (2.2)$$

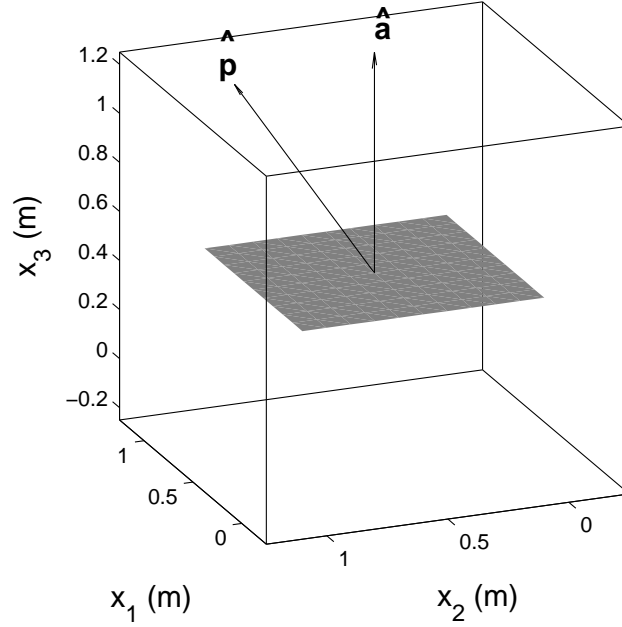


Figure 2.1: Schematic representation of unit normals to a plane wave and a horizontal interface, the angle of incidence θ_I is the angle between normal $\hat{\mathbf{p}}$ and $\hat{\mathbf{a}}$. \mathbf{x}_1 , \mathbf{x}_2 are the horizontal coordinate axis and \mathbf{x}_3 is the vertical axis.

where v is the velocity of the incident medium. The unit normal associated with a reflecting subsurface plane can be computed as

$$\hat{\mathbf{a}} = \sin \theta_a \cos \phi_a \hat{\mathbf{i}} + \sin \theta_a \sin \phi_a \hat{\mathbf{j}} + \cos \theta_a \hat{\mathbf{k}}. \quad (2.3)$$

where θ_a is the dip and ϕ_a is the azimuth of the normal to the interface. These two unit normals are shown in Figure 2.1. This Figure shows two unit normal vector, $\hat{\mathbf{p}}$, normal to the plane wave in the propagation direction, and $\hat{\mathbf{a}}$, is the normal to the horizontal interface shown by shaded plane. Now, following simple vector calculus, the cross product of these two unit normal vectors is used to obtain the angle of incidence θ_I as

$$\sin \theta_I = |\hat{\mathbf{p}} \times \hat{\mathbf{a}}|, \quad (2.4)$$

The sine of the angle of incidence is related to the slowness along the interface as

$$p_I = \frac{\sin\theta_I}{v} = |\hat{\mathbf{p}} \times \hat{\mathbf{a}}| \sqrt{p_1^2 + p_2^2 + q^2}. \quad (2.5)$$

where p_I is the slowness along the interface (ray parameter). Thus, the angle of incidence is obtained according to equation (2.4). After obtaining the angle of incidence from equation (2.5), this value is substituted in the known analytic expression (Kennett, 2001) in order to obtain the R and T coefficients in the plane wave domain.

2.2.1 3D R and T coefficients for SH waves

It is known that evaluating the R and T coefficients is beneficial to interpret the field records for lithology, fluid content etc by generating synthetic seismograms (Upadhyay, 2004). Incident, reflected, and transmitted plane P- and S- waves make a pertinent system. The assumption of two dimensional plane waves ensures our discussion for two separate groups of waves (Slawinski, 2003). These groups are the coupled P- and SV-waves, and the SH- wave. The analytical expression of the R and T coefficients for three dimensional plane waves in elastic media were given by Borejko (Borejko, 1996). Generalized ray- integral representation of pertinent waves were illustrated in that paper. Generalized ray integral representation of SH-wave for dipping structure was given by Zieger and Pao (Pao et al., 1984). Further, assuming isotropy, the standard ‘2D’ formulas (Krebes, 2004) can be used for any plane reflector regarding its 3D orientation. According to seismic reflection theory, when an incident plane wave encounters the discontinuities in the properties at a horizontal interface between two homogeneous layers, there both the phenomenas: reflection from the boundary and transmission through the boundary take place. The boundary conditions, the continuity of displacement and traction, are considered at the boundary to obtain the amplitude information of reflected and transmitted waves. After applying these boundary conditions, R and T coefficients for SH-wave are

known in terms of the angle (Krebes, 2004). These expressions are transformed into plane wave coordinates by estimating the angle of incidence using equation (2.5) and written as

$$R_{SH} = \frac{\rho_1 v_1^2 q_1 - \rho_2 v_2^2 q_2}{\rho_1 v_1^2 q_1 + \rho_2 v_2^2 q_2}, \quad (2.6)$$

and

$$T_{SH} = \frac{2\rho_1 v_1^2 q_1}{\rho_1 v_1^2 q_1 + \rho_2 v_2^2 q_2}, \quad (2.7)$$

where ρ_1, v_1 are the density and velocity of the incident medium, respectively. ρ_2, v_2 are the density and velocity of the refracted medium, respectively and q_1 is described as

$$q_1(\vec{p}) = \frac{1}{v_1} \sqrt{1 - (v_1 p_I)^2}, \quad (2.8)$$

and q_2 is described as

$$q_2(\vec{p}) = \frac{1}{v_2} \sqrt{1 - (v_2 p_I)^2}. \quad (2.9)$$

2.2.2 Dipping interface problem

The above expressions of the R and T coefficients can be used for the special case of a dipping interface. In this case, the normal to the interface (see the Figure 2.2) would be different from the horizontal one and can be computed from equation (2.3). Figure 2.2 shows the tilted interface where $\hat{\mathbf{a}}$ is normal to this interface. An assumption, that the normal to the interface lies in plane of propagation, is considered here. This constraint is applied to equation (2.3). This assumption ensures that SH wave is still decoupled from P and SV waves (Sten and Wyssession, 2002). Now, the ray parameter for each individual plane wave is computed according to equation (2.5) and used in equations (2.6) and (2.7) in order to obtain the R and T coefficients for dipping interface, respectively.

In-line and cross-line slices of the R and T coefficients can be obtained using $p_2 = 0$, $p_1 = 0$, respectively. Recalling equation (2.5) for $p_2 = 0$, the ray parameter is the same as horizontal slowness (p_1) in the 2D case and for $p_1 = 0$ it would be p_2 . Further, in-line

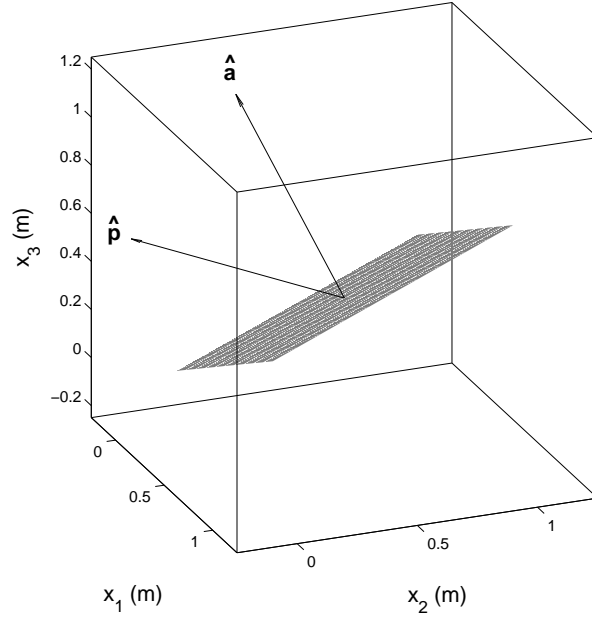


Figure 2.2: Schematic representation of unit normals to a plane wave and a tilted interface, the angle of incidence θ_I is the angle between normal $\hat{\mathbf{p}}$ and $\hat{\mathbf{a}}$. \mathbf{x}_1 , \mathbf{x}_2 are the horizontal coordinate axis and \mathbf{x}_3 is the vertical axis.

and cross line R and T coefficients can be obtained using equations (2.6) and (2.7) with different q_1 and q_2 from equations (2.8) and (2.9). These equations are deduced and given as

$$q_1(\vec{p}) = \frac{1}{v_1} \sqrt{1 - (v_1 p_1)^2}, \quad (2.10)$$

and

$$q_2(\vec{p}) = \frac{1}{v_2} \sqrt{1 - (v_2 p_1)^2}, \quad (2.11)$$

for the in-line, and

$$q_1(\vec{p}) = \frac{1}{v_1} \sqrt{1 - (v_1 p_2)^2}, \quad (2.12)$$

and

$$q_2(\vec{p}) = \frac{1}{v_2} \sqrt{1 - (v_2 p_2)^2}. \quad (2.13)$$

for the cross line.

For the zero slowness, the R and T coefficients are the same for both the in-line and

cross line cases and are independent of frequency. These are given as

$$R_{SH} = \frac{\rho_1 v_1 - \rho_2 v_2}{\rho_1 v_1 + \rho_2 v_2}, \quad (2.14)$$

and

$$T_{SH} = \frac{2\rho_1 v_1}{\rho_1 v_1 + \rho_2 v_2}. \quad (2.15)$$

respectively.

2.3 Examples

Now to explore the R and T coefficients change with p_1 and p_2 for a horizontal reflector, an example in which $v_1 = 1500m/s$ and $v_2 = 2500m/s$ with the same density across the reflector is considered. Figure 2.3 shows the schematic representation of the 3D real and imaginary part of the R and T coefficients, respectively obtained from equations (2.6) and (2.7). Presently, 512 in line and cross line traces have been taken into account for a particular frequency of 40Hz. Considering the equations from (2.10) to (2.13), the in line and the cross line slices of the R and T coefficients are shown in Figure 2.4. At zero slowness, the R and T coefficients attain the values as expected. As horizontal slowness increases to larger values, the amplitude of the transmitted wave increases and the reflected amplitude approaches zero. Recalling equation (2.6), the reflected amplitude would be zero when horizontal slowness p_1 is equal to $1/\sqrt{v_1^2 + v_2^2}$ (see the appendix A for mathematical manipulation). Despite crossing a significant change in velocity, there is no reflected wave for a plane wave at this horizontal slowness while the transmitted wave has amplitude 1. Further, as the slowness value increases beyond to this particular slowness, the amplitude of transmitted wave continues to increase. This amplitude of the transmitted wave increase due to an increase in the horizontal orientation of the transmitted wave. At the critical slowness, the transmitted wave would be horizontal. This implies that the vertical slowness in the second medium will be zero. According

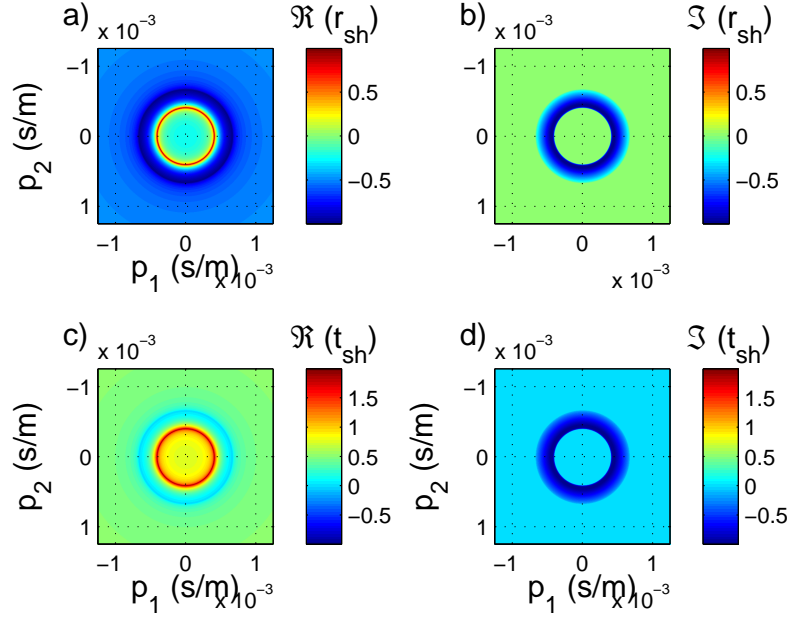


Figure 2.3: a) Real part b) Imaginary part of reflection coefficient. c) Real part d) Imaginary part of transmission coefficient for a horizontal reflector. 512 in line and cross line traces are used.

to equation (2.11), this occurs at $p_1 = 1/v_2 = 0.0004\text{s/m}$. At this value of slowness, the amplitude is 2 for the transmitted SH wave and 1 for reflected wave. Beyond the critical slowness, there is no transmitted wave in the lower layer and q_2 is imaginary in this situation. They are known as evanescent waves and their amplitudes decay with depth. Due to the imaginary vertical slowness, the reflection and transmission coefficients become complex beyond the critical slowness. Once the coefficients become complex, the shape of the reflected pulse and transmitted pulse is modified (Kennett, 2001). Following this theory, there will be a distortion of the reflected and transmitted pulses at $p_1 > 1/v_2$ as depicted in Figure 2.4. Further, cross-line slices of the R and T coefficients can be describe in light of the above description of the in-line slices.

Considering a dipping interface, Figure 2.5 shows the real and imaginary part of the 3D

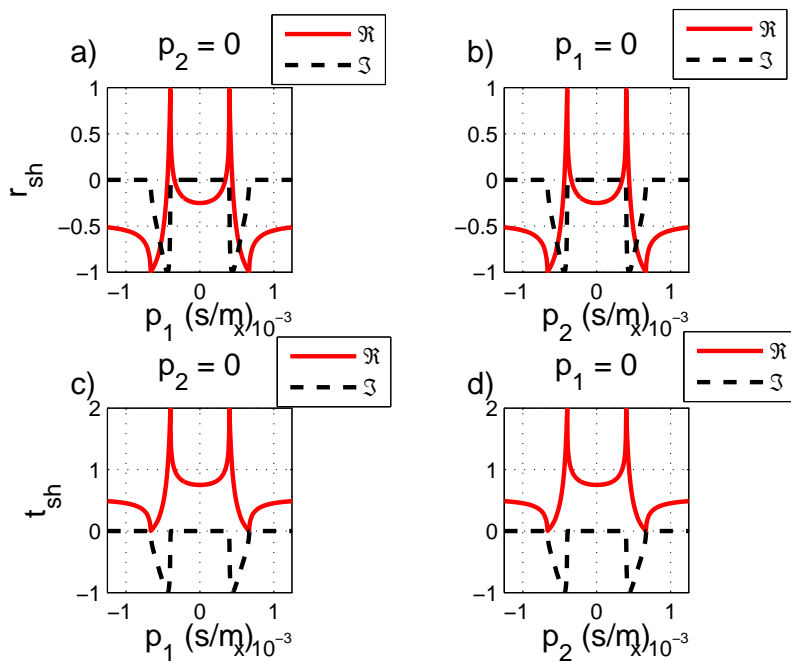


Figure 2.4: a) In line slice b) Cross line slice of the reflection coefficient. c) In line slice d) Cross line slice of the transmission coefficient for a horizontal reflector. 512 in line and cross line traces are used

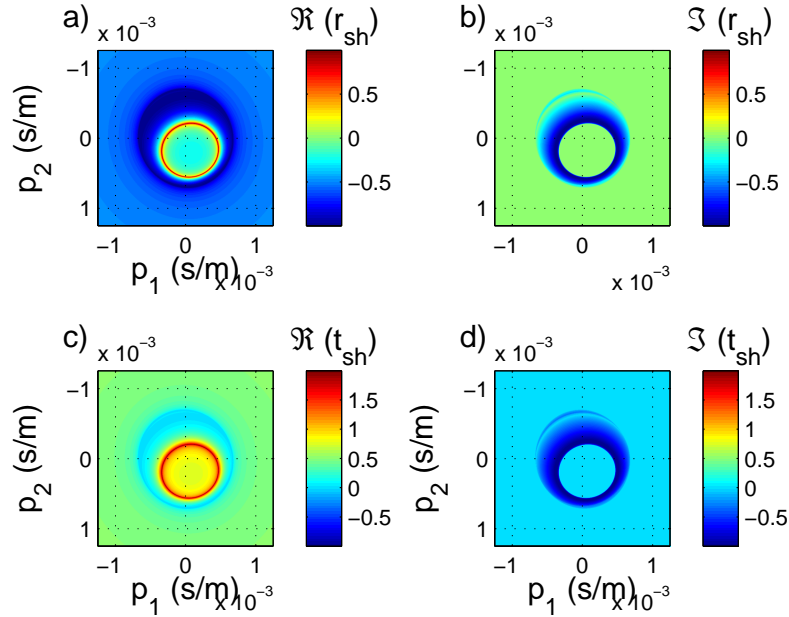


Figure 2.5: a) Real part b) Imaginary part of the reflection coefficient. c) Real part d) Imaginary part of the transmission coefficient for a dipping interface. 512 in line and cross line traces are used

R and T coefficients. This Figure differs from the Figure 2.3 in a way that the obtained results are not symmetric any more with respect to the zero slowness. In line and cross line slice of the R and T coefficients corresponding to the considered case are shown in Figure 2.6, which illustrates that the R and T coefficient curves have been shifted towards to the positive value of the slowness and have lost the symmetrical behavior about the zero slowness as expected.

In order to reveal the effect of the data acquisition geometry on the concluding results, two more cases have been considered. In the first case, 128 cross-line traces are considered. For performing the second case, 8 cross-line traces have been used. The number of in-line traces does not change for both given cases and it is 512. Using 512 in-line and 128 cross-line traces, the in-line and cross-line slices of the R and T coefficients are shown

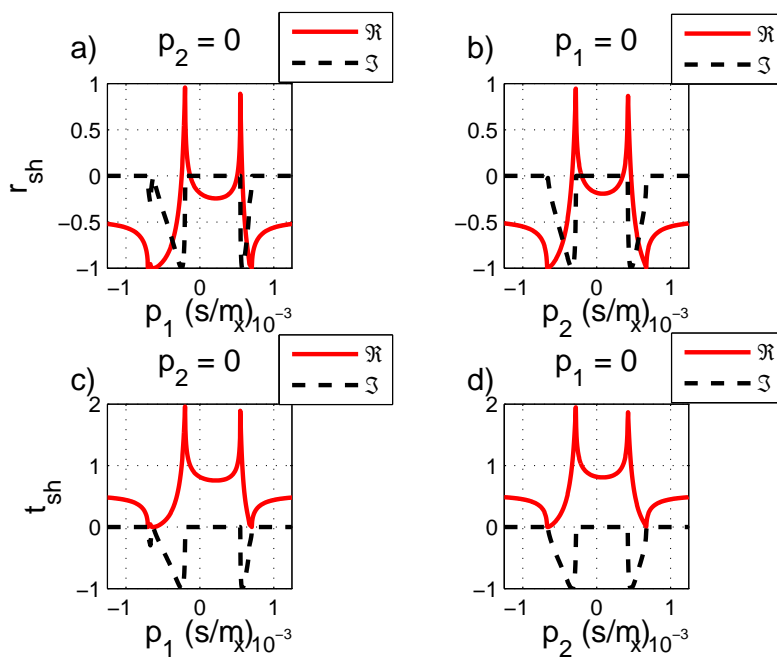


Figure 2.6: a) In line slice b) Cross line slice of the reflection coefficient. c) In line slice d) Cross line slice of the transmission coefficient for a dipping interface. 512 in line and cross line traces are used

in Figure 2.7. The obtained in-line slices follow the same pattern as in the previous case. Further, on considering the cross-line slices of the R and T , it is demonstrated that the R and T coefficients follow the expected value at zero slowness. The R and T coefficients curve deviate from the expected behavior at the critical slowness as the R and T coefficients are not attaining values of 1 and 2, respectively. This discrepancy resides on the fact that there is no sample point used by MATLAB corresponding to the critical slowness. As the sample rate is inversely proportional to the number of traces, it is the 0.000019 s/m for the considered case. Now, following the theory, 0.000343 s/m is expected as the critical slowness while 0.0004039 s/m is the nearest point to the critical slowness calculated by MATLAB. Additionally, in order to obtain the R and T coefficients corresponding to all points in between two sample points, interpolation is used by MATLAB. It is also demonstrated from Figure 2.4 and can be shown by theory that there is a huge difference in the obtained value of the R and T coefficients affiliated to the nearest slowness on either side of the critical slowness. However, MATLAB is not sensitive to this type of contrast and comes up with underestimated results as shown in Figure 2.7.

On continuation of the presented analysis, Figure 2.8 shows the in-line and cross-line slices of the R and T coefficients obtained using 8 cross-line traces. The inspection of the cross-line slices illustrates that the R and T coefficients follow the expected behavior at zero slowness. As slowness increases, the distorted picture of the R and T coefficients is obtained. Even though the density and the velocity of the reflector were consistent for all cases in the current study, we obtain the distorted pattern of the R and T coefficients if appropriate data acquisition geometry is not considered. Thus, data acquisition geometry plays an important role in order to image the target horizon. The 3D reflection and transmission as well as in-line and cross-line slices of the R and T coefficient for a dipping interface are given by (Sharma and Ferguson, 2009b)

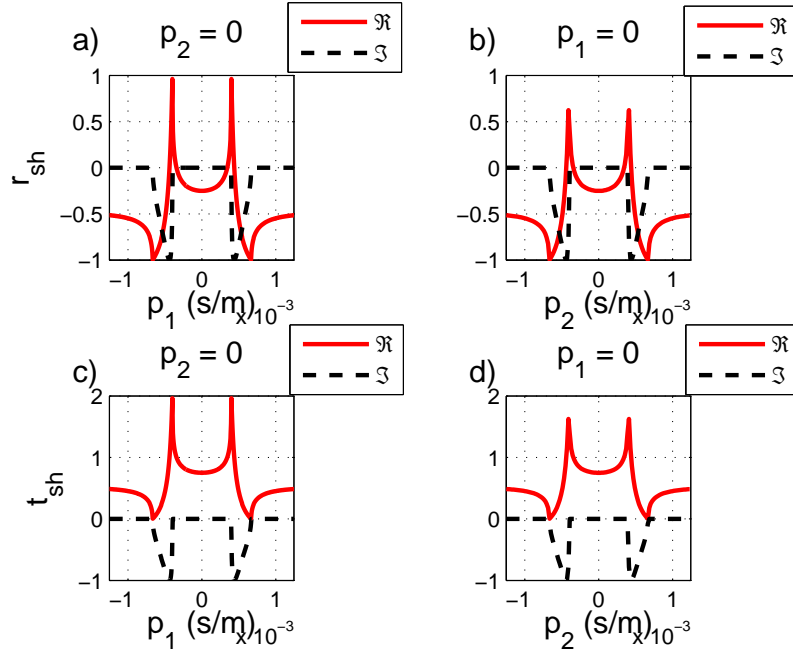


Figure 2.7: a) In line slice b) Cross line slice of reflection coefficient. c) In line slice d) Cross line slice of transmission coefficient for a horizontal interface. 512 in-line and 128 cross-line traces are used.

2.4 Conclusions

The angle of incidence is obtained by using the cross product of two known unit normals. This value of incident angle is used in the analytical expression of the R and T coefficients. By doing this, the R and T coefficients have been obtained in the plane wave domain. First of all, the R and T coefficients have been obtained for the reflector aligned with the computational grid. Presently, it has been shown that obtaining the R and T coefficients for the reflector non-aligned with the computational grid required an ordinary effort only. The importance of this approach is an automatic adaptation of the R and T coefficient

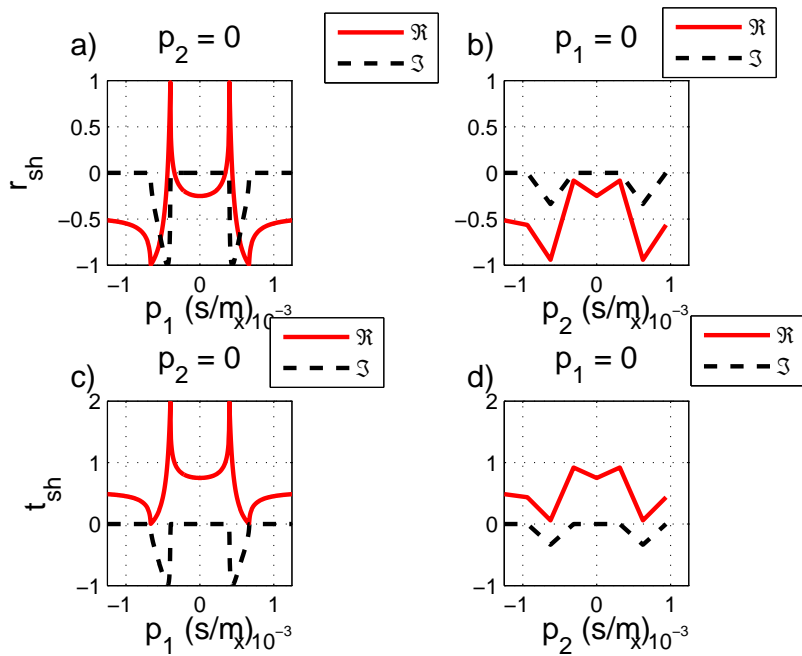


Figure 2.8: a) In line slice b) Cross line slice of the reflection coefficient. c) In line slice d) Cross line slice of the transmission coefficient for a horizontal interface. 512 in-line and 8 cross-line traces are used.

expressions to the special dipping interface case. The power of this is, that no ray tracing is required. The R and T coefficients obtained for the same number of in line traces but, different numbers of cross line traces, show the deviation from the expected one. It reveals the problem associated with data acquisition that make it necessary to acquire the data correctly.

Chapter 3

9C-3D modelling for VTI media.

3.1 Summary

For comparison with real seismic data, and with synthetic data derived from fully elastic numerical methods, I present a *9C-3D* numerical modeling approach that is posed in the slowness domain. The slowness domain approach has a number of advantages: 1) multipathing with no internal reflection “ simpler event registration”. 2) Parallelizable over temporal frequency. 3) Stable. 4) High frequency. 5) Selectable propagating mode. 6) No discontinuity of slopes. Following the Fourier decomposition, wavefield extrapolation proceeds as a set of distributed, monochromatic extrapolation steps in depth. *3D* phase shift operators in anisotropic media have been used to extrapolate a *3C* source wavefield to each grid point. There, source polarization is transformed into the orientation of the multicomponent geophone by applying a rotation matrix on the extrapolated field. The polarization angle(dip) of compression wave computed from the incident angle that is the angle between the slowness vector and the normal to each grid point and the horizontal projection of the associated slowness vector at each grid point are the essential parameters of the rotation matrix. Traveltimes in anisotropic media are accommodated through plane wave transformation and phase shift, and a propagation angle is produced. For each geophone component, the polarization angle is calculated from the propagation angle. Finally, extract the desired component for analysis. My numerical results demonstrate that all 9 source-receiver combinations are reliably estimate using my procedure.

3.2 Introduction

Seismic anisotropy plays an important role in oil and gas exploration field in order to improve the image of target horizons (Grechka, 2009). Consequently, it is less forgiving and more detrimental to our data acquisition and processing efforts to ignore the anisotropy. It has been demonstrated that wavefield propagation through anisotropic media deviates from the isotropic case (Aki and Richards, 1980) and is composed of two parts: kinematic and dynamic. Of interest here is the kinematic analysis of wave propagation in anisotropic media. The use of travel time information to infer anisotropy of the subsurface and to image seismic data motivates this choice. In order to attain this information it is worth to review wave-field propagation in the transverse isotropic media.

3.3 Wave propagation in transversely isotropic media

Dealing with anisotropy in the oil and gas industry contains two main objectives at the exploration and field development stages. In exploration, we would like to improve the velocity model by estimating anisotropy from available seismic data and migrate the data using this model in a hope to improve the image of target horizons compared to the image obtained by using the best isotropic velocity model (Grechka, 2009). As long as it happens our job is done and we do not care about the physical reason of anisotropy. Conversely, we do want to find out the physical reason for the measured anisotropy at the field development stage. In consequence, a sound understanding of the basic principles of seismic wave propagation in anisotropic media and the ability to model the main characteristics of propagating waves are required. The equation of motion for a transversely isotropic solid can be represented as

$$\rho \frac{\partial^2 u_i}{\partial t^2} = \frac{\partial \tau_{ij}}{\partial x_j}, \quad (3.1)$$

where the u_i are the components of particle displacement, the τ_{ij} are the stresses and ρ is the density of the corresponding medium and $i, j=1,2,3$.

To solve equation 3.1 in a unique fashion, the displacement vector \mathbf{u} and the stress tensor τ are related to each other as given by Hooke's law and can be expressed as

$$\tau_{ij} = c_{ijkl}\epsilon_{kl}, \quad (3.2)$$

where \mathbf{c} is the fourth-rank stiffness tensor and $\epsilon_{ij} = \frac{1}{2}(\partial u_i/\partial x_j + \partial u_j/\partial x_i)$, and $i, j=x, y, z$ or $1,2,3$. The substitution of equation 3.2 into equation 3.1 yields the wave equation as

$$\rho \frac{\partial^2 u_i}{\partial t^2} = c_{ijkl} \frac{\partial^2 u_k}{\partial x_l \partial x_j}. \quad (3.3)$$

Its standard solution is a harmonic plane wave of the form

$$u_k = AU_k e^{i\omega(n_j x_j - Vt)}, \quad (3.4)$$

where \mathbf{U} is the polarization vector, ω is the angular frequency, \mathbf{n} is the unit wavefront normal and V is the phase velocity. Substitution of the plane wave solution 3.4 into equation 3.3 leads to the Christoffel equation (Tsvankin, 2001)

$$\begin{bmatrix} (G_{11} - \rho V^2) & G_{12} & G_{13} \\ G_{21} & (G_{22} - \rho V^2) & G_{23} \\ G_{31} & G_{32} & (G_{33} - \rho V^2) \end{bmatrix} \begin{bmatrix} U_1 \\ U_2 \\ U_3 \end{bmatrix} = 0. \quad (3.5)$$

with $G_{ik} = c_{ijkl} n_j n_l$.

The Christoffel equation (3.5) is the most important equation for analysis of wave phenomena in anisotropic media. In fact this equation is treated as an eigenvalue-eigenvector problem for the symmetric, positive definite matrix \mathbf{G} . The positive definiteness of tensor \mathbf{c} ensures the positive definiteness of \mathbf{G} while its symmetry is the consequence of the symmetry of the stiffness tensor. Since the kinematic and dynamic signature of body waves for HTI media can be obtained from known analysis of VTI media, I consider a

transversely isotropic medium where the z axis coincides with the normal to the plane of transverse isotropy and can be treated as the axis of rotational-symmetry. However, it is known that such a medium can be characterized by five elastic constants (Slawinski, 2003) and using these constants in equation 3.5, the eigenvalues of the Christoffel equation can be obtained from

$$\det[G_{ij} - \rho V^2 \delta_{ik}] = 0. \quad (3.6)$$

which yields a cubic equation for ρV^2 . The Christoffel equation yields three possible values of the phase velocity which belongs to the P-wave and two shear waves for a given phase direction \mathbf{n} . Therefore, the S-wave is splitted into two modes with different velocities and polarizations. However, the three eigenvalues of $\mathbf{G}(\mathbf{n})$ are the squared phase velocities of the three body waves and can be expressed as

$$V_p^2(\theta) = \frac{1}{2\rho} [(c_{11} + c_{44}) \sin^2(\theta) + (c_{33} + c_{44}) \cos^2(\theta) + D], \quad (3.7)$$

$$V_{sv}^2(\theta) = \frac{1}{2\rho} [(c_{11} + c_{44}) \sin^2(\theta) + (c_{33} + c_{44}) \cos^2(\theta) - D], \quad (3.8)$$

$$V_{sh}^2(\theta) = \frac{1}{\rho} [c_{66} \sin^2(\theta) + c_{44} \cos^2(\theta)], \quad (3.9)$$

where

$$D = [((c_{11} - c_{44}) \sin^2(\theta) - (c_{33} - c_{44}) \cos^2(\theta))^2 + 4(c_{13} + c_{44})^2 \sin^2(\theta) \cos^2(\theta)]^{1/2}. \quad (3.10)$$

The complexity of these equation is a main problem to use of anisotropic model for seismic exploration but it can be reduced by using Thomsen's parameters (Thomsen, 1986a). These parameters play an important role for understanding seismic signatures in anisotropic media and can be expressed as

$$\alpha_0 = \sqrt{\frac{c_{33}}{\rho}}, \quad (3.11)$$

$$\beta_0 = \frac{\overline{c_{55}}}{\rho}, \quad (3.12)$$

where α_0 , β_0 are the P-wave and S-wave velocities along the rotational-symmetry axis and anisotropy can be characterized by the dimensionless coefficients

$$\epsilon = \frac{c_{11} - c_{33}}{2c_{33}}, \quad (3.13)$$

$$\gamma = \frac{c_{66} - c_{55}}{2c_{55}}, \quad (3.14)$$

and

$$\delta = \frac{(c_{13} + c_{55})^2 - (c_{33} - c_{55})^2}{2c_{33}(c_{33} - c_{55})}. \quad (3.15)$$

The instinctive application of the coefficients ϵ and γ is clear as they vanish in isotropic media. Thus, the magnitude of the P and SH-wave anisotropy can be measured from the values of ϵ and γ . The intuitive appeal of the coefficient δ is not as transparent as those of ϵ and γ and might seem unexpected. The significance of δ becomes apparent once it is noticed that

$$\frac{d^2 V_p}{d\theta^2} \Big|_{\theta=0} = 2\delta\alpha_0. \quad (3.16)$$

Consequently, δ is not just an arbitrary combination of the elastic coefficients. Instead, the curvature of the P-wave velocity function at the vertical is governed by δ . It also governs the P-wave normal moveout velocities from horizontal reflectors and plays a key role for seismic reflection data (Grechka, 2009). On being acquainted with Thomsen's parameters, the phase velocity expression of the body waves can be expressed as

$$V_p^2(\theta) = \alpha_0^2[1 + \epsilon \sin^2 \theta + D^*(\theta)], \quad (3.17)$$

$$V_{SV}^2(\theta) = \beta_0^2[1 + \frac{\alpha_0^2}{\beta_0^2} \epsilon \sin^2 \theta - \frac{\alpha_0^2}{\beta_0^2} D^*(\theta)], \quad (3.18)$$

$$V_{SH}^2(\theta) = \beta_0^2[1 + 2\gamma \sin^2 \theta], \quad (3.19)$$

where

$$D^*(\theta) = \frac{1}{2} \left(1 - \frac{\beta_0^2}{\alpha_0^2}\right) \left\{ \left[1 + \frac{4\delta}{\left(1 - \frac{\beta_0^2}{\alpha_0^2}\right)^2} \sin^2 \theta \cos^2 \theta + \frac{4\left(1 - \frac{\beta_0^2}{\alpha_0^2} + \epsilon\right)\epsilon}{\left(1 - \frac{\beta_0^2}{\alpha_0^2}\right)^2} \sin^4 \theta\right]^{1/2} - 1 \right\}. \quad (3.20)$$

Once the eigenvalues of the Christoffel equation are known from equations 3.17, 3.18 and 3.19, the corresponding eigenvectors \mathbf{U} can be computed from any two equations of the three equations of the Christoffel equation 3.5. Since the Christoffel equation is real and symmetric, the obtained polarization vectors of the body waves are mutually orthogonal for any given phase direction \mathbf{n} (Tsvankin, 2001). However, the polarization are generally neither parallel nor orthogonal to the wavefront normal (Tsvankin, 2001).

Further, it is known that multicomponent seismic analysis is an effective technology for risk reduction in exploration and development. In exploration stage improved imaging, direct hydrocarbon and lithology indication can be offered by multicomponent measurement while development setting facilitate improved reservoir illumination and characterization by multicomponent measurements (Grechka, 2009).

The importance of the anisotropy and multicomponent seismic over the isotropy and single component seismic motivates the author to model *9C-3D* for the vertical transverse isotropic (VTI) media. Here, VTI media is taken into account because of its simplicity in the case of the anisotropic media beyond the isotropic media.

3.4 Theory

To investigate seismic wave interaction with anisotropic media, I extrapolate the wavefield first and then apply a rotation matrix on this wavefield in order to obtain multicomponent data. Now, two parts: phase extrapolation of a known source wavefield, and how

to build the rotation matrix are discussed in the following section.

Wave field extrapolation in the plane wave domain insures efficiency in terms of computational time (Sharma and Ferguson, 2009b). Given a source type, the source wavefield is extrapolated from the earth surface to the reflector as

$$\varphi_{\Delta z} = \varphi_0 e^{i \Delta z q \omega} \quad (3.21)$$

where φ_0 is the spectra of the source wavefield at the surface obtained via the Fast Fourier Transform (FFT)

$$(t \rightarrow \omega, x \rightarrow p_1 \omega, y \rightarrow p_2 \omega)$$

of the source wavefield. Vertical slowness, q is dependent on horizontal slownesses p_1 and p_2 and seismic velocity through the scalar wave-equation. In anisotropic media, q depends on a set of elastic coefficients - α_0 , β_0 , δ , ϵ , and γ for transversely isotropic (TI) media. The source wavefield $\varphi_{\Delta z}$ is the wavefield at depth Δz after extrapolation, and q is the vertical slowness and is known for the different seismic wave modes in anisotropic media (Ferguson and Margrave, 2008) and shown in Appendix B.

After extrapolation, the source wavefield resides on the reflecting plane. Together, the polarization directions of P-, SV-, and SH-waves (compression, vertical shear, and horizontal shear respectively) characterize a 3 dimensional co-ordinate system defined here as the survey co-ordinate system, while the recording coordinate system is characterized by the three component directions of a 3C geophone.

To model the arrival of a 3C wave, I rotate the co-ordinate system from the survey co-ordinate to the recording co-ordinate system to register the source energy on the vertical, in-line, and cross-line components. With the basic method of a co-ordinate system transformation (Neufeld and Clayton, 2000), I transform the survey coordinate system into the recording system by a rotation of θ_1 degrees about the x axis followed by a rotation of ϕ degrees about the z axis.

The polarization angle (θ_1) is the angle that the polarization vector of the incident compressional wave makes with the vertical component of the 3C geophone. From the basic knowledge of wave propagation through anisotropic media it has been demonstrated that the polarization direction of compression waves deviate from the propagation direction but can be computed for a given propagation angle (Slawinski, 2003). Now to compute the polarization angle (θ_1), the propagation angle(θ) is computed first. Angle θ is the angle that the slowness vector of an incident plane wave makes with the vertical component of a 3C geophone and can be computed as described below. These angles (θ, ϕ) are defined pictorially in Figure 3.1.

A hypothetical geophone indicated by three orthogonal blue lines are aligned with spa-

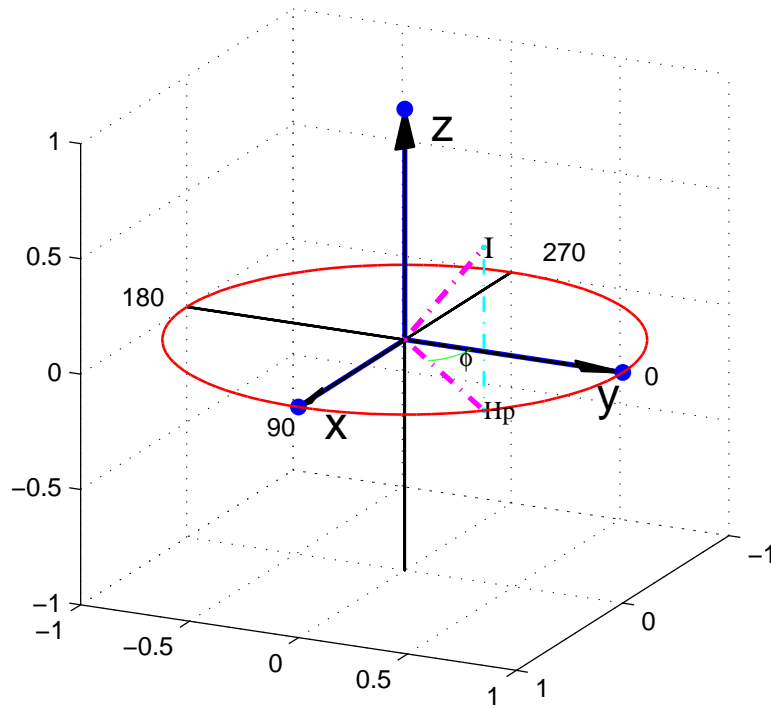


Figure 3.1: A hypothetical 3C geophone at a grid point . “I” represents the normal to an incident plane wave and azimuth is measured relative to y axis. Azimuth 0 indicates the in-line direction and the cross-line direction is characterized by 90° .

cial axes x , y , and z . The normal to an incident plane wave is indicated by the symbol “ I ”, and the horizontal projection of “ I ” is indicated by H_p . Azimuth ϕ is the angle which the horizontal component y makes with H_p and is indicated on this Figure. The propagation angle θ is the angle between the vertical component z and “ I ”.

The slowness vector $\hat{\mathbf{p}}$ characterizes the direction of the incident wavefield and can be computed using equation 2.1. The unit normal associated with a $3C$ geophone at a grid location is

$$\hat{\mathbf{a}} = \sin \theta_a \cos \phi_a \hat{\mathbf{i}} + \sin \theta_a \sin \phi_a \hat{\mathbf{j}} + \cos \theta_a \hat{\mathbf{k}}, \quad (3.22)$$

where θ_a and ϕ_a are the dip and azimuth of the normal to the interface respectively.

The angle θ between $\hat{\mathbf{p}}$ and $\hat{\mathbf{a}}$ is then computed by a cross product according to (Ferguson and Margrave, 2008)

$$\sin \theta = |\hat{\mathbf{p}} \times \hat{\mathbf{a}}|, \quad (3.23)$$

where \times indicates a cross product. Note, though I restrict my discussion here to horizontal interfaces $\hat{\mathbf{a}} = \hat{\mathbf{k}}$ for simplicity, I anticipate implementation of dipping interfaces as an extension to this approach.

The propagation angle θ , once computed, is used to calculate the polarization angle in terms of elastic coefficients (Slawinski, 2003). I develop a relationship between these two angles in terms of Thomsen parameters (Thomsen, 2002) according to

$$\theta_1 = \tan^{-1} \frac{(\alpha^2(\theta) - \beta_0^2 \sin^2 \theta - \alpha_0^2 \cos^2 \theta)}{\sqrt{(\alpha_0^2 - \beta_0^2) [\alpha_0^2 [2\delta + 1] - \beta_0^2]} \sin \theta \cos \theta}. \quad (3.24)$$

where θ_1 is the polarization angle of P-wave if $\alpha(\theta)$ is considered as the P-wave velocity and by conceiving $\alpha(\theta)$ as the shear wave velocity it is polarization angle of SV-wave, θ is the propagation angle computed from equation 3.23. The P-wave polarization angle can be computed from the known polarization angle of the SV-wave (θ_{SV}) by subtracting 90 to (θ_{SV}) (Tsvankin, 2001). Now, given θ_1 and a known source, effective $3C$ recording

D_{θ_1} is computed

$$D_{\theta_1} = \begin{bmatrix} 1 & 0 & 0 \\ 0 & \cos \theta_1 & \sin \theta_1 \\ 0 & -\sin \theta_1 & \cos \theta_1 \end{bmatrix} W, \quad (3.25)$$

where W describes the known source type. Generally, a $3C$ source wavefield is written in matrix form as (Ferguson, 2009)

$$W = \begin{bmatrix} S_1 \\ S_2 \\ P \end{bmatrix}, \quad (3.26)$$

where S_1 , S_2 and P are the cross-line, in-line and vertical components of the source respectively. A vertical source wavefield, for example, is written

$$W = \begin{bmatrix} 0 \\ 0 \\ P \end{bmatrix}. \quad (3.27)$$

Figure 3.2 depicts four $3C$ geophones positioned at grid points 200 m below a source position. In this Figure, 1, 2, 3 and 4 describe the four quadrants of a circle whose periphery traces the azimuth from 0 to 360° and has the in-line and the cross-line directions as horizontal and vertical axes. Rotation θ_1 degrees about the x axis (H_1) is anti-clockwise for geophones to the left of the source and clockwise for geophones to the right. So, I adopt the convention of a positive angle for anti-clockwise rotation and negative for clockwise rotation (Neufeld and Clayton, 2000).

Azimuth ϕ is the angle between one of the horizontal geophone components and the plane made with the source, and it is calculated from the input parameters of a plane wave. Following a rotation of θ_1 degrees about the x axis, the source waveform is rotated ϕ degrees about the vertical axis. A rotation ϕ about the vertical axis is computed and

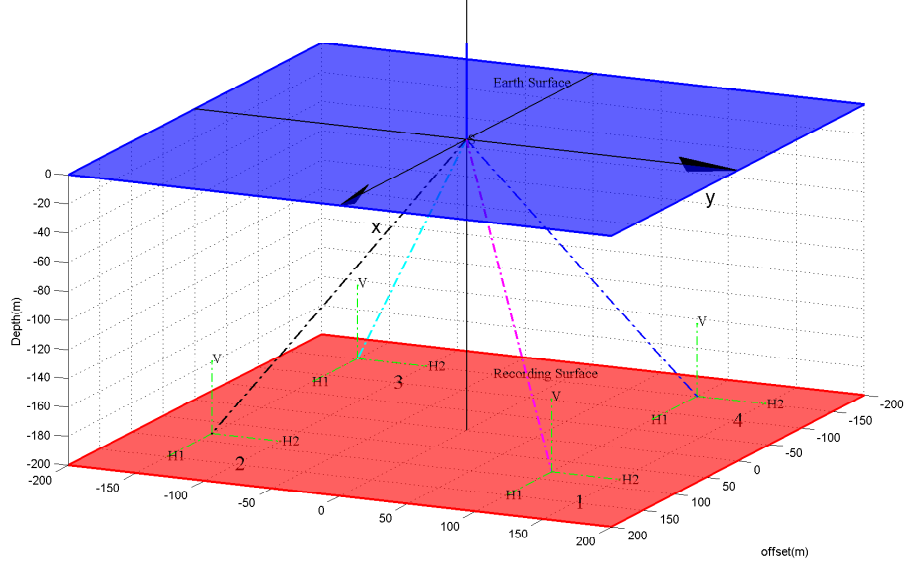


Figure 3.2: Schematic representation of considered model and positioning of 3C geophones at reflecting surface. 1, 2, 3 and 4 describe the four quadrant of a circle whose periphery trace the azimuth from 0 to 360° and has y and x axis as horizontal and vertical axis, respectively.

is written as

$$D_\phi = \begin{bmatrix} \cos \phi & \sin \phi & 0 \\ -\sin \phi & \cos \phi & 0 \\ 0 & 0 & 1 \end{bmatrix} W, \quad (3.28)$$

As a single operation, rotation through θ_1 and ϕ is computed as

$$D = \begin{bmatrix} \cos \phi & \sin \phi \cos \theta_1 & \sin \theta_1 \sin \phi \\ -\sin \phi & \cos \phi \cos \theta_1 & \cos \phi \sin \theta_1 \\ 0 & -\sin \theta_1 & \cos \theta_1 \end{bmatrix} W, \quad (3.29)$$

where D is the source wavefield rotated into the orientation of the 3C geophone. Normally it is written as (Ferguson, 2009)

$$D = \begin{bmatrix} H_1 \\ H_2 \\ V \end{bmatrix}. \quad (3.30)$$

where H_1 , H_2 , and V are the cross-line, in-line and vertical components of the vector wavefield respectively.

3.5 Examples

Since up to 75% of oil and gas producing sedimentary basins worldwide are comprised of shales and it is a major contributor to observed seismic anisotropy (Grechka, 2009), a numerical model of a 700 m thick vertical transverse isotropic (VTI) medium (shale) is taken into account here. The anisotropic parameters of this shale in Thomsen (Thomsen, 1986a) parameters are $\alpha_0=3048$ m/s, $\beta_0 =1490$ m/s, $\epsilon=0.255$, $\delta=-0.27$, and $\gamma=0.480$. Now a known impulsive source is extrapolated through the medium using equation 3.21 in the plane wave domain and transformed back into the space and time domain at the interface. Further, the components of the recorded wavefield on 3C geophones have been sliced through the inline direction and at any given time. The red dashed line highlighted in the circle at the top right corner of Figure 3.3 c indicates the direction along which a vertical slice through the modelled data is taken. The in-line and cross-line directions are indicated by magenta and blue, respectively.

Figure 3.3a shows a cross-line slice of the recorded P-wave energy on the H_1 component obtained through the procedure outlined above and can be represented as registered energy versus offset (REVO). REVO analysis reveals that energy registration increases with offset and polarity reversal occurs on either side of zero offset on behalf of different orientations of H_1 components with respect to the source on either side. The circle in the top right corner of Figure 3.3c is the plan view of a recording surface where the source location is at the center of the origin. REVO analysis of the recorded P-wave energy on the H_2 component is shown in Figure 3.3b. It indicates that energy registration decreases with offset and the polarity follows the stationary behavior on either side of zero offset

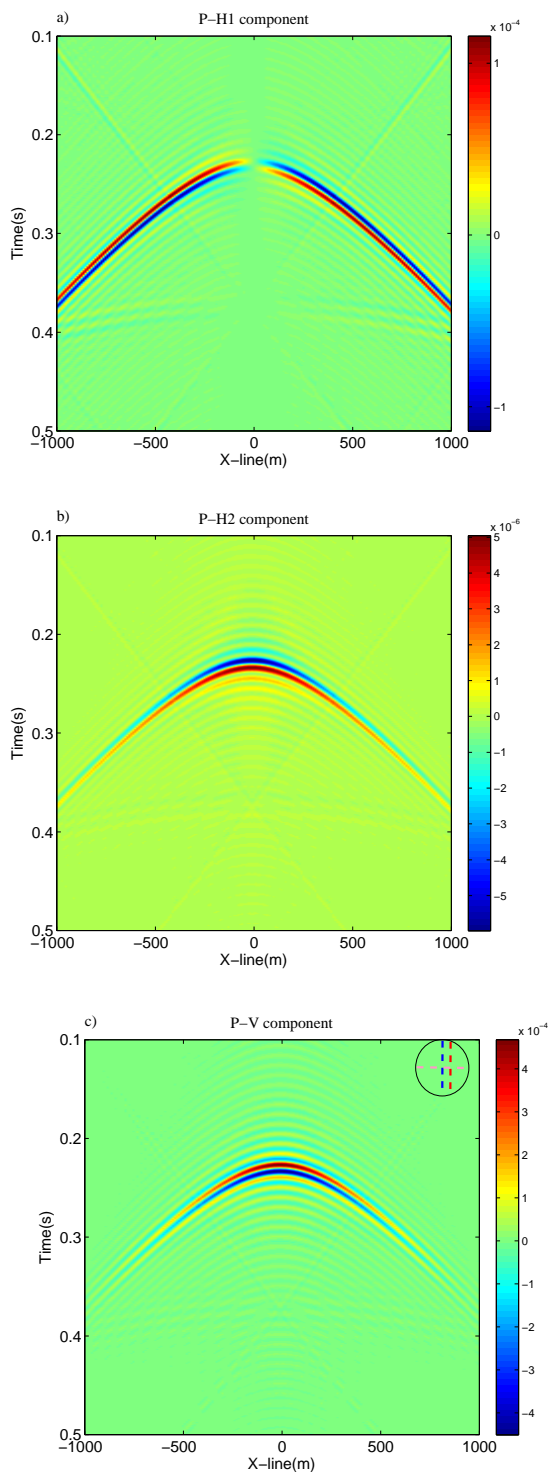


Figure 3.3: (a) Registered energy versus offset (REVO) analysis of P-wave on H_1 component illustrate that H_1 component is more favorable for energy registration as offset increases. Polarity reversal appear on the either side of zero offset. (b) (REVO) analysis of P-wave on H_2 component illustrate that H_2 component is more favorable for energy registration near to zero offset. Polarity remains stationary on the either side of zero offset. (c) Recorded P-wave energy on vertical component demonstrate that energy registration on vertical component decreases with offset. Polarity follow the stationary behavior on either side of zero offset.

due to the same orientation of the H_2 components with respect to the source on either side. Figure 3.3c shows the REVO of P-wave energy on the vertical component and energy registration decreases with offset. Since the propagation angle increases with offset, it enforces the polarization angle to be increase towards the H_1 component along the direction in which the slice of recorded data is taken. Thus, it makes the H_1 component more favorable for energy registration at large offsets and endorses the obtained REVO analysis.

Figure 3.4a, b and c indicate the time slices of the recorded P-wave energy on H_1 , H_2 and V component, respectively, and reveal the variation of recorded energy versus azimuth (REVA). The obtained circle in the $x-y$ plane manifests azimuthal isotropy of the medium as expected. It shows the efficacy of the proposed extrapolation method. Figure 3.4a demonstrates that no energy is registered on the H_1 component in the in-line direction as expected. Energy registration increases as azimuth increases from 0 to 90 degree. Polarity reversal occurs on either side of a line that bisects the obtained circle along the in-line direction. Since the H_1 components of 3C geophones of quadrant 1, 2 or 3, 4 (shown in Figure 3.2) contain the same orientation with respect to the source, they respond to the incident wave field in the same manner. While, the H_1 components of quadrant 1, 4 or 2, 3 possess antipode orientation with respect to the source and respond in an opposite way to the incident wavefield. This makes it possible to endorse the obtained polarity reversal behavior. REVA analysis of the recorded P wave energy on the H_2 component (shown in Figure 3.4b) indicates that the recorded energy decreases as azimuth increases from the in-line direction to the cross-line direction. No energy is registered on the H_2 component in the cross-line direction in this case as the H_1 component is more favorable. Polarity on the H_2 component flips from on either side of a line that bisects the obtained circle along the cross-line direction. The H_2 components of 3C

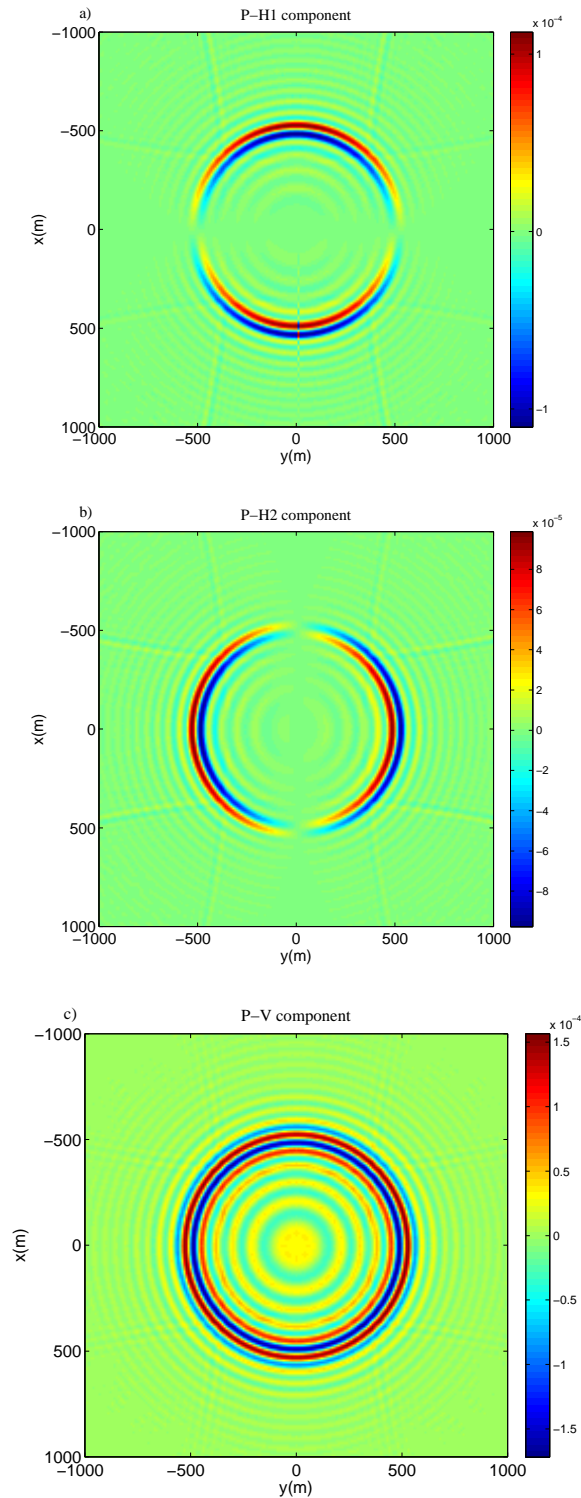


Figure 3.4: (a) Registered energy versus azimuth(REVA) analysis of P-wave at H_1 component indicates that energy registration increases as azimuth increases from 0 to 90. Polarity reversal occur on the either side of a line that bisects the circle along in-line direction. (b) REVA analysis of P-wave at H_2 component indicates that energy registration decreases as azimuth increases from 0 to 90. Polarity reversal occur on the either side of a line that bisects the circle along cross-line direction. (c) REVA analysis of P-wave on vertical component reveal the variation of recorded energy and polarity with azimuth.

geophones of the quadrant 1, 4 or 2, 3 respond to the incident wavefield in the similar way in behalf of the same orientation of the components with respect to the source. At the same time, the H_2 components of 3C geophones of the quadrant 1, 2 or 3, 4 have the opposite orientation with respect to the source and respond to the incident wavefield in a reversal manner. Figure 3.4c shows the variation of the recorded P wave energy with azimuth on the vertical component. It demonstrates that the recorded P-wave energy on the vertical component follow the stationary amplitude behavior and polarity. Since, at a given time the orientation of the vertical component with respect to the incident wavefield remains constant with azimuth, thus, it reinforces the obtained REVA behavior.

REVO analysis of the recorded SV-wave energy on H_1 , H_2 and the vertical components are shown in Figure 3.5a, b and c, respectively. This slice demonstrates an interesting property possessed by SV-waves generated by an SV-source. For anisotropic media, SV-waves triplicate (exhibit three arrivals) when the thickness of the anisotropic medium is significant (Ferguson and Sen, 2004), and this is strongly apparent on V and H_1 in Figure 3.5. It is demonstrated by Figure 3.5a that energy registration on the H_1 component decreases with offset and polarity reversal is also occurred on either side of zero offset. Figure 3.5c shows that the vertical component is more favorable for energy registration at large offsets. As the offset increases, the P-wave polarization angle increases with vertical. Thus, the orientation of the polarization angle of the SV-wave, normal to the P-wave polarization angle, increases in the direction of the vertical component and assign it as the favorable component for energy registration at large offsets.

To verify the triplication phenomenon, another approach described by Ferguson (Ferguson and Sen, 2004) is delineated now. According to this approach wave field extrapolation can be done using an estimate \tilde{q} of the true vertical slowness q and an estimate of the

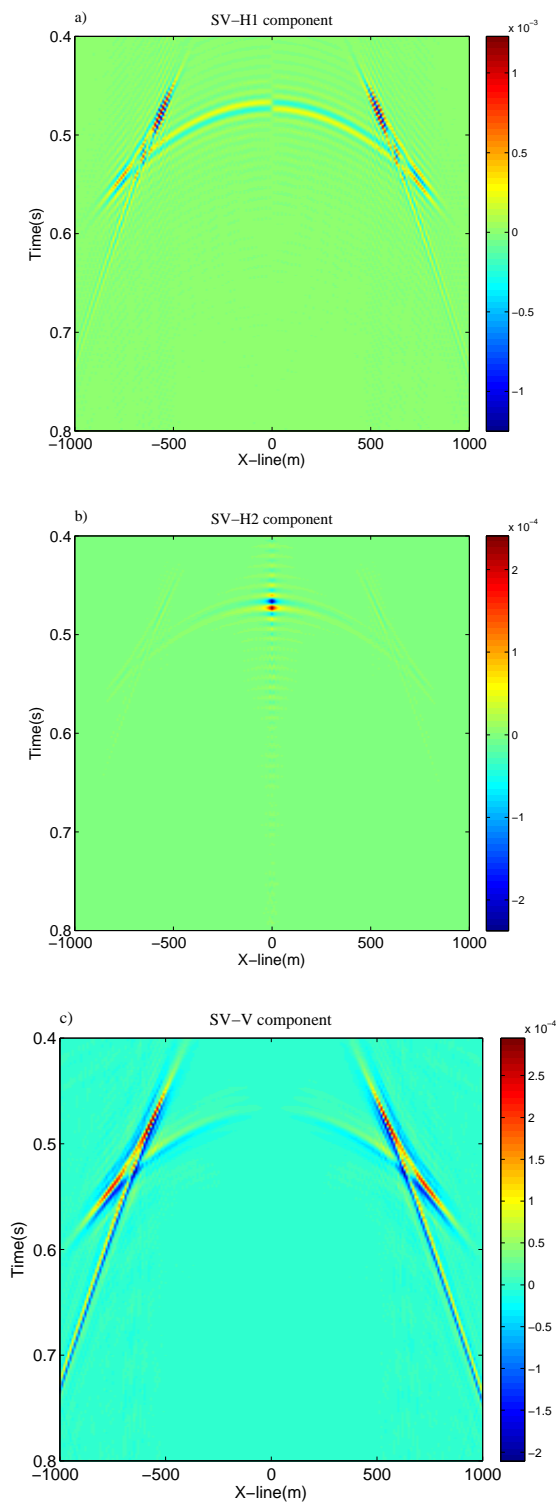


Figure 3.5: (a) REVO of SV-wave on H_1 component. The Triplication phenomena occurs in this case. Registered energy decreases with offset. (b) REVO analysis of SV-wave on H_2 component demonstrate that a minuscule amount of energy is registered on H_2 component. (c) REVO analysis of SV-wave on V component indicates that a registered energy increases with offset. Polarity reversal does not occur on the either side of zero offset.

true depth as

$$\varphi_{\Delta z} = \varphi_0 e^{-i\Delta\tilde{z}\tilde{q}\omega} \quad (3.31)$$

These estimated parameters are related to the travel time error parameter, $\Delta\tau$, via

$$\Delta\tau_{sv}(p) = 2[zq(p) - \tilde{z}\tilde{q}] \quad (3.32)$$

From the above equation, it follows that

$$-\tilde{z}\tilde{q} = \frac{\Delta\tau_{sv}(p) - 2zq(p)}{2} \quad (3.33)$$

where $\Delta\tau_{sv}$ can be defined in terms of the known vertical slowness and its derivatives with respect to Thomsen's parameters. Figure 3.6a shows the in-line slice of the extrapolated wavefield obtained by following the supporting approach and it is the facsimile of Figure 3.6b. Thus, the authentication of the triplication phenomena is demonstrated. Figure

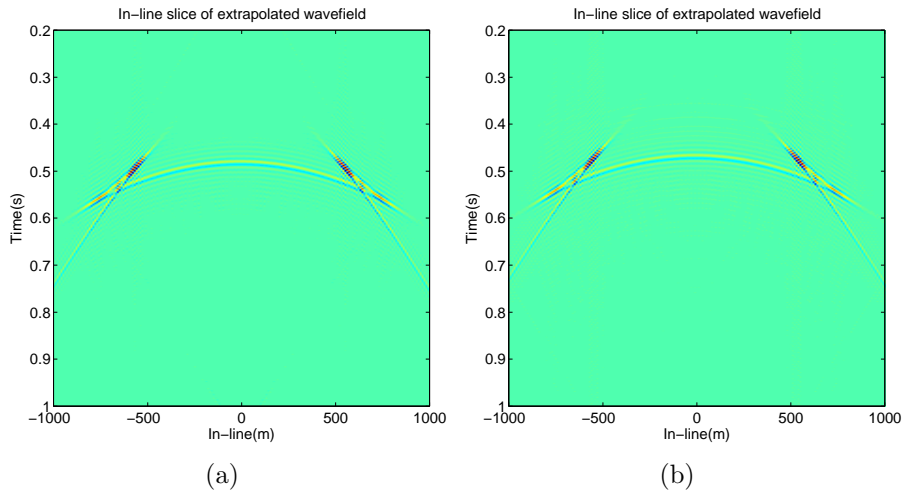


Figure 3.6: (a) In-line slice of the extrapolated SV wavefield by following the supportive approach and it is replica of that obtained by author and shown in (b) part. It shows the authentication of the triplication phenomena.

3.7 a, b and c reveal the variations of the registered SV-wave energy with azimuth on

the H_1 , H_2 and vertical components, respectively. More than one concentric circle is the counterpart of triplication here. Figure 3.7a indicates that no energy is registered in the in-line direction as expected and the registration increases as azimuth increases. Further, polarity reversal occurs on the either side of a line that bisects the obtained circle along the in-line direction due to the different orientation of $3C$ geophones of the concerned quadrant with respect to the source. Energy registration on the H_2 component decreases with azimuth and no energy is recorded on the H_2 component in the cross-line direction as shown in Figure 3.7b. Again the polarity reversal occurs on either side of a line that bisects the obtained circle in the cross-line direction. Figure 3.7c demonstrates the recorded SV-wave energy on the vertical component at a given time and it follows the stationary behavior with azimuth. At a given time the orientation of the SV-wave polarization angle with respect to the vertical remains constant for each azimuth and ensures the stationary behavior of the recorded energy on the vertical component.

REVO analysis of the recorded SH-wave energy on the H_1 component indicates that a small amount of energy is registered on the H_1 component and is shown in Figure 3.8a. Figure 3.8b shows that SH-wave energy registration on the H_2 component decreases with offset and polarity reversal occurs on either side of zero offset. No energy is registered on the vertical component since SH-wave is decoupled from other seismic waves.

Time slices of the recorded SH wave energy on the H_1 , H_2 and vertical components are shown in Figure 3.9a, b and c, respectively. Figure 3.8a reveals the variation of the recorded SH-wave energy on the H_1 component with azimuth and demonstrates that energy registration decreases with azimuth and no energy is registered in the cross-line direction. Energy registration on the H_2 component increases with azimuth and no energy is registered in the in-line direction.

The zero offset travel time shown in Figures 3.5a, b, c and 3.8a, b, c indicates that SH- and SV- waves travel with the same velocity along the symmetry axis. It is also noticed

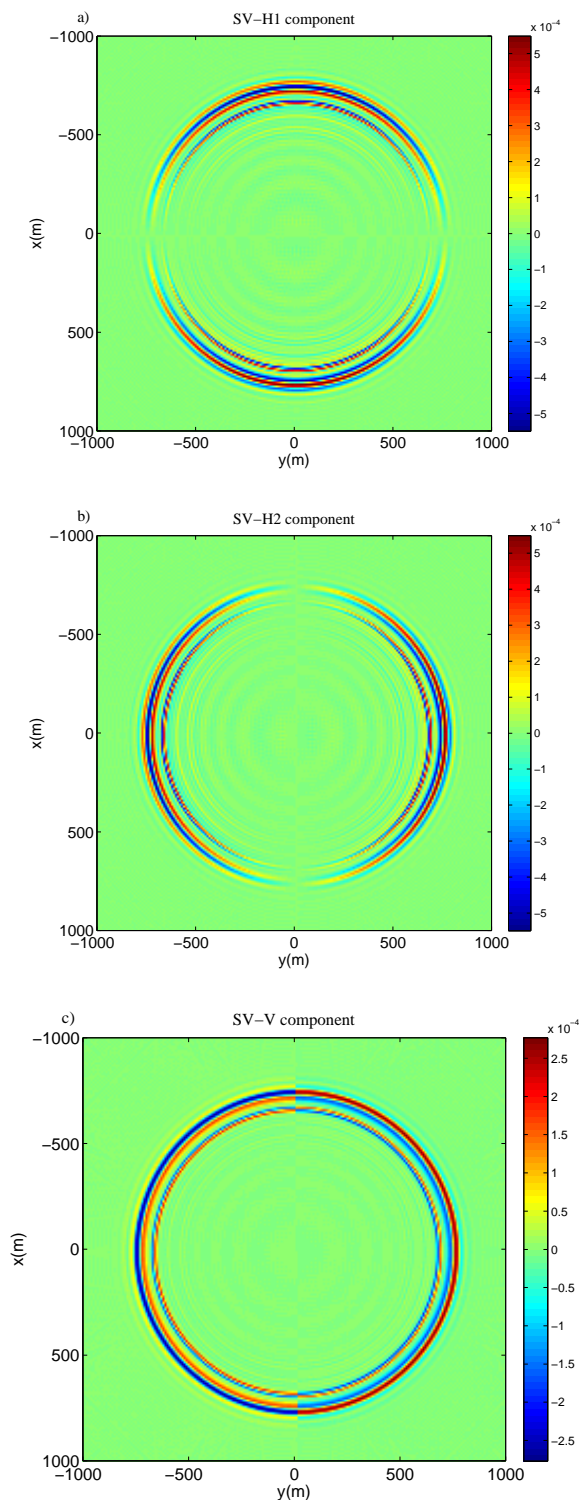


Figure 3.7: (a) REVA of SV-wave on H_1 component and more than one concentric circle is the counter part of the triplication. Polarity reversal occur on the either side of a line that bisects the circle along in-line direction. (b) REVA analysis of SV energy on H_2 component demonstrate that H_2 component is more favorable for energy registration in the in-line direction. (c) REVA analysis of SV-wave on V component indicates that energy registration on V component follows the stationary behavior. Polarity reversal occur on the either side of a line that bisects the circle along cross-line direction.

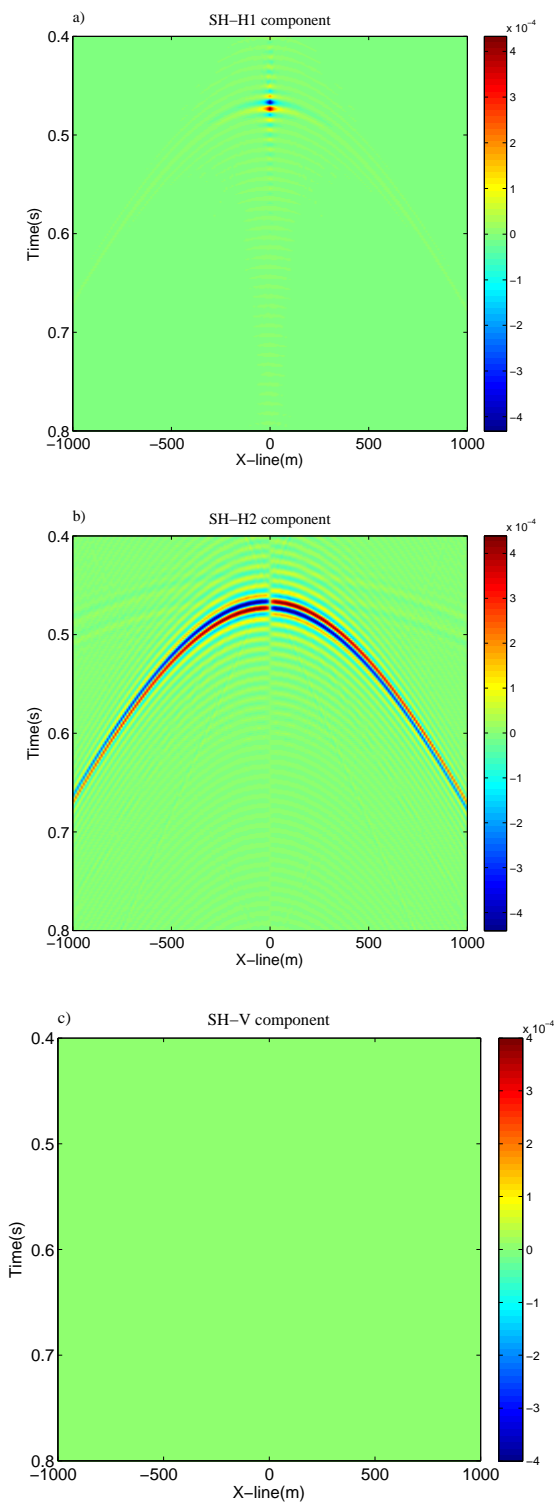


Figure 3.8: (a) REVO analysis of SH-wave energy on H_1 component indicates that a small amount of energy is registered on H_1 component. (b) REVO of SH-wave energy on H_2 component. Energy registration decreases with offset and polarity reversal occur on either side of zero offset. (c) Recorded energy of SH-wave on Vertical component and it is null in this case.

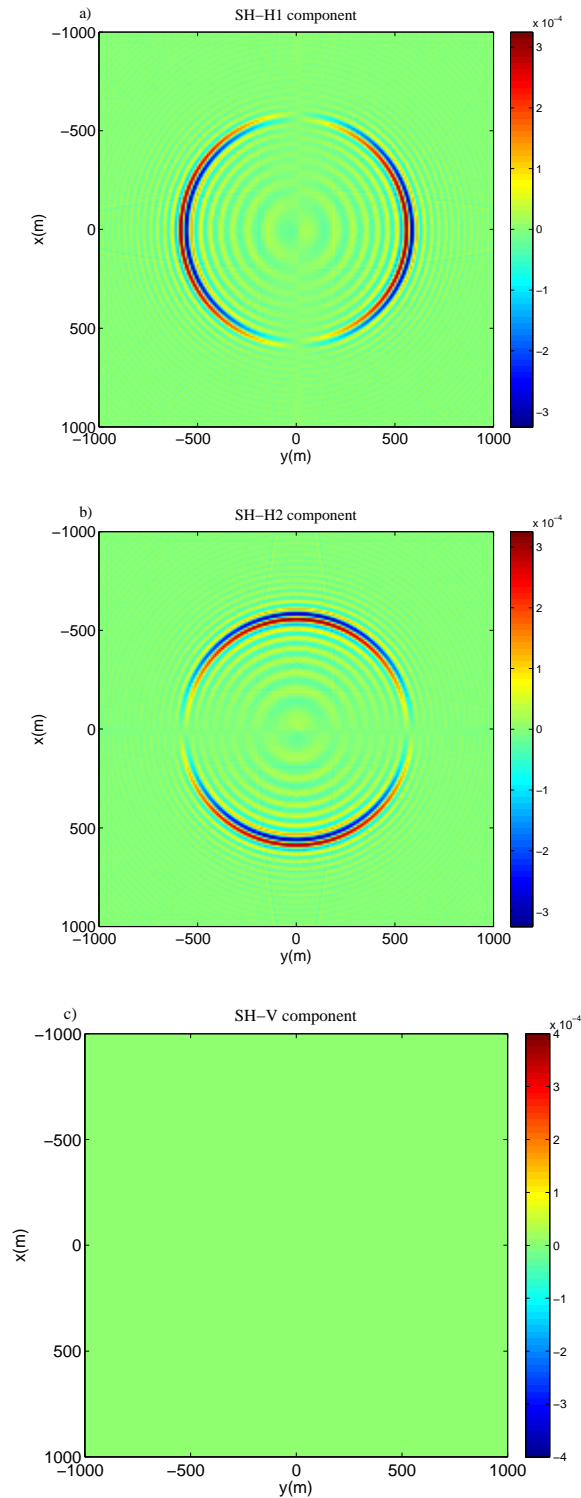


Figure 3.9: (a) REVA analysis of SH-wave energy on H_1 component indicates that energy registration decreases as azimuth increases from 0 to 90. Polarity reversal occur on either side of a line that bisect the circle along cross-line direction. (b) REVA of SH-wave energy on H_2 component. Energy registration increases with azimuth and polarity reversal occur on either side of a line that bisect the circle along in-line direction . (c) Recorded energy of SH-wave on Vertical component and it is null in this case.

here that at large offsets the arrival time of the SV- and SH- waves differs from each other. This phenomena is illustrated in more detail through the Figure 3.10. This Figure

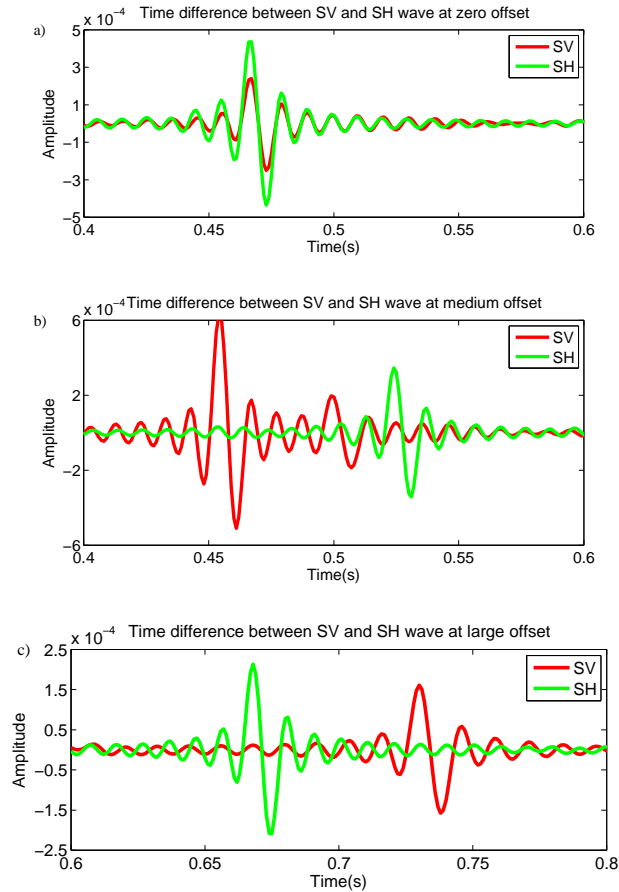


Figure 3.10: The arrival time of the SV- and SH- waves at a geophone located at (a) zero offset (b) medium offset (c) far offset. At medium offset SV energy is arriving at two times (expected, unexpected). The unexpected arrival time of SV energy is supported by the cusps in anisotropic media. The arrival time of the SH-wave is less than that of SV-wave at far offset.

shows the difference between the arrival time of the SV- and SH-waves at a geophone located at three different offset locations, such as zero, medium and large offsets. If I ignore the dynamic behavior of SH- and SV-waves, the favorable component of the energy registration and am only concerned about travel time information, the observations from this Figure are followed as:

- At zero offset both waves arrive at the same time.
- At medium offsets SV-wave energy is recognized by the geophone more than one time as supported by the cusp phenomena in anisotropic media.
- However, at far offsets, the SH wave arrives prior to the SV-wave

. These observations can be endorsed in the reference of the Figure 3.11. This Figure

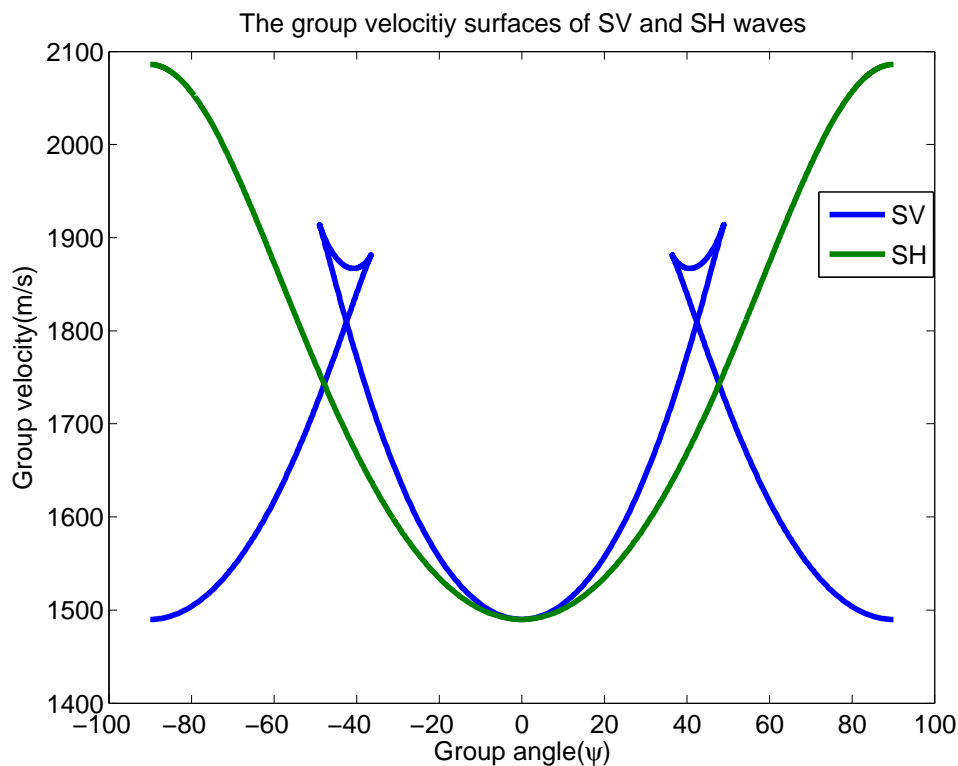


Figure 3.11: The velocity variation of the SV- and SH-waves with the group angle. The velocity curve of the SV-wave shows the cusp phenomena and possesses multiple value at angle near by 45 degree in this case.

reveals the group velocity behavior with angle. It is observed that the SH-wave velocity increases monotonically with angle(offset). Although, the SV-wave velocity increases until the maximum value is attained and then decreases and grasp the minimum value at far offsets. As it is seen that up to medium offsets, the SH-wave velocity surface lies below the SV-wave velocity surface, the arrival time of the SV-wave would be less

than that of the SH-wave arrival time up to medium offsets. At far offsets, the SH-wave velocity surface attains its maximum value that is greater than the SV-wave velocity at the same offset and this behavior shows the agreement for the occurred pattern of travel time of the SV- and SH-waves at far offset. It is also demonstrated that near an angle of 45 degree, the SV-wave velocity surface is multi valued with cusp and reinforced to the occurred pattern of the unexpected arrival time of the SV-wave at medium offset.

3.6 Conclusions

$9C - 3D$ seismic modeling for VTI has been accomplished in the plane wave domain. The authentication of the proposed extrapolation method has been demonstrated, kinematically. The REVO and REVA analysis of the known source (P, SV, and SH) on the components of the $3C$ geophone have been delineated here in order to illustrate favorable condition of energy registration on different components of the $3C$ geophone. Polarity reversal analysis with azimuth and offset has also been exposed. The phenomena of the triplication occurs in using an in-line source. This is supported by the another approach too.

Chapter 4

R and T coefficients in the plane wave domain for VTI media.

4.1 Summary

Presently, I obtain the reflection(R) and transmission (T) coefficients at the boundary between two transversely anisotropic media with a vertical axis of symmetry (VTI) in behalf of their importance for numerical computations. Additionally, these coefficients are valuable for full elastic wave modelling in anisotropic media. Classical R and T coefficients have been expressed as a function of the phase angle that can be computed by using the effective ray parameter. To do this, I compute a normal for each individual plane wave based on the local velocity that is a function of Thomsen's parameters of the medium and the vector cross-product of this normal with the normal to the reflector yields a ray parameter that is used here to compute the corresponding R and T coefficients for a given plane wave. Now following Graebner's approach (Graebner, 1992), I obtain R and T coefficients in terms of Thomsen's parameters as these parameters are essential for understanding the seismic wave's signatures in the anisotropic media. Moreover, amplitude versus offset (AVO) is a variation in seismic reflection amplitude with offset and it is also referred as AVA (amplitude versus angle). Typically, the amplitude decreases with offset because of geometric spreading, attenuation and other factors while an AVO anomaly is characterized by the increasing AVO in a sedimentary section and indicates the probability of the presence of hydrocarbons. As opposed to the isotropic case where the velocity remains constant for all incident angles, the velocity is a function of the angle of incidence for anisotropic media and motivates the author to analyze the effect of rock anisotropy on the R and T coefficients of seismic waves. To achieve this purpose, first

the SH-wave is considered, due to its simplicity for VTI media. The effect of Thomsen parameter γ on the R coefficients is delineated presently. In continuing this, the three models characterized by Class 1, 2 and 3 type of Gas-sand anomalies are considered for observing the influence of anisotropy on P-wave reflectivity and to test the accuracy of the plane wave R coefficients. A test of accuracy of the popular Rüger's approximation (Rüger, 2001) is also delineated here.

4.2 Introduction

The travel time of a signal from the surface to and from a reflector and the amplitude of the reflection comprise the seismic response. The reflection coefficient plays an important role in order to interpret the field records for lithology, porosity and fluid content etc (Upadhyay, 2004). Thus, the amplitude of the reflection attains more intension of Geoscientists. For isotropic media, the amplitude of the reflection is a function of the density, compressional and shear wave velocities of the two layers that make up the interface and the angle of incidence (Shearer, 1999). The velocity of isotropic media remains constant during the AVO analysis while velocity of anisotropic media varies with the angle of incidence and interrupt the AVO analysis (Rüger, 2001). In order to analyze the effect of anisotropy on the R and T coefficients, a VTI model is taken into account due to its simplicity among anisotropic media beyond the isotropic media. The thinly layered media with horizontal interfaces and horizontally stratified shale formations are characterized by the VTI model (Thomsen, 2002). For VTI media, the wave equation separates into a coupled pair of equations for the P-SV waves and into a single equation for the pure SH-wave (Slawinski, 2003). Further, VTI media possess z axis as axis of symmetry so there is no loss of generality in considering propagation in any plane. First I discuss the plane wave R and T coefficients of SH-wave for VTI media. Then I consider

the plane wave R and T coefficients of P- and SV-wave as an extension of preceding work.

4.3 R and T coefficients of SH wave for VTI media

In the past, R and T coefficients have been obtained in several domains according to their importance. Further, considering anisotropy in seismic exploration, the R and T coefficients have been obtained in terms of the phase angle and material properties on either side of the interface (Daley and Hron, 1977). Presently, I derive the R and T coefficients in the plane wave domain in behalf of the efficiency in terms of the computational time for Rayleigh Sommerfeld Modeling(RSM) (Sharma and Ferguson, 2009b). Along with this, some times R and T coefficients are required for use in reflectivity programs where integration over the ray parameter is required (Rüger, 2001). For this case, parameterization by the phase angle can be inconvenient. This inconvenience can be avoided by deriving the R and T coefficients in terms of the ray parameter. To do this, I compute the ray parameter using the effective ray parameter approach (Sharma and Ferguson, 2009b) and is used to compute the corresponding R and T coefficients in the plane wave domain.

In general, the reflected and transmitted waves are generated by an incident wave when an interface is encountered. The amplitude of the reflected and transmitted waves depend on the R and T coefficients (Krebes, 2008). In order to obtain the R and T coefficients boundary conditions, the continuity of displacement and traction, are considered at the boundary. After applying the boundary conditions, the R and T coefficients for anisotropic media are obtained in terms of the effective ray parameter and the elastic constant and can be written as (Slawinski, 2003)

$$R_{SH} = \frac{c_{44}^1 q_1 - c_{44}^2 q_2}{c_{44}^1 q_1 + c_{44}^2 q_2}, \quad (4.1)$$

and

$$T_{SH} = \frac{2 c_{44}^1 q_1}{c_{44}^1 q_1 + c_{44}^2 q_2}, \quad (4.2)$$

where c_{44}^1 and c_{44}^2 are the elastic constants of the incident and the refracted media. c_{44}^1 can be related to Thomsen's parameter as (Thomsen, 2002)

$$c_{44}^1 = \rho_1 (\beta_{01})^2, \quad (4.3)$$

and c_{44}^2 is described as

$$c_{44}^2 = \rho_2 (\beta_{02})^2, \quad (4.4)$$

where ρ and β are the density and the vertical shear wave velocity. In the subscripts the first digit indicates the shear wave propagation direction with respect to the vertical and the second digit indicates the medium. The incident and the refracted medium are characterized by indices 1 and 2, respectively. Following equations 4.3 and 4.4, the reflection and transmission coefficients can be described as

$$R_{SH} = \frac{\rho_1 \beta_{01}^2 q_1 - \rho_2 \beta_{02}^2 q_2}{\rho_1 \beta_{01}^2 q_1 + \rho_2 \beta_{02}^2 q_2}, \quad (4.5)$$

and

$$T_{SH} = 2 \frac{\rho_1 \beta_{01}^2 q_1}{\rho_1 \beta_{01}^2 q_1 + \rho_2 \beta_{02}^2 q_2}, \quad (4.6)$$

where q_1 is the vertical slowness for SH wave in the incident medium and can be written as (Ferguson and Margrave, 2008)

$$q_1 = \sqrt{\beta_{01}^{-2} - p_I^2 (2\gamma_1 + 1)}, \quad (4.7)$$

and the vertical slowness of the refracted medium q_2 is described as

$$q_2 = \sqrt{\beta_{02}^{-2} - p_I^2 (2\gamma_2 + 1)}, \quad (4.8)$$

where γ_1 and γ_2 are the Thomsen's parameters of the incident and the refracted medium. p_I is the effective ray parameter and can be computed as

$$p_I = |\hat{\mathbf{p}} \times \hat{\mathbf{a}}| \sqrt{p_1^2 + p_2^2 + q^2}, \quad (4.9)$$

where p_1 , p_2 and q are the horizontal components 1, 2 and the vertical component of the slowness vector, respectively and these are evaluated in the incident medium. The slowness vector $\hat{\mathbf{p}}$ characterizes the direction of the incident wavefield and can be computed using equation 2.1 while unit normal vector $\hat{\mathbf{a}}$ associated with TTI symmetry plane is computed according to equation (3.22).

4.4 Reflection and Transmission coefficients for P-SV wave

Historically, the P-SV reflection and transmission coefficients of an isotropic media has been studied by numerous authors (Aki and Richards, 1980; Kennett, 2001). Further, Daley and Hron have extended this study for anisotropic media (Daley and Hron, 1977). Using the zeroth order approximation to an asymptotic ray series they have published the displacement reflection and transmission coefficients of P-SV waves for VTI media in terms of the elastic coefficients and the phase angle (Daley and Hron, 1977). Accounting for the importance of the plane wave reflection and transmission coefficients as delineated in the previous section, here I also derive plane wave P-SV reflection and transmission coefficients. Graebner (Graebner, 1992) has published the reflection and transmission coefficient in terms of the elastic coefficients and the horizontal and the vertical components of the slowness vector. Since Thomsen's parameters for an anisotropic medium play an important role in order to reduce the non uniqueness of the inverse problem where it is needed to model the data in a given geologic environment (Grechka, 2009). Thus, I derive the reflection and transmission coefficients in terms of Thomsen's parameters for seeking the effect of Thomsen's parameters (δ, ϵ) on these coefficients. To do this, I develop a relationship between the elastic constants used by Graebner (Graebner, 1992) and Thomsen's parameters (Thomsen, 1986b). Further, by using the effective ray parameter I obtain 3D reflection and transmission coefficients for VTI media.

To obtain the R and T coefficients, the continuity of the displacement and the stress is required. Consider a P-wave that impinges on the interface and it generates a reflected and refracted P-and SV-wave at the interface. Then, the stress-strain relationship ($\tau = \mathbf{c}\epsilon$) can be expressed as

$$\begin{bmatrix} \tau_{xx} \\ \tau_{yy} \\ \tau_{zz} \\ \tau_{yz} \\ \tau_{zx} \\ \tau_{xy} \end{bmatrix} = \begin{bmatrix} A & A - 2N & F & 0 & 0 & 0 \\ A - 2N & A & F & 0 & 0 & 0 \\ F & F & C & 0 & 0 & 0 \\ 0 & 0 & 0 & L & 0 & 0 \\ 0 & 0 & 0 & 0 & L & 0 \\ 0 & 0 & 0 & 0 & 0 & N \end{bmatrix} \begin{bmatrix} \epsilon_{xx} \\ \epsilon_{yy} \\ \epsilon_{zz} \\ 2\epsilon_{yz} \\ 2\epsilon_{zx} \\ 2\epsilon_{xy} \end{bmatrix}, \quad (4.10)$$

where $\epsilon_{ij} = \frac{1}{2}(\partial u_i / \partial x_j + \partial u_j / \partial x_i)$, and $i, j = x, y, z$ or $1, 2, 3$. The τ_{ij} are the stresses, the ϵ_{ij} are the strains, the u_i are the components of particle displacement and the A, C, F, L and N are the elastic constants. Now, the substitution of the plane wave particle displacement equation into the wave equation yields the eigenvalues (phase velocities) of the P- and SV-waves. Once the eigenvalues are known, the corresponding eigenvectors can be obtained as a function of the elastic coefficients and the horizontal and the vertical slownesses. On being acquainted with the eigenvalues and the eigenvectors of the P- and SV-waves, the R and T coefficients are obtained after implementation of the boundary conditions at the interface and can be expressed in matrix form as $\mathbf{S}\mathbf{x} = \mathbf{b}$. For this case the matrix \mathbf{S} is given by

$$\mathbf{S} = \begin{bmatrix} \left(l_{\alpha_1} & m_{\beta_1} & -l_{\alpha_2} & -m_{\beta_2} \right) \\ m_{\alpha_1} & -l_{\beta_1} & m_{\alpha_2} & -l_{\beta_2} \\ a_1 & b_1 & a_2 & b_2 \\ c_1 & d_1 & -c_2 & -d_2 \end{bmatrix}, \quad (4.11)$$

where $a_i=L_i(q_{\alpha_i}l_{\alpha_i}+p_I m_{\alpha_i})$, $b_i=L_i(q_{\beta_i}m_{\beta_i}-p_I l_{\beta_i})$, $c_i=p_I l_{\alpha_i}F_i+q_{\alpha_i}m_{\alpha_i}C_i$, and $d_i=p_I m_{\beta_i}F_i-q_{\beta_i}l_{\beta_i}C_i$, and $i=1$ corresponds to the upper medium and $i=2$ indicates the lower medium. The l_{α} , m_{α} are the eigenvectors of the P-wave and the l_{β} , m_{β} are the eigenvectors of the SV-wave and can be expressed as

$$l_k = \sqrt{\frac{(C'q_k^2 + L'p_I^2 - 1)}{(A'p_I^2 + L'q_k^2 - 1) + (C'q_k^2 + L'p_I^2 - 1)}}, \quad (4.12)$$

and

$$m_k = \sqrt{\frac{(A'p_I^2 + L'q_k^2 - 1)}{(A'p_I^2 + L'q_k^2 - 1) + (C'q_k^2 + L'p_I^2 - 1)}}, \quad (4.13)$$

where $k=1$ characterize the P-wave and the SV is characterized by the $k=2$ and $A'=A/\rho$, $L'=L/\rho, C'=C/\rho$. Now the vectors, \mathbf{x} and \mathbf{b} , are given by

$$\mathbf{x} = \begin{bmatrix} r_{pp} \\ r_{ps} \\ t_{pp} \\ t_{ps} \end{bmatrix}, \quad (4.14)$$

and

$$\mathbf{b} = \begin{bmatrix} \left(\begin{array}{c} -l_{\alpha_1} \\ m_{\alpha_1} \\ L_1 (q_1 l_{\alpha_1} + p_I m_{\alpha_1}) \\ -p_I l_{\alpha_1} F_1 - q_{\alpha_1} m_{\alpha_1} C_1 \end{array} \right) \end{bmatrix}, \quad (4.15)$$

In above equations p_I is the effective ray parameter and is computed with equation 2.5. q_{α} and q_{β} are the vertical slowness of the P- and SV-wave, respectively and can be computed using equations B.1, B.2, B.3 and B.4. The elastic coefficient matrix for VTI media can

be expressed as (Tsvankin, 2001)

$$c_{VTI} = \begin{bmatrix} \left(\begin{array}{cccccc} c_{11} & c_{11} - 2c_{66} & c_{13} & 0 & 0 & 0 \\ c_{11} - 2c_{66} & c_{11} & c_{13} & 0 & 0 & 0 \\ c_{13} & c_{13} & c_{33} & 0 & 0 & 0 \\ 0 & 0 & 0 & c_{44} & 0 & 0 \\ 0 & 0 & 0 & 0 & c_{44} & 0 \\ 0 & 0 & 0 & 0 & 0 & c_{66} \end{array} \right) \end{bmatrix}. \quad (4.16)$$

The comparison of the elastic stiffness matrix from equation 4.10 with the above equation yields the relationship

$$c_{11} = A, c_{44} = L, c_{33} = C, c_{55} = L,$$

and

$$c_{12} = c_{11} - 2c_{66}. \quad (4.17)$$

Moreover, Thomsen's parameters are defined as follow: The vertical P-wave velocity is characterized by

$$\alpha_0 = \frac{\overline{c_{33}}}{\rho}, \quad (4.18)$$

and S-wave velocity along the vertical axis of symmetry can be defined by

$$\beta_0 = \frac{\overline{c_{44}}}{\rho}, \quad (4.19)$$

and anisotropy can be characterized by the dimensionless coefficients

$$\epsilon = 1/2 \frac{c_{11} - c_{33}}{c_{33}}, \quad (4.20)$$

$$\gamma = 1/2 \frac{c_{66} - c_{44}}{c_{44}}, \quad (4.21)$$

and

$$\delta = 1/2 \frac{(c_{13} + c_{44})^2 - (c_{33} - c_{44})^2}{c_{33} (c_{33} - c_{44})}. \quad (4.22)$$

By considering the equations (4.17 to 4.22), it can be demonstrated that

$$A = \rho \alpha_0^2 (1 + 2\epsilon), C = \rho \alpha_0^2, L = \rho \beta_0^2, N = \rho \beta_0^2,$$

and

$$F = \rho \frac{\alpha_0^2 - \beta_0^2}{(2\delta + 1)\alpha_0^2 - \beta_0^2} - \rho \beta_0^2. \quad (4.23)$$

Once this relationship is built and is used in the above equations, the corresponding R and T coefficients are obtained in terms of Thomsen's parameters.

4.5 Example

Now following the equations from 4.1 to 4.9 as discussed above, I obtain the reflection and transmission coefficients of SH-wave in the plane wave domain for interfaces between two VTI media. To authenticate the proposed approach, I obtain the reflection and transmission coefficients for a isotropic medium by employing a constraint on γ ($\gamma = 0$) in equations 4.5 and 4.6 since $\gamma=0$ corresponds to the isotropic case. Figure 4.1 shows the real and imaginary parts of the 3D reflection and transmission coefficients obtained by applying a constraint $\gamma=0$ on the anisotropic algorithm. Figure 4.2 shows the 3D reflection and transmission coefficients by following the isotropic algorithm as discussed in Chapter2 and is the facsimile of Figure 4.1. Further, the corroboration is attained by consider the in-line slices and the cross-line slices of the reflection and transmission coefficients and are shown in Figure 4.3a, b, c and d. The results obtained by following the anisotropic and isotropic algorithms are denoted by the red and the green colors, respectively, and the overlapping of these results ensure the efficacy of the proposed approach of obtaining R and T coefficients in the plane wave domain.

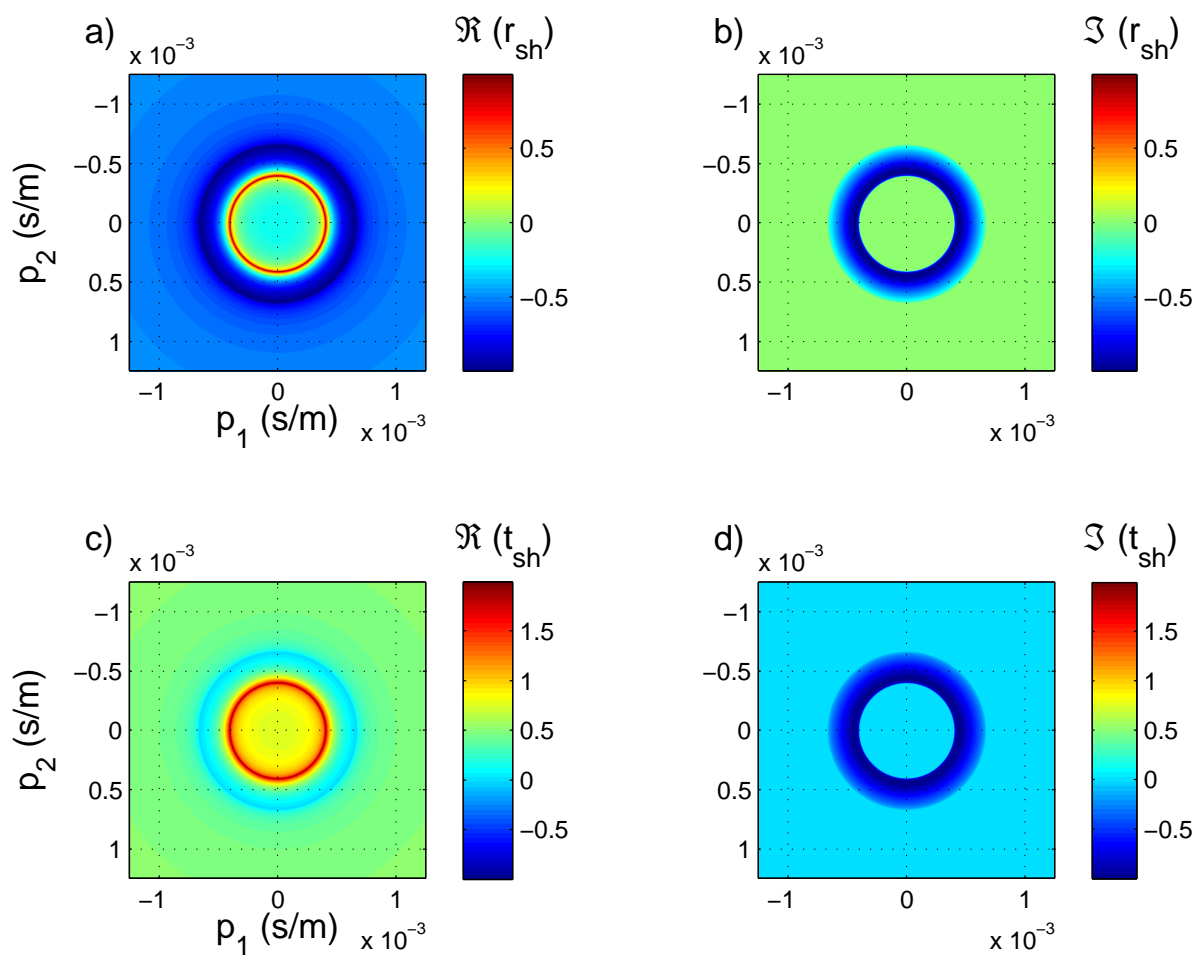


Figure 4.1: a) Real part of reflection coefficient. b) Imaginary part of reflection coefficient. c) Real part of transmission coefficient. d) Imaginary part of transmission coefficient, obtained from the anisotropic algorithm by applying constraint ($\gamma = 0$) on it.

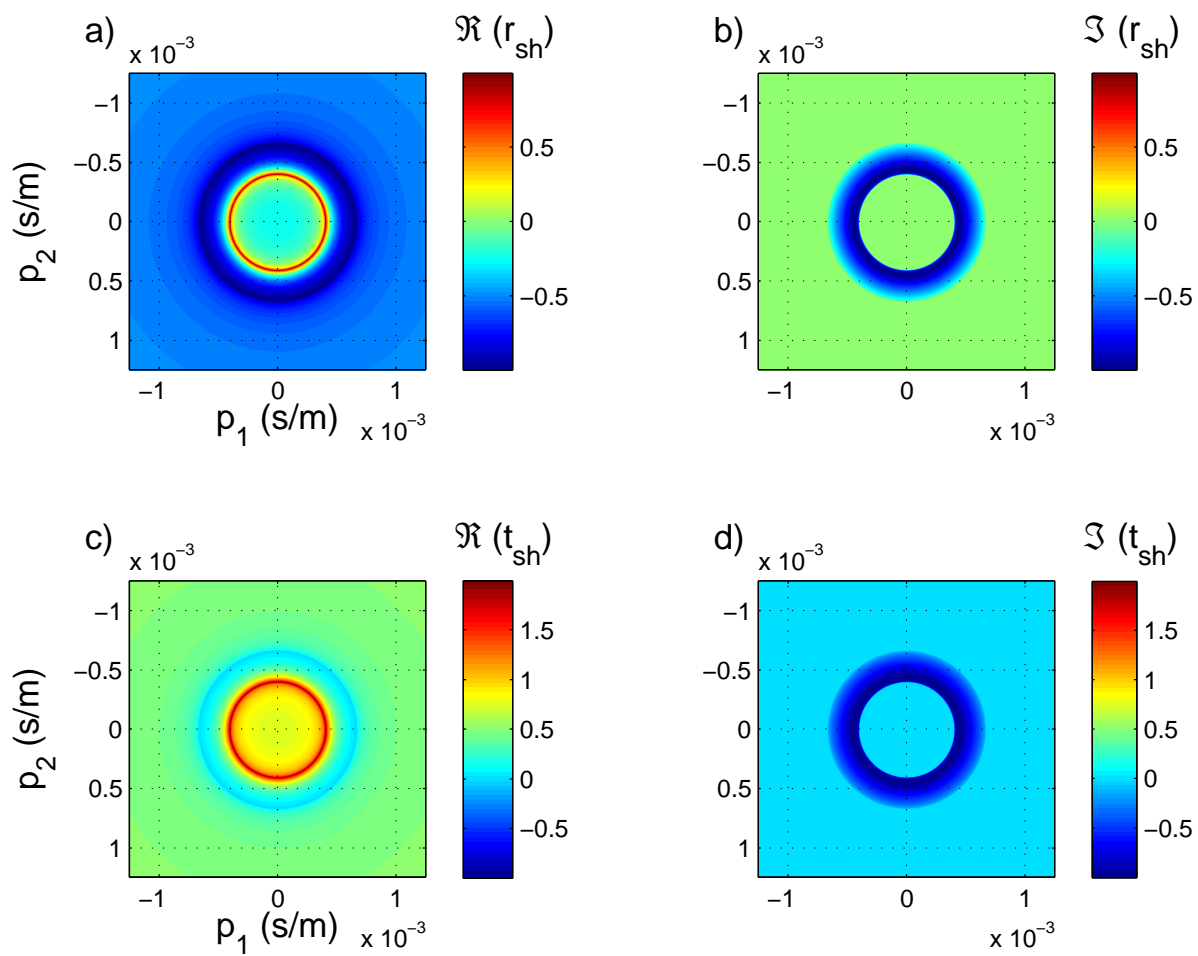


Figure 4.2: a) Real part of reflection coefficient. b) Imaginary part of reflection coefficient. c) Real part of transmission coefficient. d) Imaginary part of transmission coefficient, obtained from the isotropic algorithm.

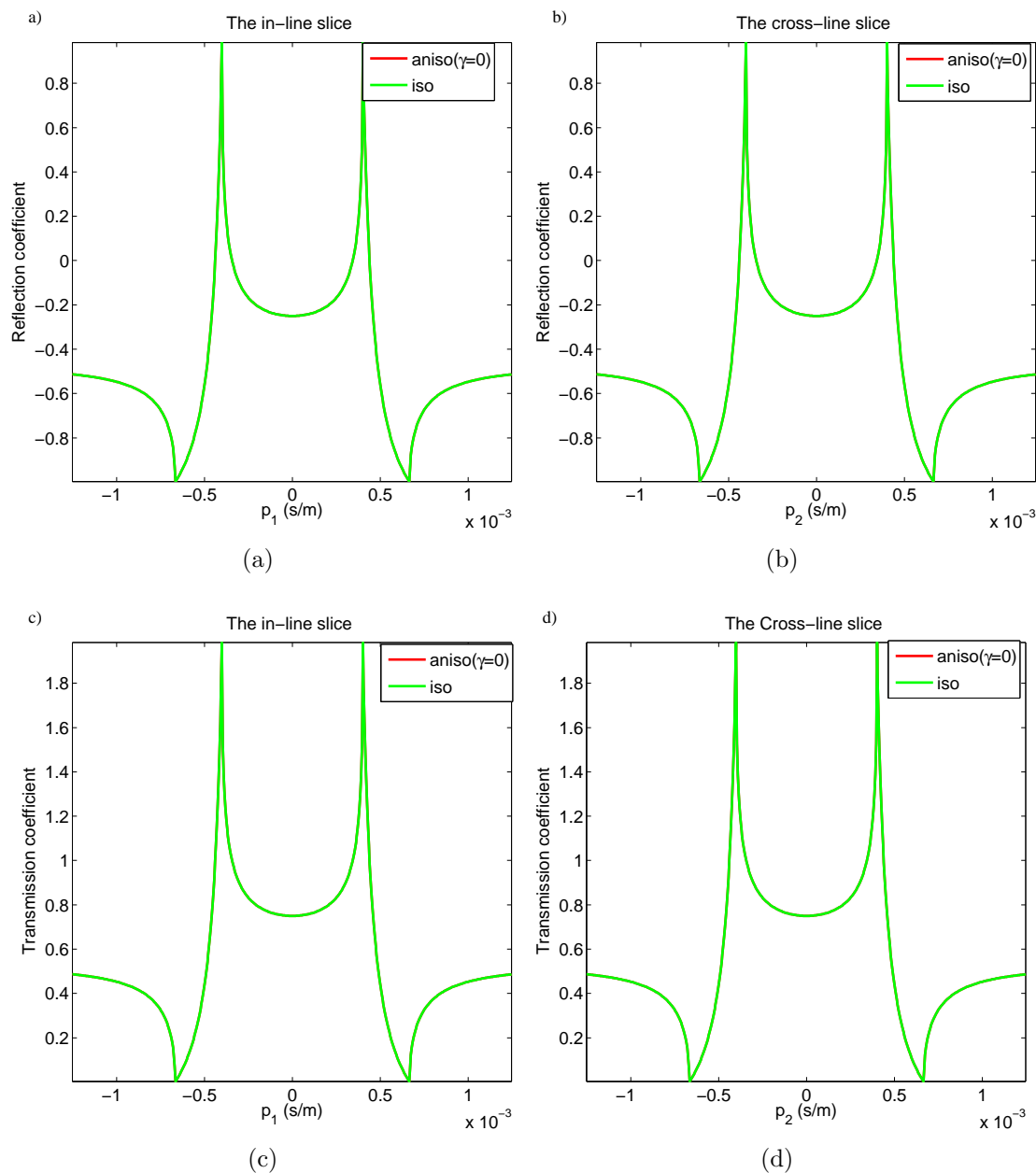


Figure 4.3: (a) The in-line (b) The cross-line slices of the SH wave R coefficients. (c) The in-line (d) The cross-line slices of the SH wave T coefficients. The red line denotes the coefficients obtained by degenerated anisotropic algorithm and the green line shows the isotropic coefficients. The overlapping of these curve endorse the efficacy of the anisotropic algorithm for isotropic media.

As it is known that AVO analysis considers the amplitude variation for the pre-critical propagation (Rüger, 2001), I consider this condition in order to analyze the influence of Thomsen's parameter on the AVO analysis. To do this, the upper medium is characterized by the invariant vertical velocity and the variable γ and the lower medium possess the covariant Thomsen's parameters. Now two cases for the lower medium : (1) when the vertical velocity of the lower medium exceeds the vertical velocity of the upper medium. (2) The reverse to the first case , are considered. Then, four sub-cases (i) $\gamma_1=\gamma_2=0$ (ii) $\gamma_1 \neq 0$ and $\gamma_2=0$ (iii) $\gamma_2 > \gamma_1$ (iv) $\gamma_2 < \gamma_1$ have been taken into account. Figure 4.4 shows the reflection coefficient curves as a function of the horizontal slowness for the first case with four sub-cases. It is seen that at zero slowness the reflected wave has negative amplitude as expected since the velocity of the lower medium is greater than the velocity of the upper medium. Then iso/iso curve follows the expected behavior. While, the change between the reflection coefficient values, as well as the change of the slope of the reflection coefficient, is significant among the individual sub-cases for the first case. Only for zero slowness (normal incidence) do the curves coincide. The slope of the reflection coefficients for aniso/iso and aniso γ_1 /aniso($\gamma_2 < \gamma_1$) sub-cases is less than the slope of the iso/iso. As $\gamma > 0$ corresponds to the velocity increment with slowness, for the aniso/iso situation the velocity of the upper medium increases with slowness while the lower medium's velocity remains constant hence the numerator of the equation 4.5 attains the lesser value and the denominator has larger values than the values obtained for iso/iso situation. Both factors, together, allow us to except the obtained pattern of the reflection coefficient curve. Further, for the aniso γ_1 /aniso($\gamma_2 < \gamma_1$) scenario, the obtained reflection coefficient curve lies in between the previous two situations. The obtained reflection coefficient curve for the fourth sub-case shows more deviation from the obtained curve of the isotropic-isotropic situation as the velocity of the lower medium increases more rapidly than the upper medium in this case.

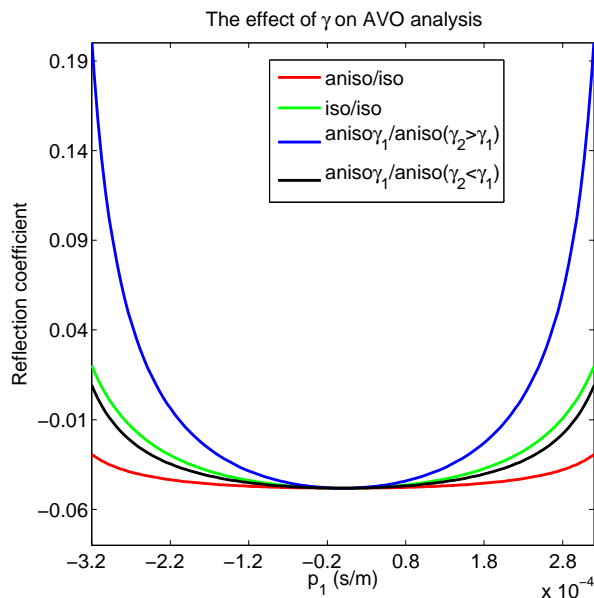


Figure 4.4: The variation of R coefficient with horizontal slowness for the different interfaces illustrates that anisotropy does have a considerable influence on the AVO analysis.

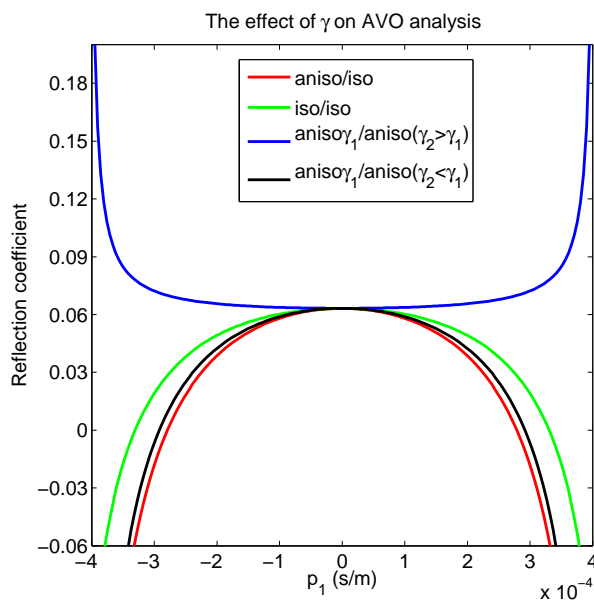


Figure 4.5: The influence of the Thomsen's parameter γ on the AVO analysis as shown in Figure 4.4 for different model.

Figure 4.5 shows the reflection coefficient curves as a function of the horizontal slowness for the second case with four sub-cases. Again the change between the reflection coefficient values, as well as the change of the slope of the reflection coefficient, is significant among the individual sub-cases. However, as indicated in the above examples, ignoring the presence of anisotropy in VTI media has the potential of severely distorting the AVO analysis.

Now following the theory delineated above in the reflection and transmission coefficient for P-SV section, I implement an algorithm based on equations 4.11 to 4.23 in order to compute the reflection and transmission coefficients for VTI media. Prior to anisotropy considerations, I compute the reflection coefficients of the seismic waves for isotropic media by using the anisotropic algorithm while applying the constraint ($\delta, \epsilon = 0$). Moreover, reflection coefficients are obtained using the isotropic algorithm based on the Zoeppritz equations in order to substantiate to the anisotropic algorithm (Shearer, 1999). However a complete set of the reflection and transmission coefficients are required for accomplishing the 3D modeling but only the reflection coefficients of P-P and SV-SV are considered presently in behalf of the complexity of the reflection and transmission curves for this case. Figure 4.6a, b show the real and imaginary parts of the reflection coefficients of the reflected P and SV waves when incident P and SV waves are considered, respectively, and are obtained by the implementation of degenerated anisotropic and isotropic algorithms. The overlapping of these curves show the feasibility of the anisotropic algorithm for isotropic media. To obtain these figures, the interface of the two isotropic media has been considered which follow the condition $\alpha_1 < \alpha_2$, $\beta_1 < \beta_2$ and $(\beta_1, \beta_2) < (\alpha_1, \alpha_2)$ where α_i and β_i are the P and SV waves respectively. $i = 1$ corresponds to the upper medium and the lower medium is characterized by $i = 2$. For this condition, it is known that when the P-wave encounters the interface for the four cases, namely, pre-critical, critical1, critical2, post-critical arise in this situation and can be defined on the basis

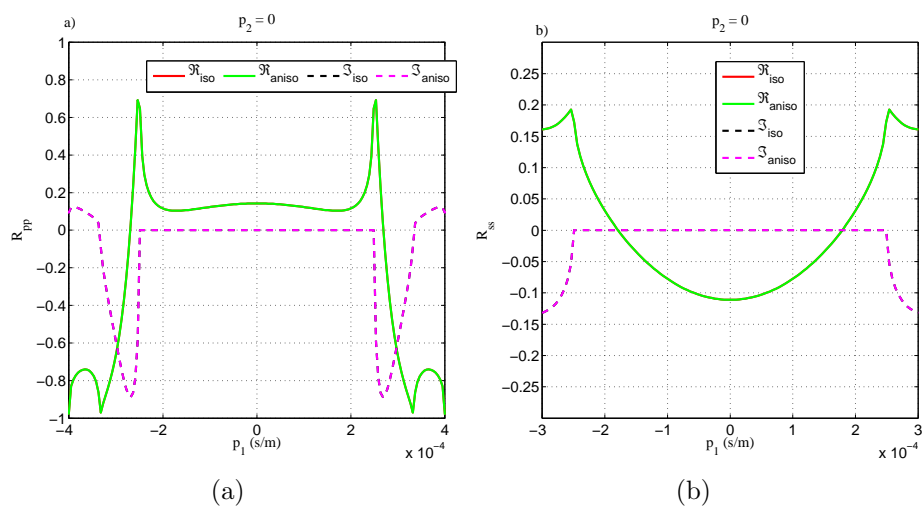


Figure 4.6: (a) The real and imaginary part of the R coefficients for (a) P-P (b) S-S cases. The green line denotes the coefficients obtained by degenerated anisotropic algorithm and the red line shows the isotropic coefficients. The dotted black and magenta lines indicates the imaginary part of the R coefficients obtained by the degenerated anisotropic algorithm and isotropic algorithms, respectively. The overlapping of these curve endorse the efficacy of the anisotropic algorithm for isotropic media.

of the maximum slowness possessed by the body waves in the lower medium. However, reflection and transmission coefficients of the P and SV waves remain real in pre-critical situations while becoming complex beyond the pre-critical, so I will consider only the pre-critical scenario for further study. Also it is known that the better quality and lower cost of acquisition and processing of the compressional wave data than the shear wave data make the exploration community more sophisticated in the acquisition and processing of the P-wave data. In the following section, I will consider only P-P reflectivity for seeking the effect of anisotropy.

In order to test the accuracy of the plane wave domain reflection coefficient the three models characterized by the class 1, 2 and 3 type of Gas-sand anomaly, respectively are considered. The model parameters used presently are taken from Rüger (Rüger, 2001) and has been published before also by Kim. Further, a test of the accuracy of the popular approximation given by Rüger is also considered here. Figure 4.7 shows the P wave reflectivity with horizontal slowness for a isotropic media. It is indicated from this figure that curves obtained by the exact algorithms of the isotropic media and VTI media are analogous to each other while an approximation of Rüger provides a close match to the exact solutions near the zero horizontal slowness and deviates from the exact solution as slowness increases. The overlapping of the plane wave reflection coefficients obtained by the exact isotropic and degenerated anisotropic algorithms establish the accuracy of the approach followed by the author. Further, the overlap of the obtained exact reflection coefficient with the reflection coefficient obtained by applying Rüger's approximation near to the horizontal slowness can be treated as supportive results in favor of the the accuracy of the exact plane wave reflection coefficient given by equations 4.11, 4.12, 4.13, 4.14 and 4.15. To illustrate the effect of the anisotropy on the P-P reflectivity and the accuracy of Rüger's approximation's, I show the P-wave reflection coefficients for the same three models as used previously but now the VTI symmetry has been introduced

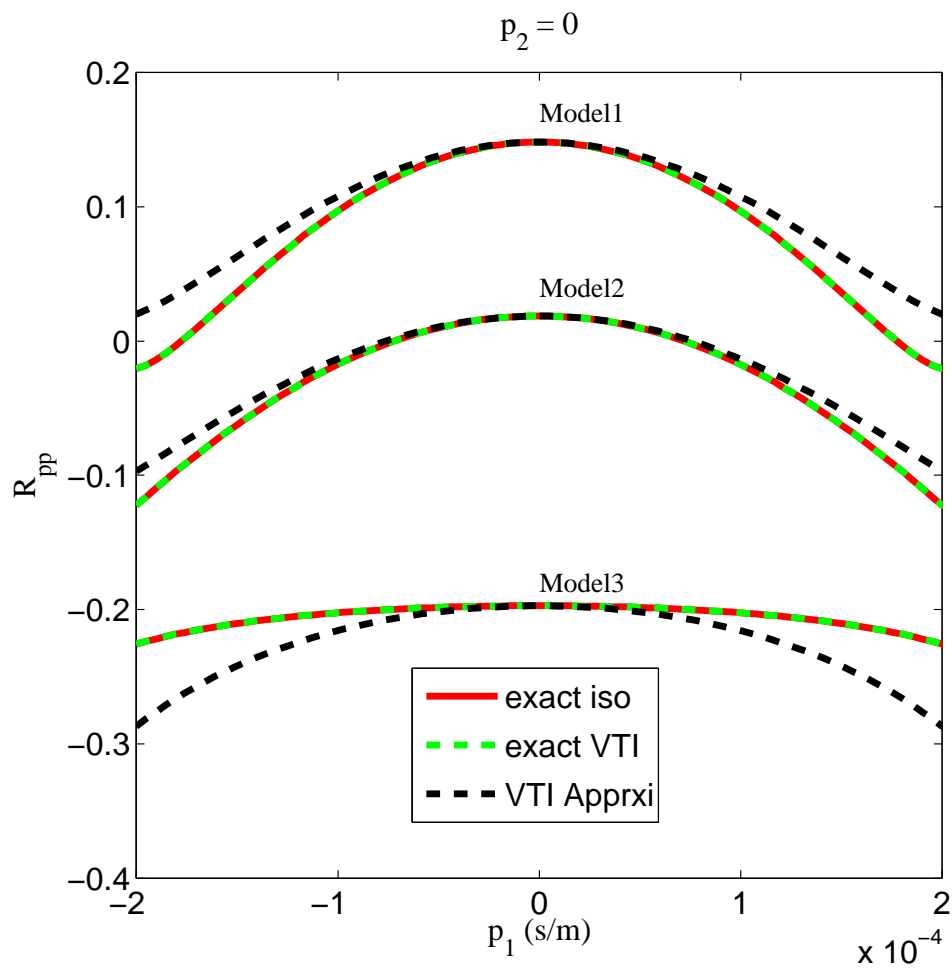


Figure 4.7: P wave reflection coefficients computed for three shale/gas-sand interfaces. The solid red lines indicate the exact solutions and the dashed green and black lines show the solutions computed by exact VTI and Rürger's approximated algorithms for isotropic medium, respectively.

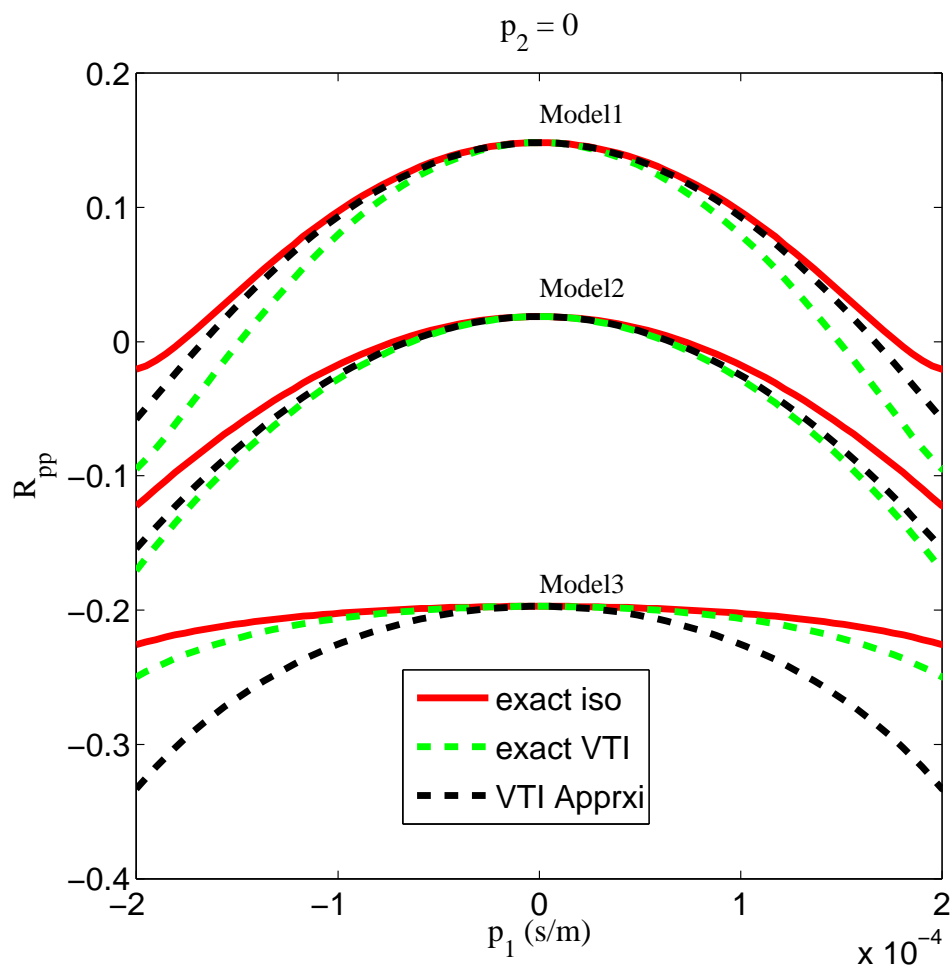


Figure 4.8: The reflection coefficients curves of the P wave for the three models shown in appendix. The thick red line denotes the exact isotropic reflection coefficient, the dashed green and black lines show the exact and approximated reflection coefficients after introducing vertical transverse isotropy into the shale overburden with anisotropic parameters ($\delta = 0.12$, $\epsilon = 0.133$)

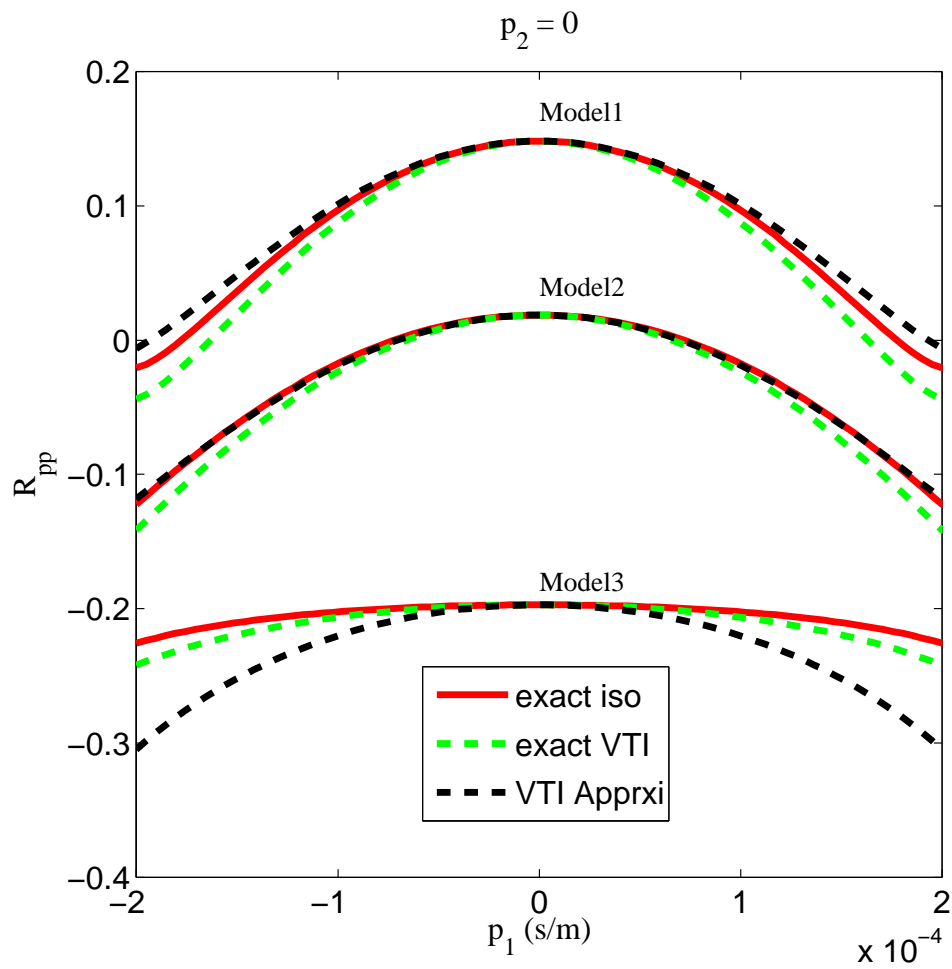


Figure 4.9: In order to seek the influence of the ϵ on the reflection coefficients, the same reflection coefficient curves of the P wave as the ones shown in Figure 4.8 but for a zero ϵ in the shale layer ($\delta = 0.12, \epsilon = 0$)

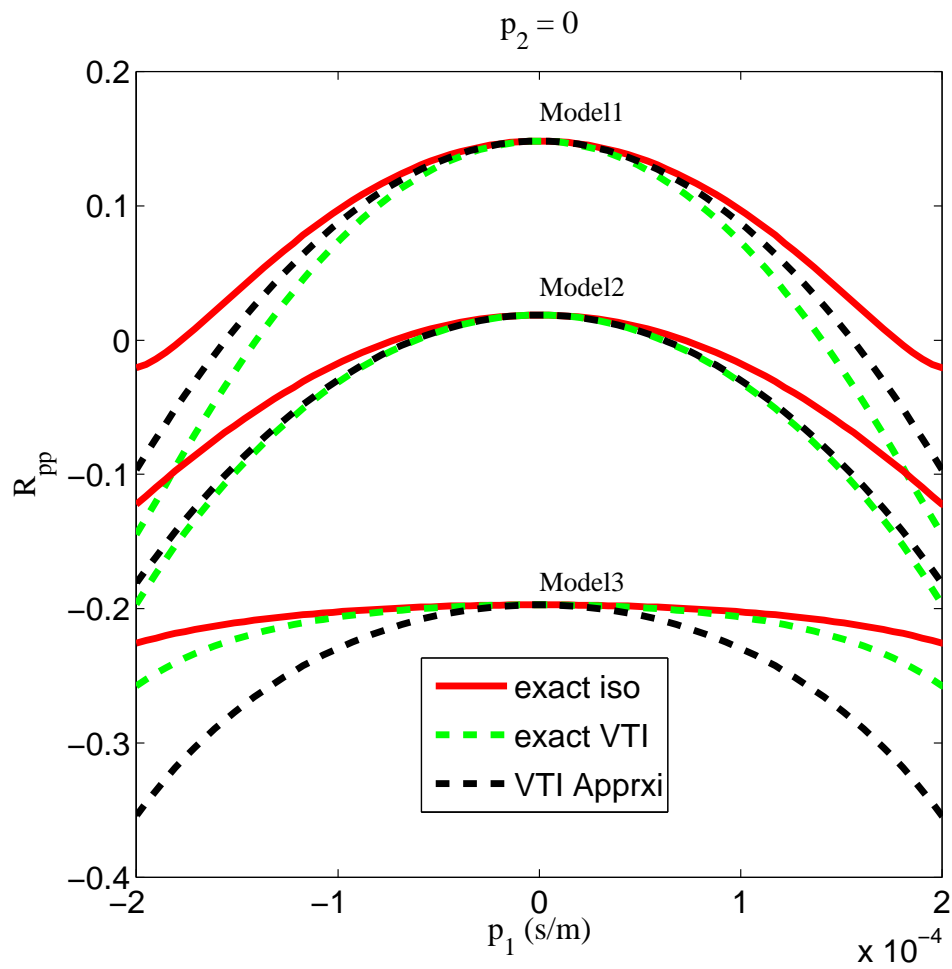


Figure 4.10: The same P wave reflection coefficient curves as shown previously in Figures 4.8 and 4.9 but for a VTI medium characterized by anisotropic parameters ($\delta = 0.12, \epsilon = 0.233$)

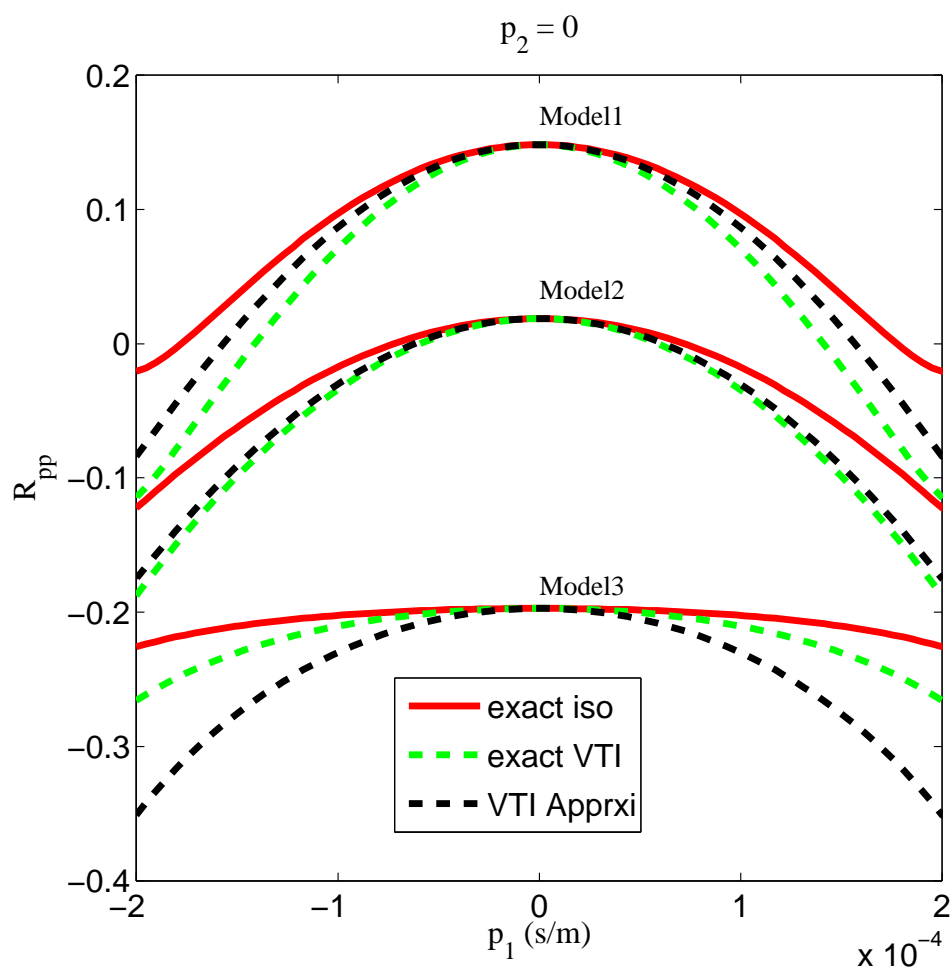


Figure 4.11: P wave reflection coefficient curves for the same three models but for a positive value of δ in the shale layer ($\delta = 0.24, \epsilon = 0.133$)

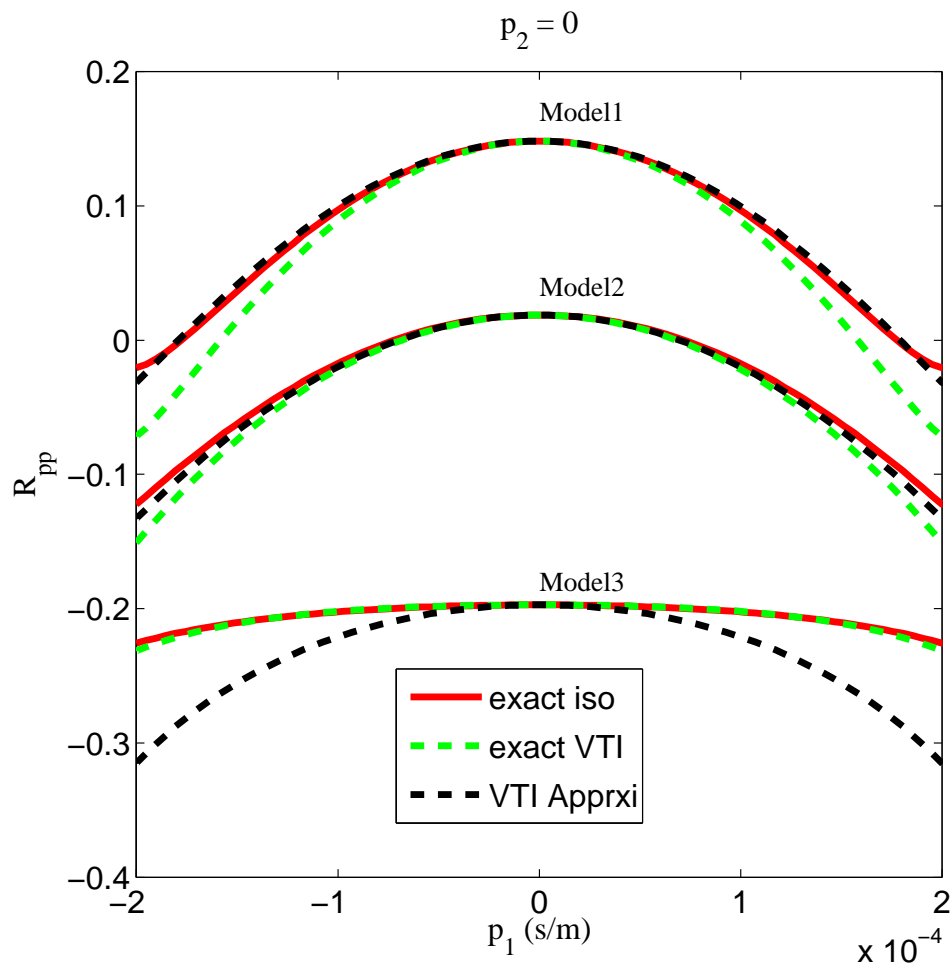


Figure 4.12: In order to seek the influence of the δ on the reflection coefficients, the same reflection coefficient curves of the P wave as the ones shown in Figure 4.11 but for a zero δ in the shale layer ($\delta = 0, \epsilon = 0.133$)

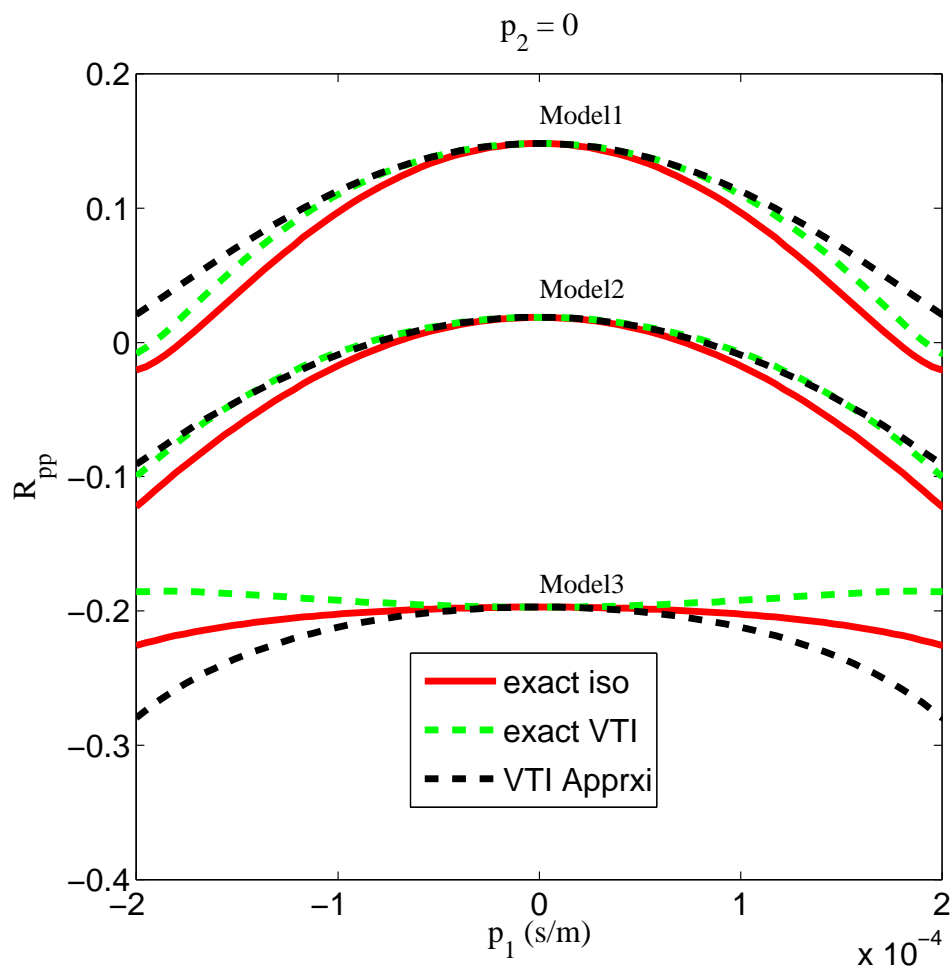


Figure 4.13: The same P-wave reflection coefficient curves as the ones shown in Figure4.11, but for a negative value of anisotropy(negative δ in the overburden ($\delta = -0.24, \epsilon = 0.133$))

into the overburden shale by considering the anisotropic parameters ($\epsilon = 0.133, \delta = 0.12$). Figure 4.8 illustrates the effect of the anisotropy on the P-P reflection coefficient and accuracy of Rüger's approximation as exact VTI reflection coefficients are compared with the corresponding isotropic reflection coefficients ($\epsilon = 0, \delta = 0$) and VTI approximated reflection coefficients. This figure shows that the behavior of the reflection coefficient curve can be changed substantially in the presence of anisotropy. It is also depicted that the VTI approximation's results do match perfectly with the exact one at the zero horizontal slowness and closely near to it. Meanwhile, the deviation of the approximated reflection coefficient curve from the exact one, as horizontal slowness increases, is also observed. It's also noticed that the approximation and the exact reflection curves are close to each other for the first two models. The accuracy of Rüger's approximation is lower for the third model. In this case it is shown that the anisotropy has the largest influence on the reflection coefficient for higher values of slowness. Further, the examples are repeated for two different values of anisotropy parameters ($\epsilon = 0$ and $\epsilon = 0.233$) in Figures 4.9 and 4.10, respectively. By examining these figures it is observed that the difference between the curves are restricted to the large values of slowness but the accuracy of the approximation remains unchanged near to and at the horizontal slowness. Other examples are considered for three different values of anisotropy parameters ($\delta = 0.24, \delta = 0$ and $\delta = -0.24$) with a constant value of $\epsilon = 0.133$ for observing the influence of delta on the reflection coefficient curves. These examples are shown in the Figures 4.11, 4.12 and 4.13. A close investigation of these Figures makes it possible to illustrate that anisotropy influences the P-wave reflection coefficient in a considerable manner and the difference between the curves near zero horizontal slowness is governed by the anisotropy parameter δ .

4.6 Conclusions

I have presented the plane wave reflection coefficient of the SH and P-SV waves for anisotropic media by following Graebner's approach and using the effective ray parameter approach in order to accomplish the full elastic wave modeling for anisotropic media in behalf of its efficiency in the plane wave domain. The authentication of the obtained plane wave reflection coefficient of P-wave has been described in reference to isotropic reflection coefficient and Rüger's approximated reflection coefficient. Further, it has been observed that anisotropy influences the solution for the SH-wave reflection coefficient through the contrast in the anisotropy parameter γ across the boundary. It has been demonstrated that anisotropy does not have any effect on the reflection coefficient of the normally incident waves. For the P-P case, the parameter δ governs the pattern of the reflection coefficient near zero slowness and ϵ is responsible for the behavior of the obtained reflection coefficient at the large values of the horizontal slowness. These observations are a manifestation of the well known facts that ϵ governs the influence of anisotropy on the P waves traveling near horizontally and δ dominates near vertical wave propagation. If there is no contrast in Thomsen's parameters (ϵ, δ) across the interface, the reflection coefficients obtained from the exact anisotropic algorithm by putting a constraint $(\epsilon, \delta = 0)$ on it, coincides with those obtained from the purely isotropic algorithm. Meanwhile the reflection coefficients obtained from Rüger's approximation do match with the exact one at and near to the zero horizontal slowness. Finally, these analysis of the effect of anisotropy on the reflectivity of the body waves, indicate that conventional AVO analysis needs to be modified in the presence of anisotropy on either side of the interface. Since there is a considerable difference between the reflection coefficient curve obtained from the exact and approximated algorithms at large values of the horizontal slowness and this difference may also be noticeable near zero slowness in the presence of

strong anisotropy, we should deal with the more exact algorithm so that the scanty of the accuracy could be avoided.

Further, as the dependency of the reflected waves amplitude on offset has proven to be a valuable exploration tool for direct hydrocarbon detection, I have demonstrated that anisotropy does have a considerable influence on the R coefficient of seismic waves. Thus conventional AVO analysis needs to be modified in the presence of the anisotropy on either side of the reflecting boundary. A test of accuracy of Rüger's approximation is also delineated here.

Chapter 5

Phase shift modelling for HTI media.

5.1 Summary

Fractures play an important role in hydrocarbon production as they determine the pathways and volume of crustal fluid movement. A horizontal transverse isotropic (HTI) medium is the simplest effective model of a formation that contains a single parallel fracture system. By following the same theory as discussed in the previous chapter, I present phase shift modelling in order to seek the dynamic and kinematic signature of seismic waves in HTI media as these analysis can be useful for fracture analysis. The only difference in this case resides on the way of computing the polarization angle of the incident body waves at each grid point at the interface. Consequently, a layer of infinitesimal thickness above the HTI media is taken into account for defining the initial wavefield propagation direction. The incident wavefield propagation direction is governed by the cross product of the unit normal vector in the direction of propagation with the unit normal vector associated with the rotational-symmetry axis. This cross-product yields the effective ray parameter that is the prerequisite for obtaining vertical slowness of the refracted wave in HTI media. On being acquainted with the effective ray parameter and the vertical slowness of the refracted wave in HTI media, the unit normal vector in propagation direction in HTI media is computed and used in the cross-product with the unit normal vector associated with a $3C$ geophone at a grid location. This cross-product leads to the computation of the polarization angle of propagating body waves in HTI media at the interface and nurture to the rotation matrix. Therefore, the rotation matrix, built on the bases of the polarization angle and azimuth, is applied to the extrapolated wavefield

in order to model $9C$ data. It is observed that the amplitude and travel time of seismic waves are affected by HTI media. The presented $9C-3D$ modelling will contribute to fracture detection from surface seismic data since the information about the fracture system can be extracted from the three dimensional behavior of the shear wave splitting. Subsequently, this modelling will be applicable for VSP and micro-seismicity modelling in the presence of anisotropy.

5.2 Introduction

In recent years, geo-scientist are supposed to explore the different kind of hydrocarbon reservoirs in behalf of increasing demand for oil and gas in the world. Many of the reservoirs, such as carbonates, tight clastic and basement reservoirs, contain a finite population of natural fractures (Zheng, 2006). Further, fractures control the fluid flow rate, which depends on the permeability of the reservoir as it is high in the direction of fractures strike and low across it (Lines, 2004). Consequently, the knowledge of the distribution of the fracture system to geo-scientist and reservoir engineers is the prerequisite for the successful development of these reservoirs. According to geology, a fracture is characterized by a planar discontinuity in rock due to deformation or physical diagenesis (Xiang-Yangi, 1997). The pattern of the fractures depends on the present and history of the stress and it is evident that certain small-scale fractures may be stress aligned and behave as anisotropic media for seismic waves with sufficiently long wavelengths (Peter and Crampin, 1990). These fractures, either having been initially open due to the stress field within Earth at present time or subsequently closed due to mineralization, are important for fluid flow. Since open fractures can provide storage space and passage for flow of oil and gas, they are of interest for hydrocarbon exploration . There are two ways: direct and indirect methods, to measure fractures. Direct measurement is based on the

well-logging or core sampling and has its limitation as it is applicable around the well bore. Thus, indirect measurements are required to delineate fractured reservoir and to optimize the development of the reservoir. Since in most circumstances in depth in-situ fractures are more or less vertical, the simplest effective model of a formation containing a single parallel fracture system is transversely isotropic with a horizontal symmetry axis (HTI) and is considered presently. Figure 5.1 shows the HTI model induced by vertical fractures where the x axis is the axis of symmetry. The plane which possesses the axis of symmetry is known as symmetry axis plane and a plane normal to the symmetry axis plane is characterized by the isotropy plane and both these planes are shown in Figure 5.1. For present day geophysics, the crustal fracture content, distribution and possible alignment is the important subject despite of the complexity of crustal anisotropy. And if we are to comprehend the role of fractures and fluids to monitor hydrocarbon reservoirs for the presence or absence of major fluid pathways, we must understand how seismic waves interact with the fractures and how this interaction can provide an opportunity to extract the fracture information from seismic waves by considering the kinematic and dynamic analysis. In order to accomplish this purpose it is worth while to review wave-field propagation in the transverse isotropic media and it has been done in chapter 3.

Further, prior to the analysis of the dynamic signature of body waves in the transverse isotropic media, it is convenient to understand the difference between the group velocity and the phase velocity.

5.2.1 Group velocity

The group velocity-vector characterizes the direction and speed of energy associated with the wave motion, therefore, is of primary importance in seismic wave modelling and inversion methods. In contrast, the phase velocity is the local velocity with which wavefront propagates in the normal direction to it. For transversely isotropic media, the

Azimuthal Anisotropy (HTI)

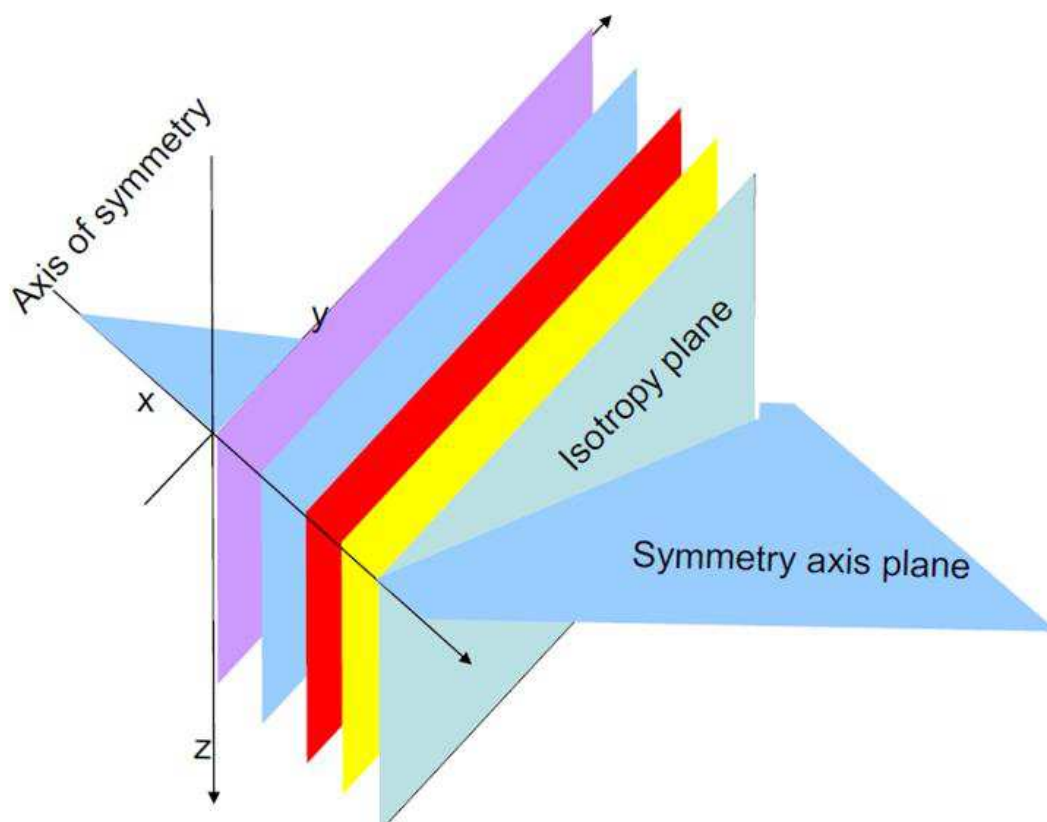


Figure 5.1: Schematic representation of HTI medium induced by vertical fractures where x axis is the axis of symmetry. The plane which possesses the axis of symmetry is known as symmetry axis plane and a plane normal to the symmetry axis plane is characterized by the isotropy plane (Nadri, 2009).

difference between the group and phase velocity vectors are caused by velocity variation with angle. As depicted in Figure 5.2 the group angle (Ψ) represents the direction of the

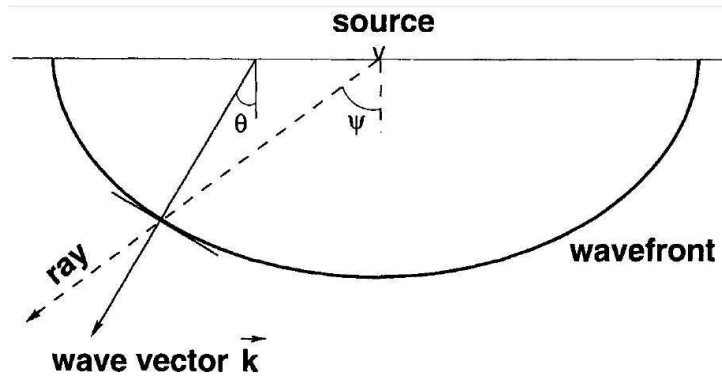


Figure 5.2: Schematic representation of the phase and group angles. The angle is measured with vertical axis. The group angle depicts the direction of energy propagation while phase angle determines the direction of wavefront propagation (Tsvankin:2001).

group velocity vector in a homogeneous medium and it is aligned with the source-receiver direction while the phase angle (θ) is the angle between the wave vector $\tilde{\mathbf{k}}$ and the vertical axis. These angles are different just because of the lack of sphericity of wavefront in the presence of anisotropy. In contrast to phase velocity which can be obtained from the Christoffel equation, group velocity can be computed from the phase velocity function by using this relationship

$$V = \mathbf{g} \cdot \mathbf{n}, \quad (5.1)$$

between the group and the phase velocities. Now to obtain the group velocity from equation 5.1, the spatial direction of the unit wavefront normal \mathbf{n} can be characterized by two directional angles θ_1 and θ_2 . These angles are known as the polar angle and the azimuth of \mathbf{n} , respectively. So the wavefront normal can be computed as

$$\mathbf{n} = [\sin \theta_1 \cos \theta_2, \sin \theta_1 \sin \theta_2, \cos \theta_1], \quad (5.2)$$

The differentiation of equation 5.1 leads the expression

$$\frac{\partial V}{\partial \theta_i} = \mathbf{g} \cdot \frac{\partial \mathbf{n}}{\partial \theta_i} + \frac{\partial \mathbf{g}}{\partial \theta_i} \cdot \mathbf{n} (i = 1, 2), \quad (5.3)$$

By definition \mathbf{n} is the normal to the wavefront, whereas the derivatives $\partial \mathbf{g} / \partial \theta_i$ are tangent to it. Hence, the second term on the right-hand side of the above equation vanishes.

Thus

$$\frac{\partial V}{\partial \theta_i} = \mathbf{g} \cdot \frac{\partial \mathbf{n}}{\partial \theta_i} \quad (i = 1, 2), \quad (5.4)$$

At this moment considering equations 5.1 and 5.4, the component of the group velocity vector can be obtained according to expression

$$\mathbf{g} = V \mathbf{n} + \frac{\partial V}{\partial \theta_1} \frac{\partial \mathbf{n}}{\partial \theta_1} + \frac{1}{\sin^2 \theta_1} \frac{\partial V}{\partial \theta_2} \frac{\partial \mathbf{n}}{\partial \theta_2}. \quad (5.5)$$

This equation leads to the following conclusions

- The magnitude of the group velocity can be defined as

$$g \equiv \|\mathbf{g}\| = \sqrt{V^2 + \left(\frac{\partial V}{\partial \theta_1}\right)^2 + \frac{1}{\sin^2 \theta_1} \left(\frac{\partial V}{\partial \theta_2}\right)^2}. \quad (5.6)$$

Therefore, the inequality $V \leq g$ is satisfied by the phase and group velocities for any wavefront normal \mathbf{n} .

- As it is known that the ray is the unit vector, \mathbf{r} , parallel to the group velocity so it can be defined as

$$\mathbf{r} = \frac{\mathbf{g}}{g}. \quad (5.7)$$

- Following equation 5.1 it can be demonstrated that

$$\mathbf{r} \cdot \mathbf{n} = \frac{V}{g}. \quad (5.8)$$

If $\mathbf{r} = \mathbf{n}$, the ray deviates from the wavefront normal towards the phase velocity increase in accordance with equation 5.5. Figure 5.3 illustrates this geometrically.

From Figure 5.3, it is evident that

$$\cos(\theta - \psi) = \frac{V(\theta)}{V(\psi)} = \frac{V(\theta)}{g(\psi)}, \quad (5.9)$$

Now by considering the right triangle whose hypotenuses is \mathbf{g} and V , $\partial V/\partial\theta$ are the sides and can be illustrated that

$$\tan(\theta - \psi) = \frac{1}{V(\theta)} \frac{dV(\theta)}{d\theta}, \quad (5.10)$$

and the trigonometric identity

$$\tan(x - y) = \frac{\tan x - \tan y}{1 + \tan x \tan y}, \quad (5.11)$$

leads to the relationship between the group angle and the phase angle as

$$\psi = \tan^{-1} \left[\frac{\tan \theta + \frac{1}{V(\theta)} \frac{dV(\theta)}{d\theta}}{1 - \frac{1}{V(\theta)} \frac{dV(\theta)}{d\theta} \theta} \right]. \quad (5.12)$$

According to equation 5.12, the equality $\psi=\theta$ occurs only when $dV(\theta)/d\theta=0$, that is, at the extrema of $V(\theta)$. At those extrema the ray direction coincides with the wavefront normal's direction and the group-and phase velocity surfaces touch each other as shown in Figure 5.3.

Previously, the group velocity has been obtained in terms of the phase velocity. Further, to understand the phenomena of triplication it is worthwhile to understand the group velocity surface, phase velocity surface and slowness surface.

- **Group velocity surface:** A surface which is produced by plotting the group velocities from a common origin along the ray direction.
- **Phase velocity surface:** Plotting the phase velocity as a function of its direction form the phase velocity surface.
- **Slowness surface:** The reciprocal surface of phase velocity surface is the slowness surface whose radius in any direction is proportional to 1/phase-velocity.

So far it has been shown that the group velocity can be obtained using the phase velocity. To gain more insight into the geometries of the slowness and group velocity surfaces, we

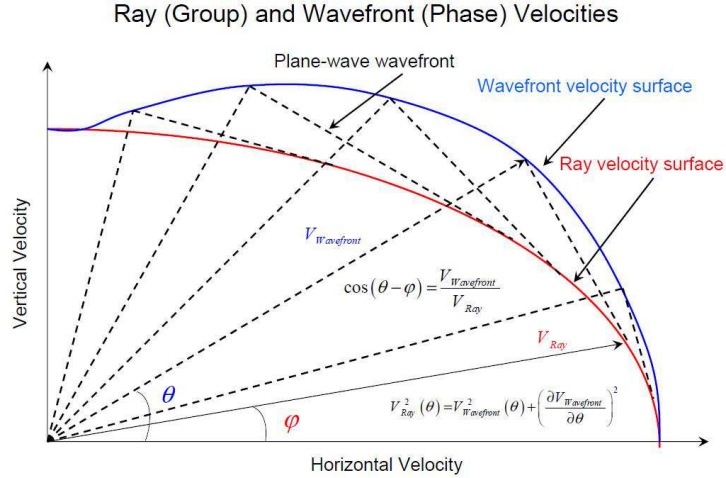


Figure 5.3: Schematic representation of the relationship between phase velocity and group velocity surfaces. The angles ψ and θ are the group and phase angles, respectively and are measured with horizontal axis. It illustrates that the group velocity surface can be constructed from the known phase velocity surface. Plane-wave fronts are the normal drawn from known points of the phase velocity surface to the group velocity surface and governs the energy distribution for a given direction (Nadri, 2009).

can describe the group velocity in terms of slowness as (Grechka, 2009)

$$\mathbf{g} \cdot \frac{\partial \mathbf{p}}{\partial p_i} = 0, (i = 1, 2). \quad (5.13)$$

This equation implies that the group-velocity vector \mathbf{g} is normal to the slowness surface. Now, to explain the origin of triplication, refer to Figure 5.4. In this figure the slowness, phase-velocity and group velocity surfaces of SV-wave are indicated by dashed blue, solid red and solid black, respectively. The slowness in this figure has both convex and concave regions. As we know from equation 5.13, the normal to the slowness surface indicates a ray direction. We plot normals to the slowness surfaces which are shown in Figure 5.4 by light and dark blue arrows. The normals spread away from each other (light blue) when the slowness surface is convex and due to this the wavefront remains single-valued. Conversely, the wavefront becomes multivalued when the normals are drawn to the concave portion of the slowness surfaces because in this case the normals intersect each other and cause the group-velocity surface to fold onto itself. A close inspection of

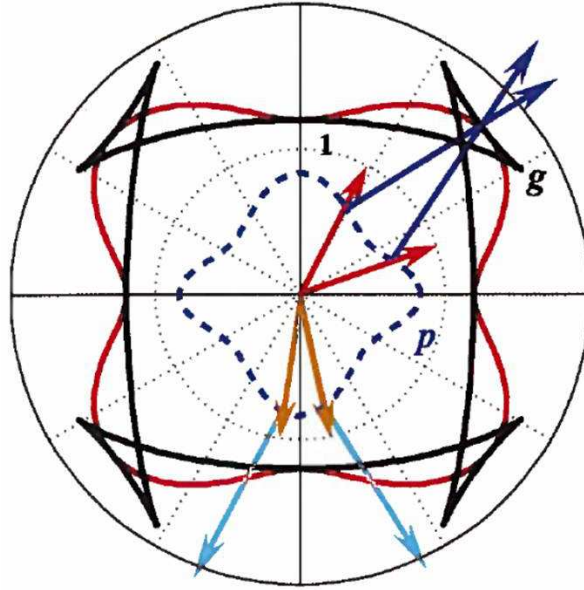


Figure 5.4: Schematic representation of the relationship between phase-velocity (solid red) and group-velocity (solid black) surfaces and slowness surface (dashed blue). This figure makes it possible to understand the reason for triplication on the SV wavefront (Grechka, 2009). The normals to the slowness-surface are shown by light and dark blue arrows. Red and brown arrows indicate the wavefront normals.

Figure 5.4 makes it possible to conclude that if we draw a radius vector for a particular direction it will intersect the group velocity surface three times. As the radius vector corresponds to the magnitude of group velocity, the three arrivals corresponding to the three ray velocities results in triplication.

So far I have discussed the crucial factors which can be used in order to analyze the dynamic behavior of the body wave propagation, through the anisotropic media. Travel times in anisotropic media are accommodated through the plane wave transformation and phase shift. For accomplishing phase shift modelling, I have implemented the same theory as discussed in Chapter 3 and CREWES report (Sharma and Ferguson, 2009a). The only difference is that a layer of infinitesimal thickness above the HTI medium is taken into account here in order to define the wavefield propagation direction initially. I have implemented a constraint on this layer that the velocity possessed by it is the maximum velocity of the lower HTI media. The incident wavefield propagation direction

is governed by the cross product of the unit vector normal to the plane wavefront with unit vector in the direction of axis of symmetry as

$$p_I = |\hat{\mathbf{p}} \times \hat{\mathbf{a}}| / \sqrt{p_1^2 + p_2^2 + q^2}, \quad (5.14)$$

where p_1 , p_2 and q are the horizontal components 1, 2 and the vertical component of the slowness vector, respectively and these are evaluated in the incident medium. For HTI media presently, I take the interface characterized by $(\hat{\mathbf{a}}=\hat{\mathbf{j}})$. Once the effective ray parameter p_I is computed, the vertical slowness q_{HTI} of the incident body wave in the lower HTI media can be computed in terms of Thomsen's parameters and the effective ray parameter known for all the body waves (Sharma and Ferguson, 2009a). On being acquainted with the effective ray parameter and the vertical slowness of the incident wavefield in the HTI media, the unit vector normal to the plane wavefront in the propagation direction can be determined as

$$\hat{\mathbf{p}}_{HTI} = \frac{p_1 \hat{\mathbf{i}} + p_2 \hat{\mathbf{j}} + q_{HTI} \hat{\mathbf{k}}}{\sqrt{p_1^2 + p_2^2 + q_{HTI}^2}}, \quad (5.15)$$

Now, the cross product of this unit vector with the vertical axis of a $3C$ geophone

$$|\hat{\mathbf{p}}_{HTI} \times \hat{\mathbf{a}}| / \quad (5.16)$$

yields the polarization angle at each $3C$ geophone located at the interface and nurture to the rotation matrix as the knowledge of the polarization angle is the essential parameter for obtaining the rotation matrix. Once the rotation matrix is built, it is implemented on the extrapolated wavefield in order to model $9C$ - $3D$ data.

5.3 Example

I consider a homogeneous and anisotropic HTI medium of 700 m thickness for a simple demonstration. The fact that the ratio of fracture size to the seismic wavelength less than

1 makes the medium to be effectively homogeneous and anisotropic. Further, Thomsen's parameters are considered from Vernik's paper (Vernik and Liu, 1997) for the medium characterization. Now a known impulsive source is extrapolated through the medium in the plane wave domain and transformed back into the space and time domain at the interface. Prior to energy distribution among the three components of the $3C$ geophones, I consider the in-line, cross-line and time slices of the known extrapolated wavefield in order to analyze the kinematic and dynamic behavior of the body waves in HTI media. Presently, the in-line and cross-line directions are characterized by the fracture strike direction and normal to it, respectively. Consequently, first a known P wave source is considered at the earth surface and is extrapolated through the HTI medium. Figure 5.5a shows the in-line slice of the extrapolated wavefield and the cross-line slice is shown in the Figure 5.5b. Kinematically, these slices lead to the following observations

- The arrival time of the extrapolated wavefield at zero offset is the same in the in-line slice as well as in the cross-line slice.
- The travel time response of the in-line slice is hyperbolic while it is non-hyperbolic for the cross-line slice.
- The arrival time of the extrapolated wavefield at far offsets in the in-line slice is less than registered in the cross-line slice. It is a manifestation of the well known fact that P-waves travel fastest in the direction of fracture strike and slow in the direction normal to it.

Figure 5.6a and b show the time slices of the extrapolated wavefield without and with analytic curve. The obtained ellipse in the $x-y$ plane manifests the azimuthal anisotropy of the medium as expected. The overlapping of the analytic ellipse with the obtained one ensures the accuracy of the proposed phase shift modelling kinematically.

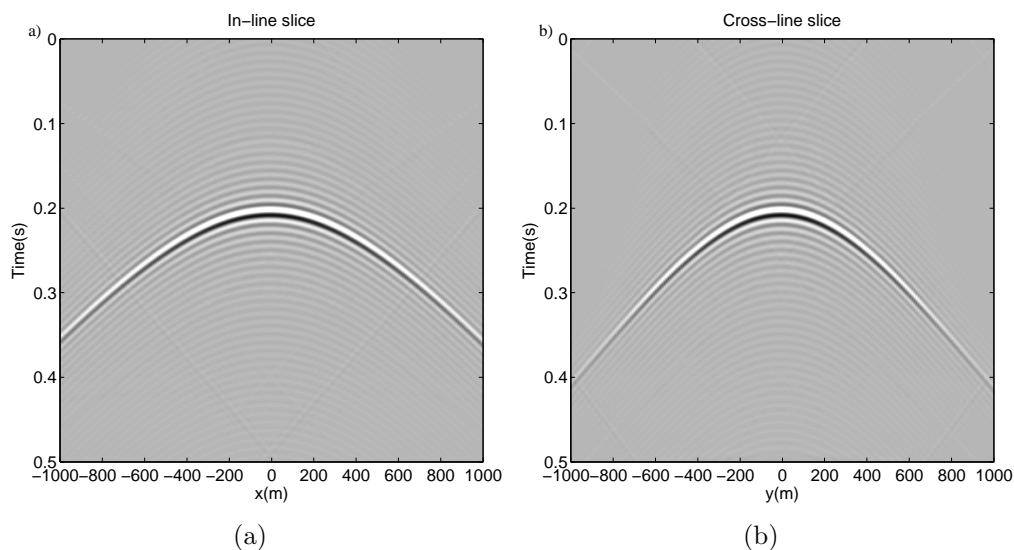


Figure 5.5: (a) In-line (b) Cross-line slice of extrapolated P wavefield through an anisotropic medium characterized by Thomsen's parameters shown in appendix. The considerable difference between these slices is observed kinematically as well as dynamically. Both slices manifest well known fact that P-wave travel fast in direction of strike with high amplitude.

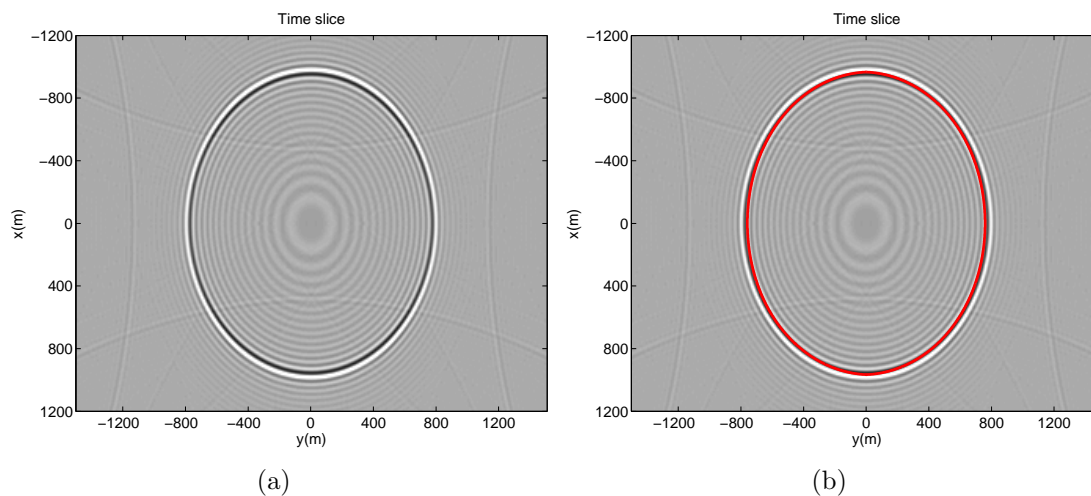


Figure 5.6: Time slice of extrapolated P wavefield (a) without (b) with analytic curve. Obtained ellipse is a manifestation of azimuthal anisotropy as expected. More energy is observed in fast direction. The overlapping of the analytic curve (shown in red color) with the obtained ellipse illustrate authentication of proposed phase shift modelling.

Dynamically, it is noticed that P-wave amplitude increases from the slow direction to the fast direction. This observation correlates well with equation 5.8 and Figure 5.3 where it is mentioned that the ray deviates towards the high phase velocity direction from the low velocity direction in the presence of anisotropy. In addition to this, if we draw a normal from a known point of the phase velocity surface to the group velocity surface, the point where it makes a contact with the group velocity surface corresponds to the plane wave drawn tangentially at that point. Then the energy distribution depends on how close these points are at the group velocity surface and it can be observed from Figure 5.3 that these points are dense in and near the fast velocity direction while sparse in the low velocity direction and hence the observed amplitude pattern in our analysis. Now, in order to seek the influence of the anisotropy on the kinematic and dynamic behavior of the P-wave I am repeating the same procedure as outlined above after introducing the different anisotropy in the same model as taken previously. Figure 5.7a and b show the in-line and the cross-line slices of the extrapolated wavefield for the same medium as before but for a positive value of δ . The time slices of the extrapolated wavefield with and without the analytic curve are shown in Figure 5.8a and b. In continuation of this analysis, the in-line and the cross line slices for negative δ are shown in the Figure 5.9a and b and the time slices are shown in the Figure 5.10a and b. A close examination of these figures make it possible to illustrate the following observations:

- Kinematically, the different values of δ do not have any effect on the in-line slice's response while do have the noticeable effect on that of the cross-line slice. The authentication of the proposed phase shift modelling is shown in these figures as analytic ellipse coincides with the obtained ellipse.
- Dynamically, at a given time the energy distribution in the $x - y$ plane depends on the magnitude of the anisotropic parameter δ . Further, it's noticed that for

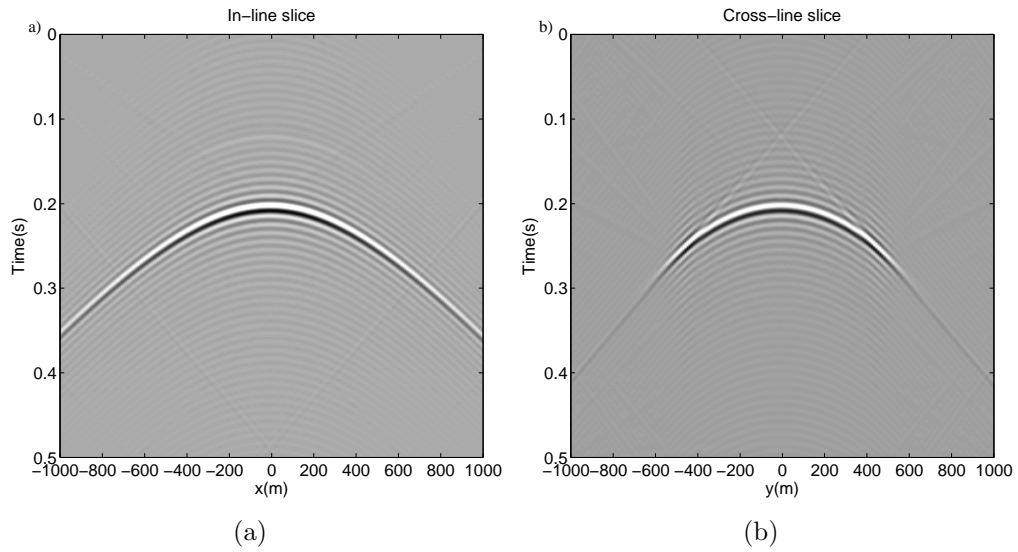


Figure 5.7: (a) In-line (b) Cross-line slice of extrapolated P wavefield for same model as before but for a larger magnitude of anisotropy (higher $\delta=0.29$) in the medium. The large value of δ does have effect on the cross-line while the in-line slice is not influenced.

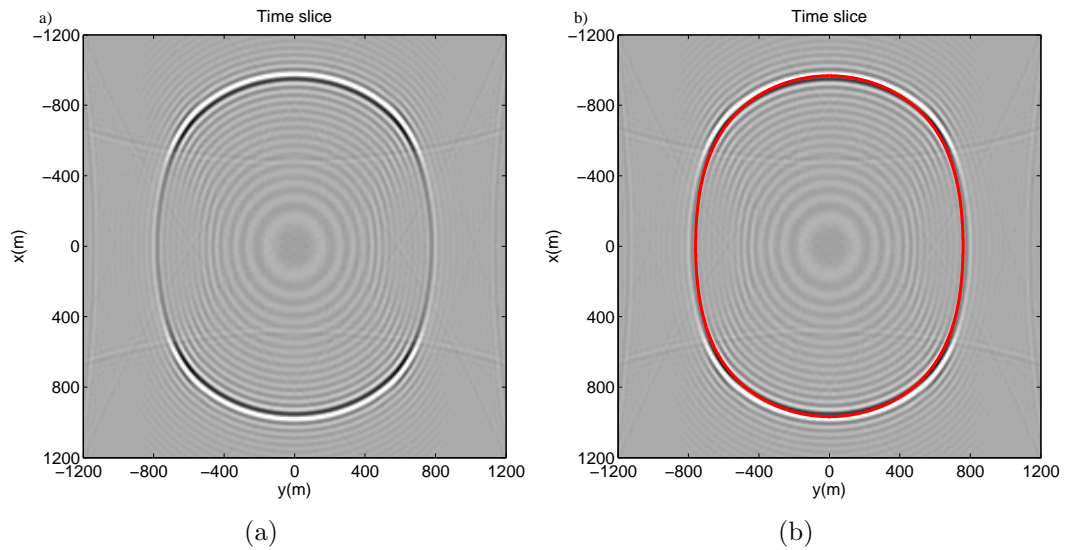


Figure 5.8: Time slice of the extrapolated P wavefield (a) without (b) with analytic curve. The large value of δ does have influence on the kinematic and dynamic behaviors of P wave.

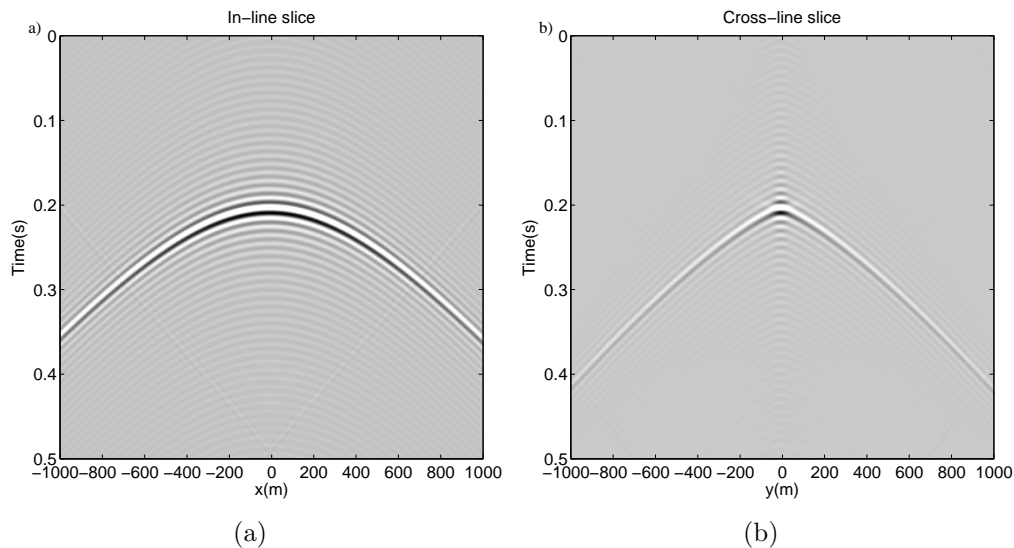


Figure 5.9: (a) In-line (b) Cross-line slice of the extrapolated P wavefield for the same model as considered for above Figure but for large negative value of δ ($\delta=-0.2$). A considerable effect, kinematically as well as dynamically, of anisotropy is observed on the cross-line slice.

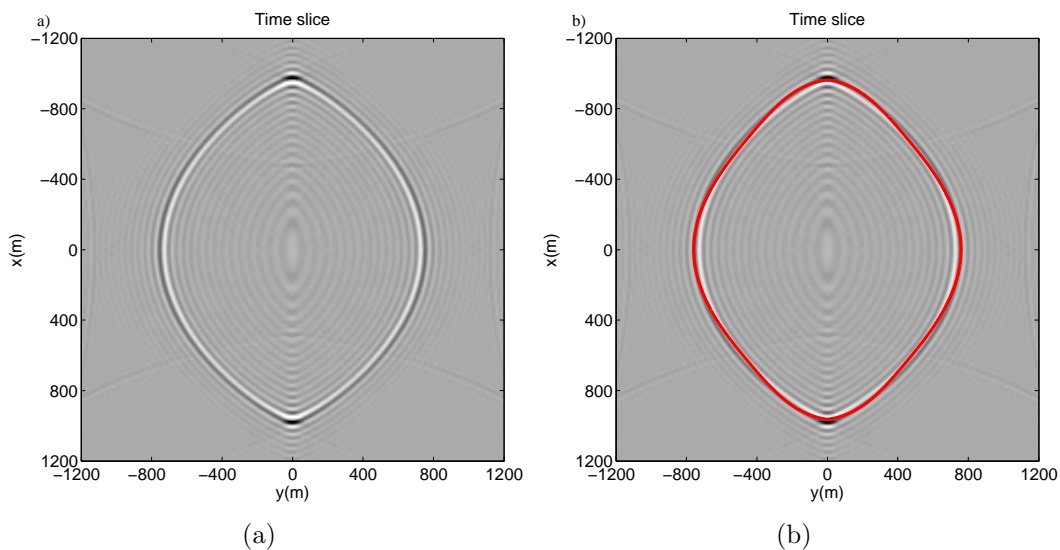


Figure 5.10: Time slice of the extrapolated P wavefield (a) without (b) with analytic curve for the same medium as considered in Figure 5.9. The authentication of the proposed modelling is demonstrated here as analytic curve is analogous to the obtained one.

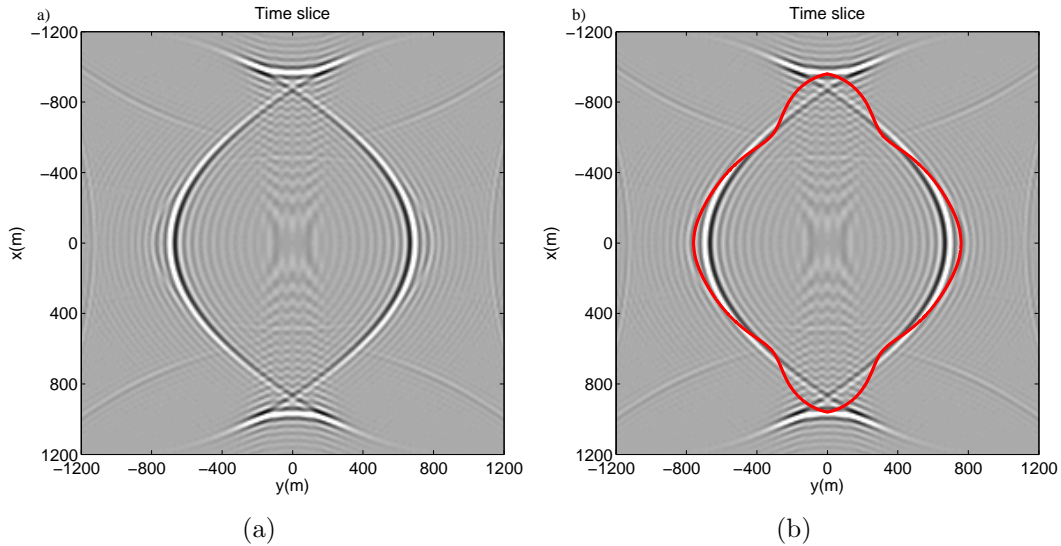


Figure 5.11: Time slices of the extrapolated P wavefield (a) with (b) without analytic curve through the medium characterized by Thomsen's parameters chosen randomly. The unexpected behavior, kinematically and dynamically, illustrate that choice of Thomsen's parameters for a medium characterization can not be random.

negative δ the contrast in the in-line and cross-line's energy is more than that for the positive δ .

Moreover, the choice of δ for the figures shown above was limited on behalf of the relationship between elastic stiffness constants and Thomsen's parameters as shown in the appendix D. Thus, the adopted value of δ should make physical sense and can not be taken randomly and it can be verified in reference to Figure 5.11 . Figure 5.11a and b show the time slice of the extrapolated wavefield for the delta chosen randomly. It is observed here that the maximum amplitude of the P-wave occurs in the slow direction and decreases towards the fast direction and there is no overlapping of the analytic and the obtained ellipses. Thus, the demonstrated dynamic behavior of the propagated P-wave is just opposite of what we expected and make it necessary that the selection of δ can not be random. Figure 5.12a and b show in-line and cross-line slices of extrapolated SH-wave

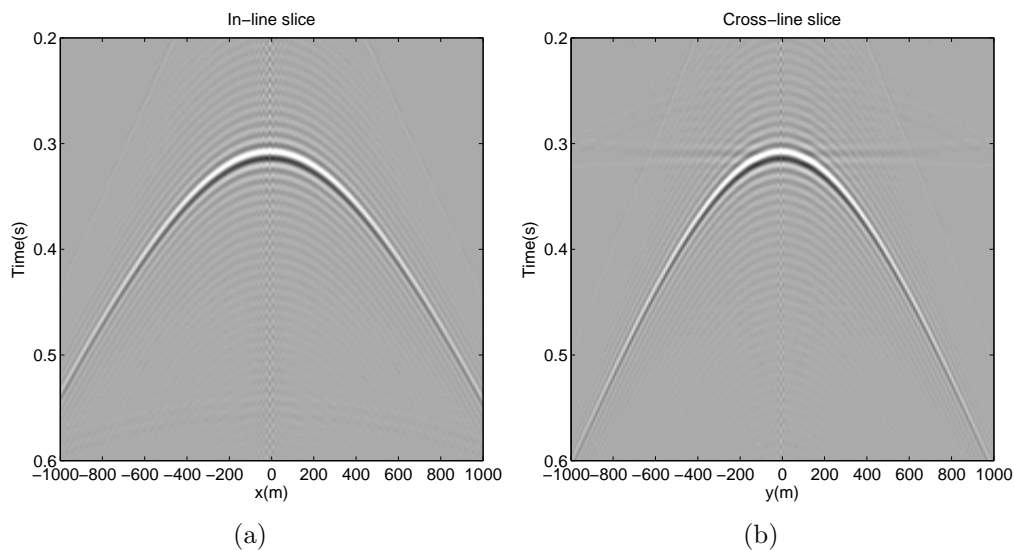


Figure 5.12: (a) In-line (b) Cross-line slice of extrapolated SH wavefield for same model as considered in Figure 5.5 with low resolution. The difference, kinematically or dynamically, can not be examined precisely on behalf of these slices.

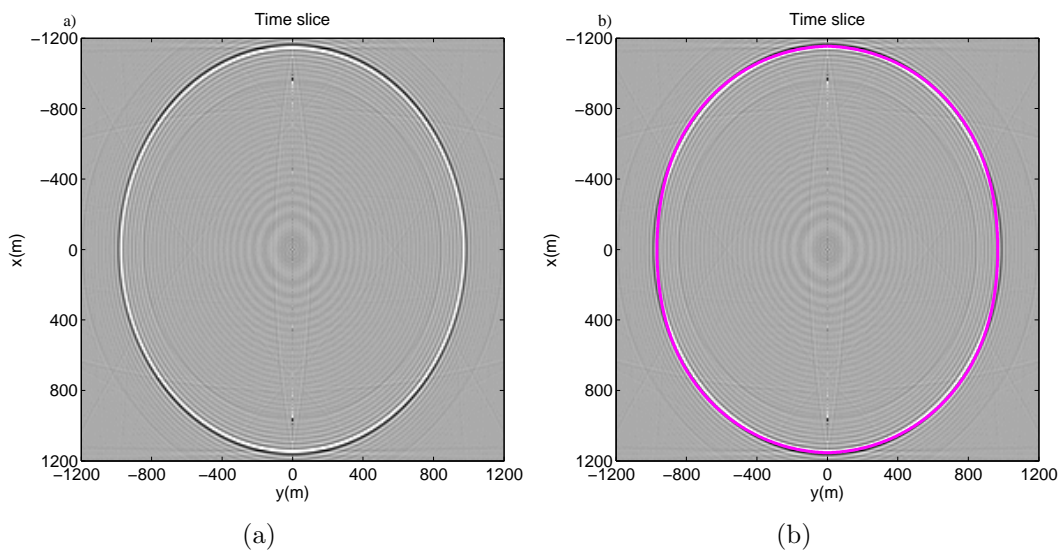


Figure 5.13: Time slice of the extrapolated SH wavefield (a) without (b) with analytic curve for same medium as ones shown in Figure 5.12 and demonstrate that SH wave travel fast in direction of fracture strike with high amplitude and illustrate the authentication of the proposed modelling.

through the same model as considered in Figure 5.5. Both of these slices are plotted with a high clipped display, otherwise, the difference in between these slices in terms of amplitude and travel time would not be noticeable. Although, it is observed from Figure 5.13a that SH-wave travel fast in the direction of fracture strike and energy decreases from the fast direction to the slow direction and follow the same behavior as that of P-waves. Kinematically, the authentication of the proposed modelling for SH-wave in anisotropic medium is demonstrated as the analytic curve (shown in magenta color) matches with the obtained one in Figure 5.13b. Again, to observe the influence of anisotropy on the kinematic and dynamic behaviors of SH-wave, the same model as considered for Figure 5.12, is taken into account after introducing large anisotropy (higher γ) into the medium through which SH-wave propagates ($\gamma = 0.34$). The in-line and the cross-line slices are shown in Figure 5.14a and b. The dissimilarity between these two slices is observed here in terms of travel time and amplitude. However, these analysis can be emphasized in reference to Figure 5.15a where it is demonstrated that more energy travel in the fast direction. As this Figure differs from Figure 5.13a it is possible to make a conclusion that anisotropy does have an effect on kinematic and dynamic behaviors of the SH-wave. So far, I have discussed the effect of anisotropy on wavefield propagation of seismic waves. Now following the same theory as outlined above through equation 5.14 to 5.16 I have obtained $\mathcal{3C}$ data for known P-wave source at the surface after applying the rotation matrix on the extrapolated wavefield and have taken a slice through the in-line direction shown in Figure 5.16. The red dashed line highlighted in the circle at the top right corner of Figure 5.16c indicates the direction along which a vertical slice of the modelled data is taken. The in-line and cross-line direction are indicated by blue and magenta color, respectively. Figure 5.16a, b and c show the registered energy versus offset (REVO) analysis of P wave on H_1 , H_2 and V components while registered energy versus azimuth (REVA) analysis is shown in Figure 5.17a, b and c, respectively. Moreover, these figures

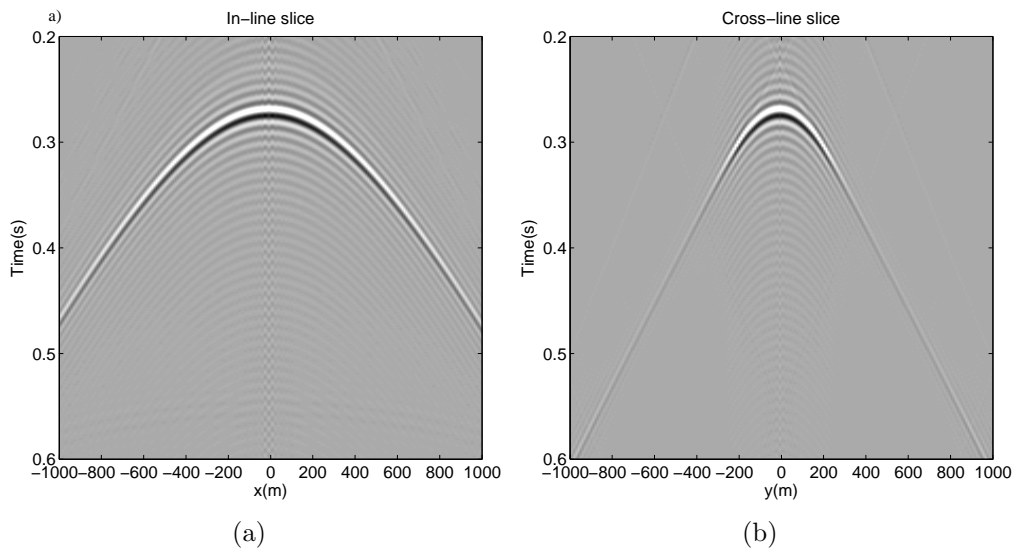


Figure 5.14: (a) In-line (b) Cross-line slice of the extrapolated SH wavefield for the same model as considered above but of large anisotropy ($\gamma = 0.34$) and show the effect of anisotropy on propagation of the SH wavefield.

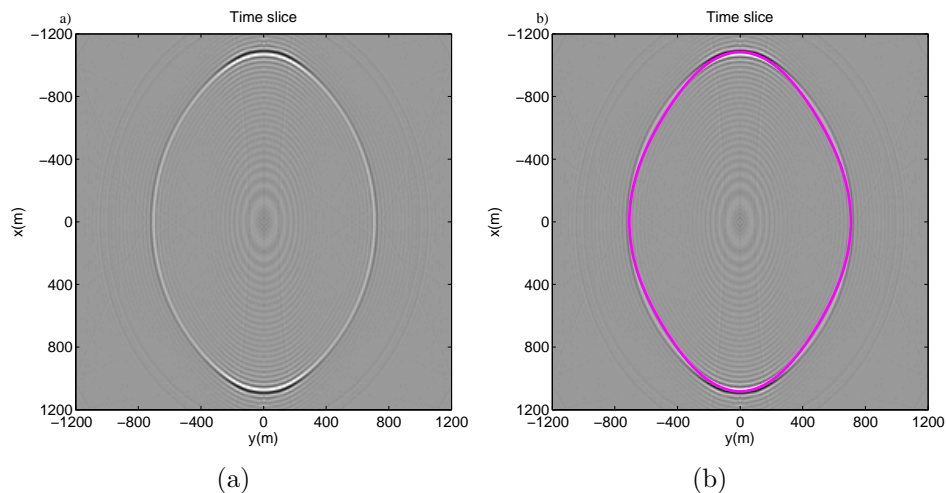


Figure 5.15: Time slices of the extrapolated SH wavefield through the same model as ones shown in Figure 5.14. The authentication of the proposed modelling is shown in (a) and (b) kinematically and dynamically, respectively.

follow the expected pattern of registered energy on the different components with offset and azimuth.

5.3.1 SV-case

Now the same theory as discussed above has been implemented for SV-wave. In order to analyze the kinematic and dynamic behavior of the SV-wave in HTI media, the same model as used for P and SH-wave is considered. Figure 5.18a and b show the in-line and cross-line slices of the extrapolated SV wavefield. It is observed that both of these slices are very close to each other in terms of the travel time response. Figure 5.19a and b illustrate time slices of the extrapolated wavefield. The obtained circle indicates that anisotropy does not have a considerable effect on SV-wave propagation as had on P and SH-wave propagations for this case. Further, the effect of anisotropy on the SV-wave propagation has been examined on behalf of considered models shown in the appendix.

Figure 5.20a and b show the time slices of the SV wavefield extrapolated through a medium characterized by Thomsen's parameters shown in the appendix and possesses positive ϵ and δ with the condition ($\epsilon > \delta$). In continuation of this, another model possesses the same condition as outlined previously but with large magnitudes of Thomsen's parameters taken into account for observing the effect of anisotropy. By inspecting Figures 5.20 and 5.21, it can be revealed that as long as Thomsen's parameters follow the condition ($\epsilon > \delta$) anisotropy does not have a considerable effect on SV wave propagation either kinematically or dynamically. However, the effect of anisotropy on SV wave propagation can be seen in Figures 5.22, 5.23 and 5.24. Although, the authentication of the proposed modelling, kinematically, is not demonstrated in these cases as obtained results are not matching with analytic curves, it is possible to make some remarkable conclusion as follows

- If ($\epsilon - \delta < 0$), the cusps occur in the in-line direction and can be observed in Figure

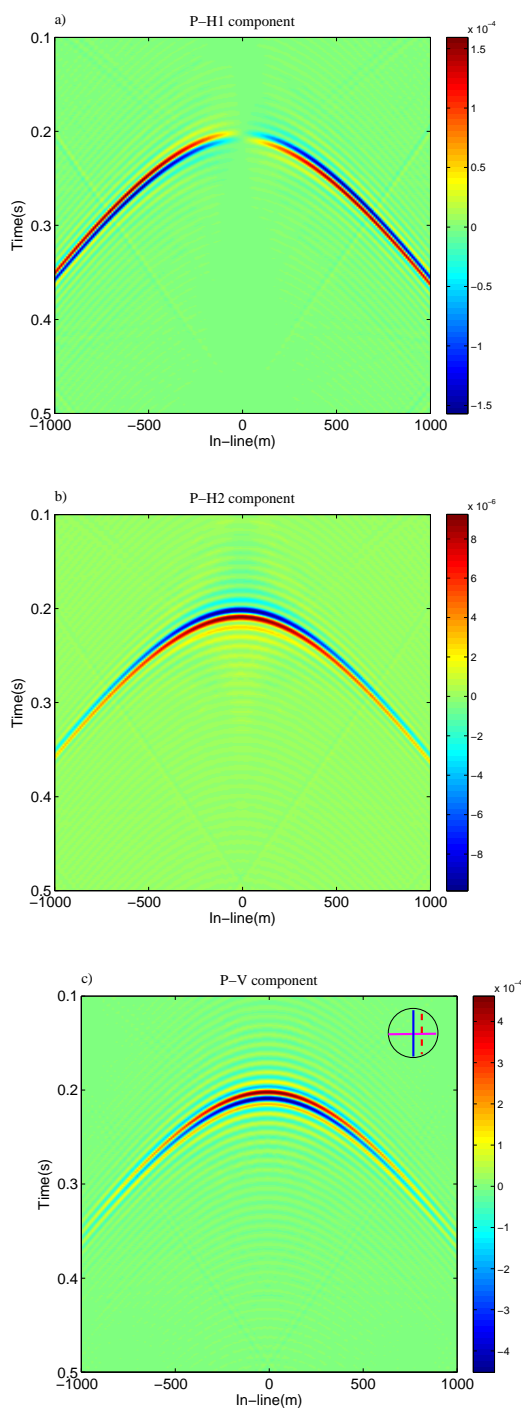


Figure 5.16: (a) Registered energy versus offset (REVO) analysis of P-wave on H1 component illustrate that H1 component is more favorable for energy registration as offset increases. Polarity reversal appear on the either side of zero offset. (b) (REVO) analysis of P-wave on H2 component illustrate that H2 component is more favorable for energy registration near to zero offset. Polarity remains stationary on the either side of zero offset. (c) Recorded P-wave energy on vertical component demonstrate that energy registration on vertical component decreases with offset. Polarity follow the stationary behavior on either side of zero offset.

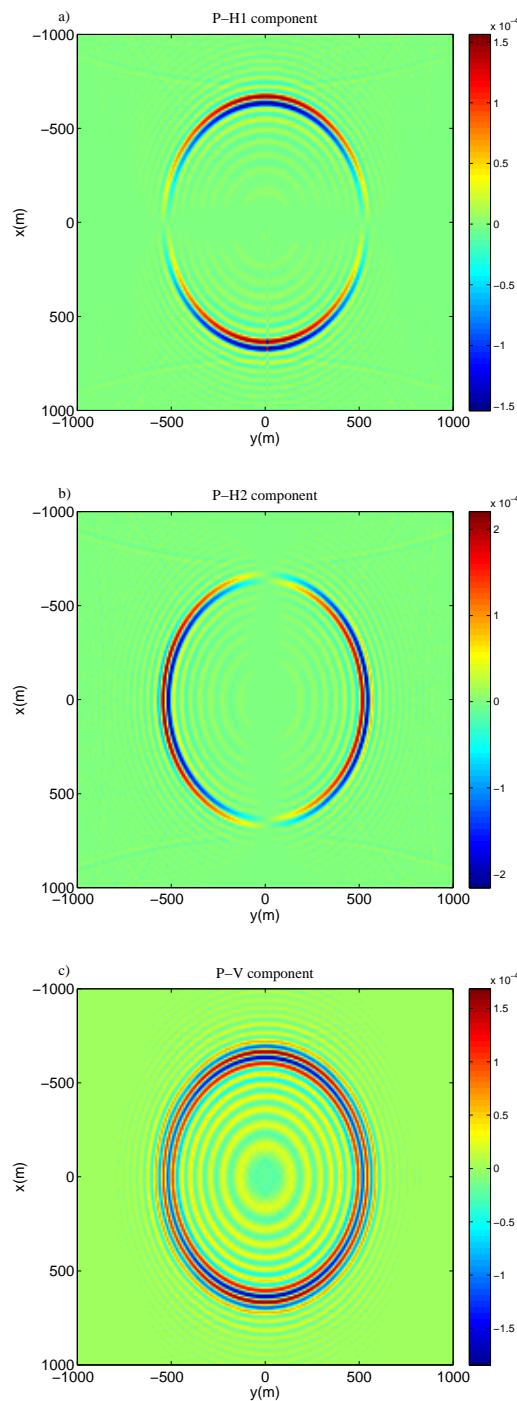


Figure 5.17: (a) Registered energy versus azimuth(REVA) analysis of P-wave at H1 component indicates that energy registration increases as azimuth increases from 0 to 90. Polarity reversal occur on the either side of a line that bisects the circle along cross-line direction. (b) REVA analysis of P-wave at H2 component indicates that energy registration decreases as azimuth increases from 0 to 90. Polarity reversal occur on the either side of a line that bisects the circle along in-line direction. (c) REVA analysis of P wave on vertical component reveal the variation of recorded energy and polarity with azimuth.

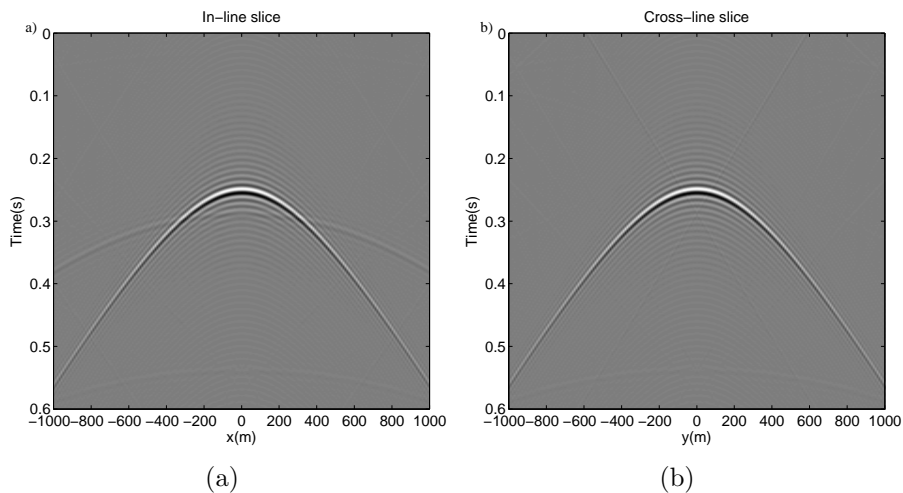


Figure 5.18: (a) In-line (b) Cross-line slice of the extrapolated SV wavefield for the same model as considered above for P and SH waves. The in-line slice is analogous to the cross-line slice

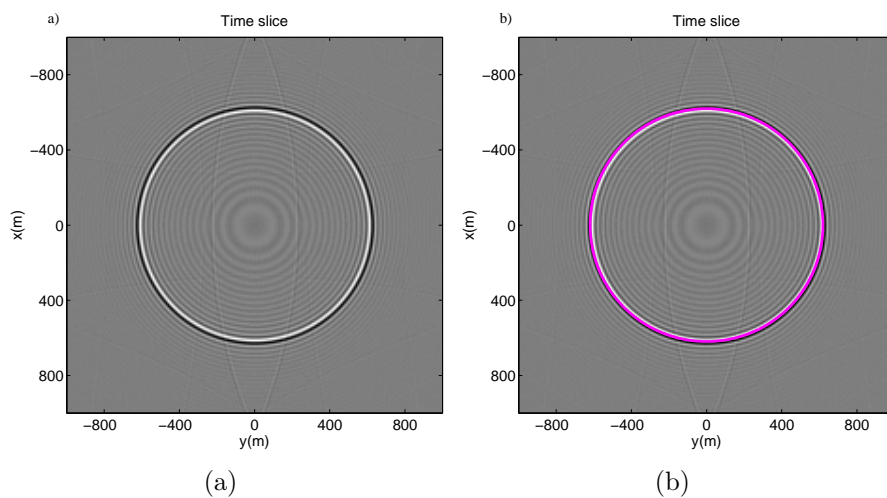


Figure 5.19: Time slices of the extrapolated SV wavefield through the same model as ones shown in Figure 5.18. The authentication of the proposed modelling is shown in (a) and (b) dynamically and kinematically, respectively. The obtained circle illustrate that anisotropy does not have a considerable effect on SV wave propagation.

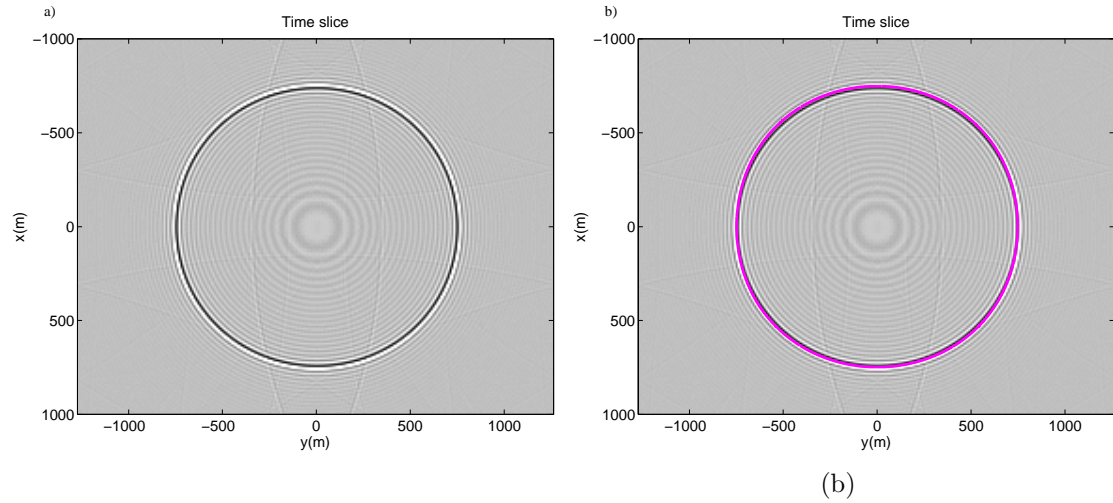


Figure 5.20: Time slices of the extrapolated SV wavefield through model2 ($\epsilon > \delta$) as ones shown in Table D.2. The authentication of the proposed modelling is shown as analytic curve overlays with obtained one as shown in (a) and (b). There is no effect of anisotropy for this model.

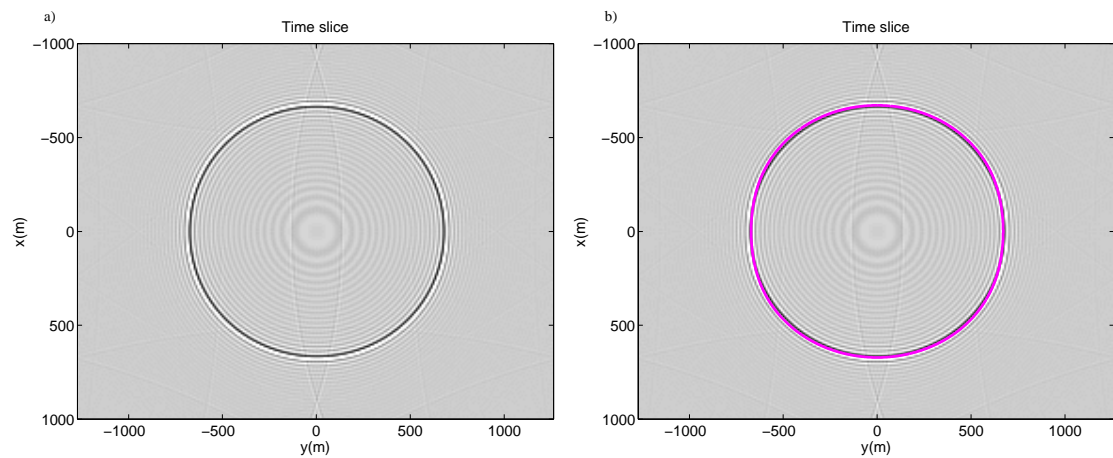


Figure 5.21: Time slices (a) and (b) of the extrapolated SV wavefield through model3 with large magnitude of ($\epsilon > \delta$) shown in Table D.2. The authentication of the proposed modelling is shown in (b), kinematically. Still no effect of anisotropy is observed.

5.22a and be authenticated by Figure 5.22b.

- if δ is negative and $(\epsilon - \delta > 0)$, the cusps occur near 45° from the axis of symmetry.

This phenomena is noticed in Figures 5.23 and 5.24.

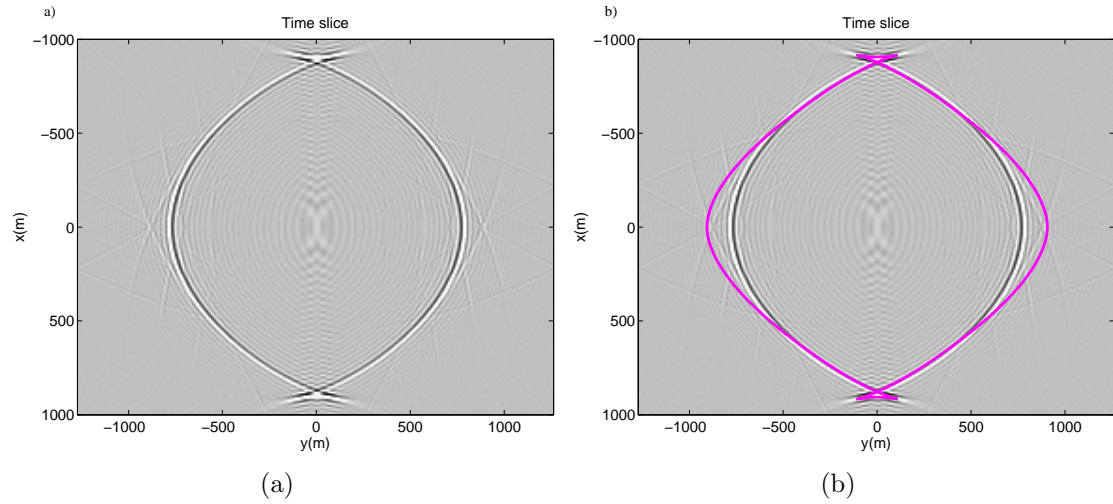


Figure 5.22: Time slices of the extrapolated SV wavefield through the model4 ($\epsilon < \delta$) shown in Table D.2. The cusps phenomena is occurred in the in-line direction. The occurrence of cusps is endorsed by the analytic curve but no overlapping of analytic curve with obtained one is noticed.

5.4 Conclusions

I have presented multi-component modelling of P-wave in the plane wave domain for HTI media. The authentication of the proposed phase shift modelling has been demonstrated kinematically and dynamically. Further, the kinematic and dynamic effect of anisotropy on seismic waves propagation has been demonstrated and the dependency of this analysis on the magnitude of Thomsen's parameters is also illustrated. Since the fractures have an impact on the amplitude and travel time of seismic waves propagation, the careful investigation of this impact can be used for fracture detection.

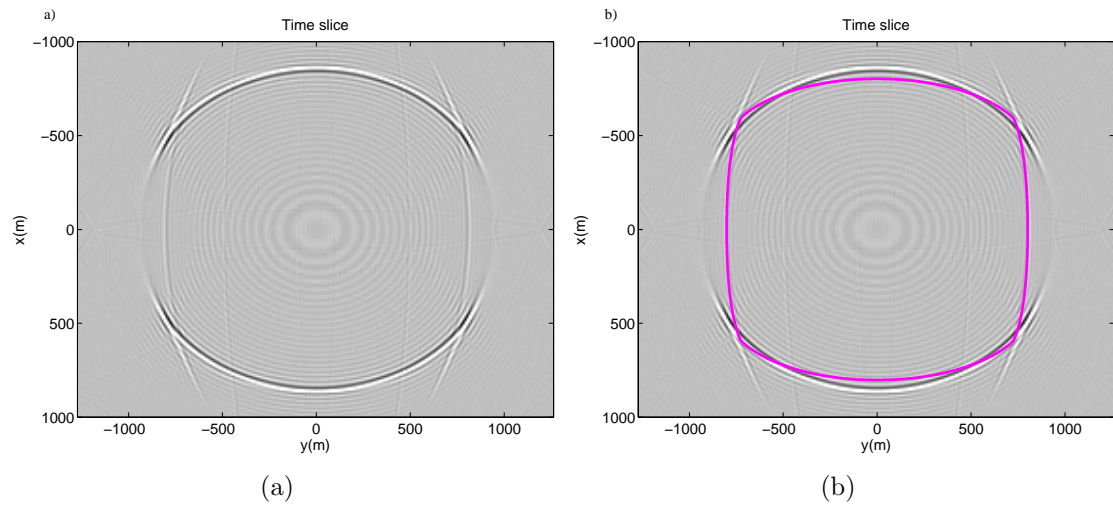


Figure 5.23: Time slices of the extrapolated SV wavefield through model5 ($-\delta$) shown in Table D.2. The cusps is observed near to 45° .

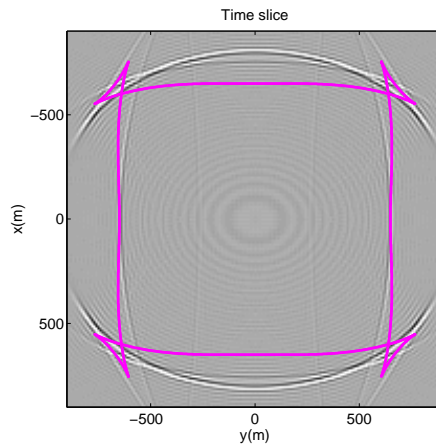


Figure 5.24: Time slices of the extrapolated SV wavefield through the model possesses large negative value of δ (model6) as shown in Table D.2.

Chapter 6

Phase shift modelling with new proposed approaches.

6.1 Summary

In order to perform phase shift modelling for HTI media, I have implemented a constraint on a layer of infinitesimal thickness above the HTI media that its velocity is the maximum velocity of the lower HTI medium. To remove this constraint, I have presented two more approaches here. According to first approach, I use the relationship between the cosine of any angle with the horizontal axis and the angle of incidence considered with respect to vertical and azimuth for obtaining an effective ray parameter for HTI media. Once the effective ray parameter is known, the vertical slowness is computed using this parameter and Thomsen's parameters of equivalent VTI media corresponding to HTI media. The acquaintance of the vertical slowness make it possible to extrapolate known source wavefield through anisotropic media using a phase shift operator. In the second approach, I solve the Christoffel equation for obtaining vertical slowness used to obtain phase shift operator for anisotropic media. In order to test the proposed approaches, I have performed seismic modelling for orthorhombic media, that has been examined in contrast to the physical modelling presented by another student of CREWES. Further, taking into account the second data acquisition geometry for VTI media, multi-component data has been obtained for P-wave source. For the sake of obtaining the multi-component data for HTI media, I have computed P-wave R coefficient numerically. The fidelity of the obtained R coefficient has been illustrated in light of Rüger,s approach.

6.2 Introduction

Historically, it has been demonstrated that the formulas pertinent to VTI media can be used for HTI media (Berryman, 2008). In doing so, the physical meaning of angle of incidence differs from the classically used one. Generally, the angle of incidence is measured with vertical axis (Rüger, 2001) while in case of HTI media it would be considered from the horizontal axis. Moreover, the classical analytic expressions for HTI media are expressed in terms of the angle of incidence that is measured with respect to vertical axis (Rüger, 1998). Thus, dealing with HTI formulas obtained from VTI formulas introduces the problem when obtained results are examined in contrast to the results obtained using the classical expressions. To avoid this problem, I use the relationship between the angle of incidence for VTI and HTI media. The following section describes the whole procedure. Additionally, using this relationship, I remove the constraint posed on the layer of infinitesimal thickness above the HTI media in Chapter 5.

6.3 Theory

6.3.1 First approach

To accomplish the phase shift modelling, the phase shift operator that is based on the vertical slowness is required. Further, the effective ray parameter is a prerequisite for obtaining the vertical slowness. Following simple geometry shown in Figure 6.1, we can build the relationship between the cosine of some angle α with the horizontal axis and the corresponding angle of incidence (θ_I) and azimuth (ϕ) as

$$\cos \alpha = \sin \theta_I \cos \phi, \quad (6.1)$$

As α is the angle with horizontal axis, the ray parameter for HTI media can be described as

$$p_{I_{HTI}} = \frac{\cos \alpha}{v}, \quad (6.2)$$

Now following the theory described in chapter 2, $\sin \theta_I$ can be computed using cross product as

$$\sin \theta_I = |\hat{\mathbf{p}} \times \hat{\mathbf{a}}| / \quad (6.3)$$

where $\hat{\mathbf{p}}$ and $\hat{\mathbf{a}}$ can be calculated using equations 2.1 and (3.22), respectively.

$\cos \phi$ can be computed from the input parameters of plane wave as

$$\cos \phi = \frac{p_1}{\sqrt{p_1^2 + p_2^2}}, \quad (6.4)$$

Using equations (6.4) and (6.3) the equation (6.2) can be expressed as

$$p_{I_{HTI}} = |\hat{\mathbf{p}} \times \hat{\mathbf{a}}| / \frac{p_1}{\sqrt{p_1^2 + p_2^2}} \sqrt{p_1^2 + p_2^2 + q^2}. \quad (6.5)$$

Once the effective ray parameter is known from equation(6.5), the corresponding vertical slowness can be computed using the relationship given by Ferguson and Margrave (shown in Appendix B) and can be used for obtaining phase shift operator (Ferguson and Margrave, 2008). As it is known that there is an equivalent VTI model for HTI media, Thomsen's parameters of the equivalent VTI model are used instead of the generic coefficients for accomplishing the proposed modelling. These parameters can be defined in the following way(Perez, 2010)

$$\epsilon^{(V)} = -\frac{\epsilon}{1 + 2\epsilon}, \delta^{(V)} = \frac{\delta - 2\epsilon(1 + \frac{\epsilon}{f})}{(1 + 2\epsilon)(1 + \frac{2\epsilon}{f})},$$

and

$$\gamma^{(V)} = -\frac{\gamma}{1 + 2\gamma},$$

where

$$f \equiv 1 - \left(\frac{\beta_0}{\alpha_0}\right)^2. \quad (6.6)$$

where α_0 and β_0 have been defined according to equations (4.18) and (4.19), respectively. The importance of these coefficients depends on the fact that all kinematic signature in HTI media now can be described using already known VTI equations.

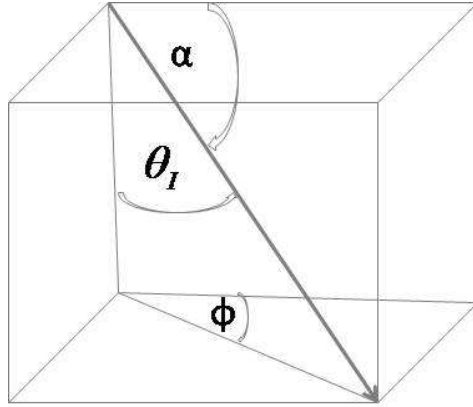


Figure 6.1: Schematic representation of an arbitrary angle α with the horizontal axis, and its associated angle of incidence(θ_I) and azimuth(ϕ)

6.3.2 Second Approach

In second approach, I solve the Christoffel equation for obtaining vertical slowness that is used to obtain phase shift operator for anisotropic media. Generally, Thomsen's parameters defined with respect to vertical, are known as these coefficients have been published before by many authors (Thomsen, 1986b; Vernik and Liu, 1997) and treated as generic coefficients. For accomplishing this approach, first, I have built a relationship in order to obtain elastic stiffness coefficients for given Thomsen's parameters (see Appendix D). Given the elastic stiffness coefficients, I obtain the elastic stiffness matrix for VTI media. Further, using Bond transformation (Upadhyay, 2004) the elastic stiffness matrix for HTI media is obtained. Now the Christoffel equation(3.5) is solved numerically for the vertical slowness(Suleiman, 2007). Once it is known, the phase shift operator is computed for wavefield extrapolation.

6.4 Example

Following the second approach, I extrapolate the known source wavefield through an orthorhombic medium. An orthorhombic medium can be defined by nine elastic constants (Thomsen, 2002). Orthorhombic symmetry, the symmetry of a brick, is most realistic case for many geophysical problems (Thomsen, 2002). Further, an orthorhombic media can be characterized by (1) a thin-bed sequence, or a shale, with a single set of vertical fractures in it; (2) a thin-bed sequence, or a shale, or a massive isotropic sandstone, with orthogonal sets of vertical fractures in it; (3) an isotropic formation with a single set of vertical, non-circular fractures in it (Thomsen, 2002). It possesses three mutually orthogonal planes of mirror symmetry. On consideration the Cartesian coordinate system associated with the symmetry planes, the matrix of density normalized elastic constants in Voigt notation is written as

$$A_{\alpha\beta} = \begin{bmatrix} (A_{11} & A_{12} & A_{13} & 0 & 0 & 0 \\ A_{12} & A_{22} & A_{23} & 0 & 0 & 0 \\ A_{13} & A_{23} & A_{33} & 0 & 0 & 0 \\ 0 & 0 & 0 & A_{44} & 0 & 0 \\ 0 & 0 & 0 & 0 & A_{55} & 0 \\ 0 & 0 & 0 & 0 & 0 & A_{66} \end{bmatrix}. \quad (6.7)$$

where $A_{ij}=c_{ij}/\rho$ and ρ is the density of the given medium.

For this study, the orthorhombic model is considered, which has been used for physical modelling by Mahmoudian (Mahmoudian et al., 2010). The considered model by Mahmoudian represents a natural fractured layer with an area of $5740\text{m} \times 5740\text{m}$ and a thickness of 701m , where the x-z plane is the fracture plane (plane of fast velocities) and the y-axis is the symmetry axis (slow direction). To perform numerical modelling effi-

ciently, I use a natural fractured layer of area $5120\text{m} \times 5120\text{m}$ and a thickness of 701m. Using the elastic constants matrix as shown in equation E.1 (appendix E), I solve the Christoffel equation for vertical slowness. Then the known source wavefield is extrapolated through a given orthorhombic medium. The slices of the extrapolated wavefield are extracted to examine these results in contrast to known slices of the physical modelling. Figure 6.2(a) and 6.2(b) show the in-line slices of the extrapolated wavefield through the orthorhombic media obtained by physical modelling and my proposed numerical modelling (second approach), respectively. The cross-line slices of the extrapolated wavefield obtained by physical modelling and proposed numerical modelling are shown in Figure 6.3(a) and 6.3(b), respectively. As the obtained slices with the proposed modelling are analogous to the slices obtained by physical modelling, the verification of the proposed modelling is demonstrated. Wavefield propagation in the 45° azimuthal plane occurred with physical modelling and with proposed numerical modelling as shown in Figure 6.4(a) and 6.5(b), respectively. Wavefield propagation in the -45° azimuthal plane is shown in Figure 6.5. The match between these slices verify the proposed modelling, kinematically.

Further, in light of the second approach, the first approach is verified since the in-line and cross-line slices obtained by the second approach match with the in-line and cross-line slices obtained by following the first approach. These slices are shown in Figure 6.6(a), 6.6(b) and 6.7(a) 6.7(b).

6.5 Surface seismic data

This section summarizes the method for obtaining multi-component data at the surface using known source wavefield on consideration the surface data acquisition geometry. For accomplishing this, I extrapolate the source wavefield from the surface to the reflector using a phase shift operator, multiply with a reflection coefficient and extrapolate back to

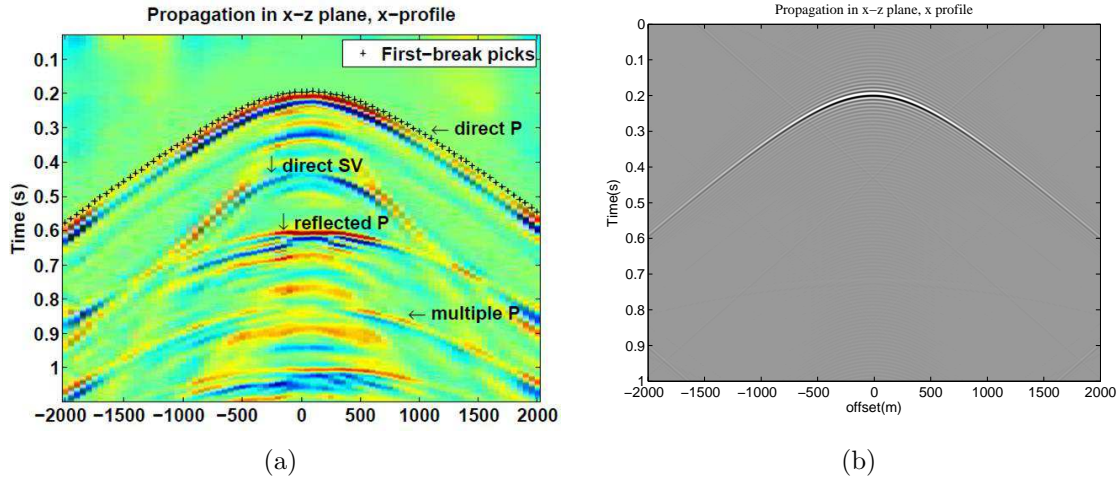


Figure 6.2: In-line slice of the extrapolated wavefield (a) obtained by physical modelling. (b) obtained by proposed numerical modelling(second approach). The analogy of these slices authenticate the proposed modelling kinematically.

the surface. Following this procedure, Figure 6.8(a) shows the monochromatic extrapolated wavefield at the reflector as a function of the horizontal components of the slowness. Figure 6.8(b) illustrates the monochromatic R coefficient in the plane wave domain at the interface of two VTI media shown in Appendix D. The multiplication of these two results in the reflected wavefield. Once the reflected wavefield is obtained in the plane wave domain, it is transformed back into the space and time domain at the surface and is extracted for analysis. The cross-line and in-line slices of the reflected wavefield at the surface before applying rotation matrix on it are shown in Figure 6.9(a) and 6.9(b). It is demonstrated presently that the cross-line slice is analogous to the in-line slice which is the manifestation of the fact that considered media is VTI media, as expected. It is also illustrated that the recorded energy decreases with offset as expected. Further, in order to obtain the multi-component data, I build a rotation matrix based on the azimuth and dip between the grid point and the polarization vector of P-wave source. Now the implementation of this matrix on the reflected wavefield gives the multi-component data.

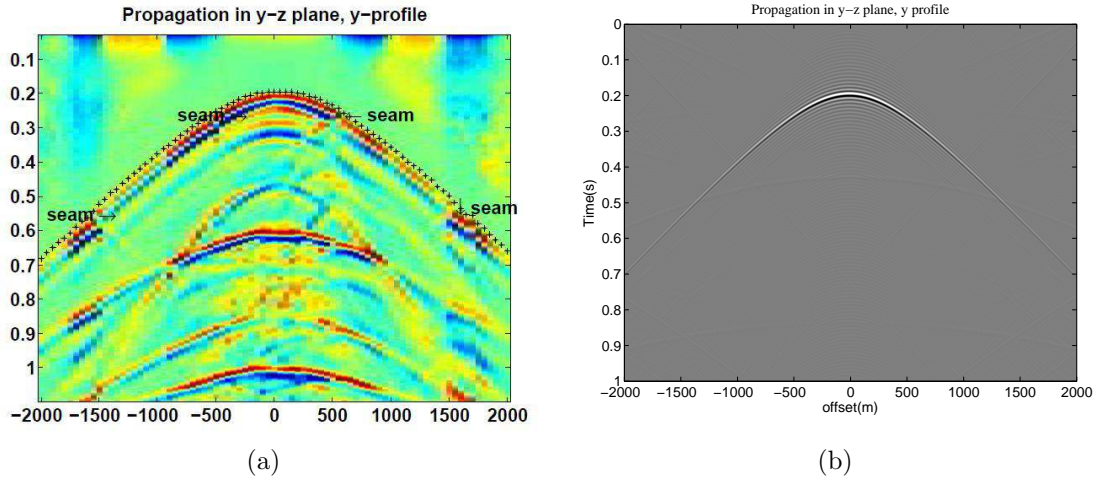


Figure 6.3: Cross-line slice of the extrapolated wavefield (a) obtained by physical modelling. (b) obtained by proposed numerical modelling(second approach). The analogy of these slices authenticate the proposed modelling, kinematically.

Figure 6.10(a) demonstrates the registered P-wave energy on the H_1 component of $3C$ geophones laid on the surface. The registered P-wave energy on the H_2 component and the vertical component is shown in Figure 6.10(b) and 6.10(c). The interpretation of these sub-figures can be described in light of the analysis that has been done in Chapter 3 for Figure 3.4

6.5.1 HTI media

For obtaining the multi-component data at the surface of HTI media, the R coefficient is required. Solving the Christoffel equation, I obtain the polarization vector that is used to calculate the displacement vector numerically. Additionally, the displacement vector is used to compute stress vector. The continuity of the displacement and stress at the interface yields the reflection coefficient(Jilek, 2002). Figure 6.11 demonstrates the P-wave R coefficient at the interface of two HTI media (shown in Appendix E). The R coefficient corresponding to the symmetry axis plane obtained numerically and by Ruger's

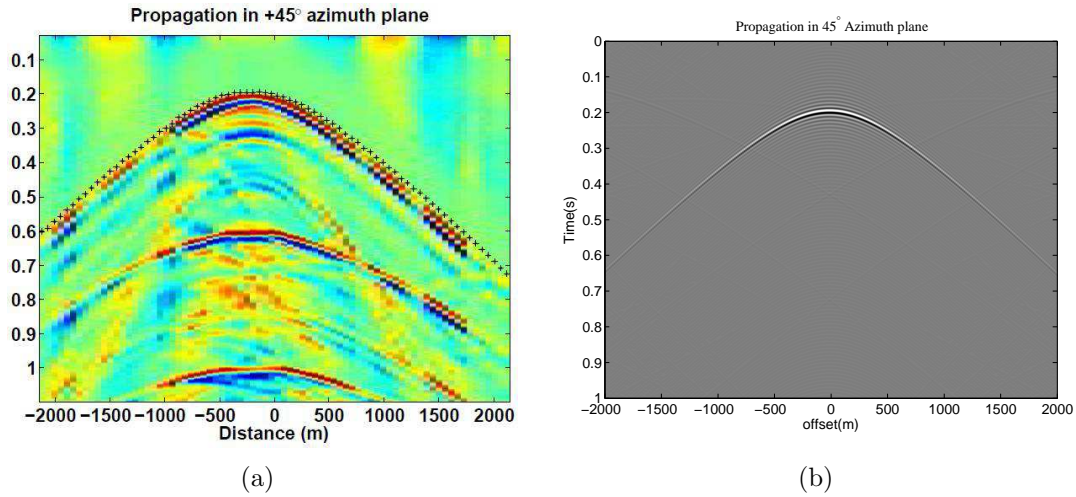


Figure 6.4: Data slice of the extrapolated wavefield along 45° azimuthal plane (a) obtained by physical modelling. (b) obtained by proposed numerical modelling(second approach). The analogy of these slices authenticate the proposed modelling, kinematically.

approach(Rüger, 1998) is illustrated in this Figure by black and green colors, respectively. The analogy of these two curves at the zero slowness and near to it ensures the authentication of the numerical approach of computing the R coefficient. Further, the R coefficient, along with the direction normal to the symmetry axis, obtained numerically and by following Rüger's approach is illustrated by the blue and red colors. The overlapping of both curves at and near to the zero slowness verifies the numerical approach of obtaining the R coefficient. However, it is required to obtain the R coefficient for obtaining multi-component data on consideration the surface geometry of data acquisition. We can use numerically computed R coefficient for accomplishing multi-component seismic modelling for HTI media.

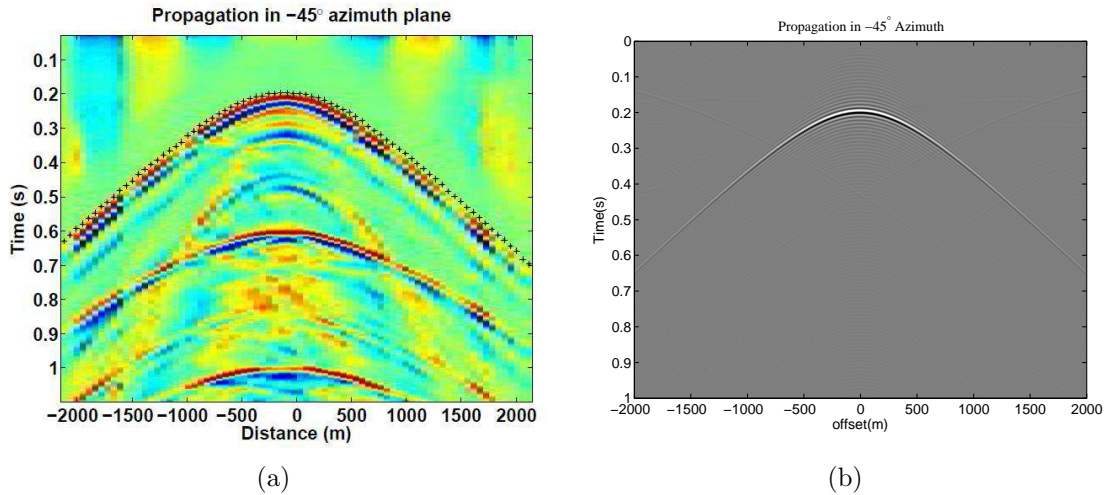


Figure 6.5: Data slice of the extrapolated wavefield along -45° azimuthal plane (a) obtained by physical modelling. (b) obtained by proposed numerical modelling(second approach). The analogy of these slices authenticate the proposed modelling, kinematically.

6.6 Conclusions

I have demonstrated two approaches for the sake of avoiding the problems associated with proposed modelling in the previous chapter for HTI media. The authentication of these approaches has been illustrated by juxtaposing the obtained results from the proposed approaches and physical modelling executed by another student of CREWES. Further, the multi-component surface data has been obtained for known P-wave source for VTI media. In regarding HTI media, I have obtained the P-wave R coefficient. The accuracy of the numerically obtained R coefficient has been tested in consideration of Rüger's approach.

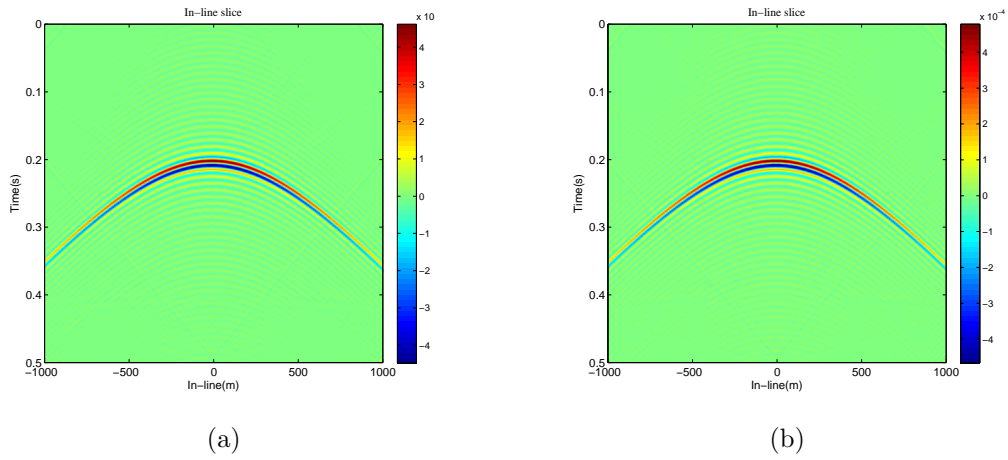


Figure 6.6: The juxtaposition of the in-line slices of the extrapolated wavefield obtained by (a) second approach (b) first approach manifests the analogy of these slice and endorse to the first approach in light of the second approach.

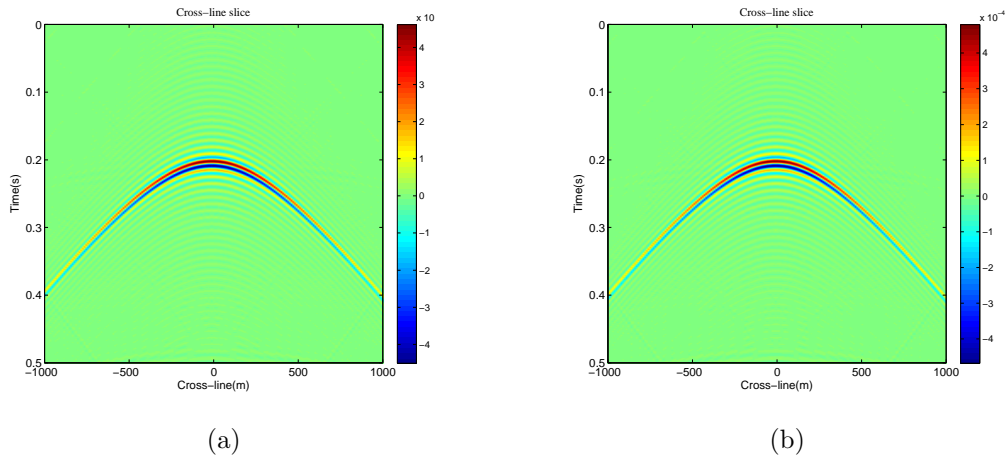
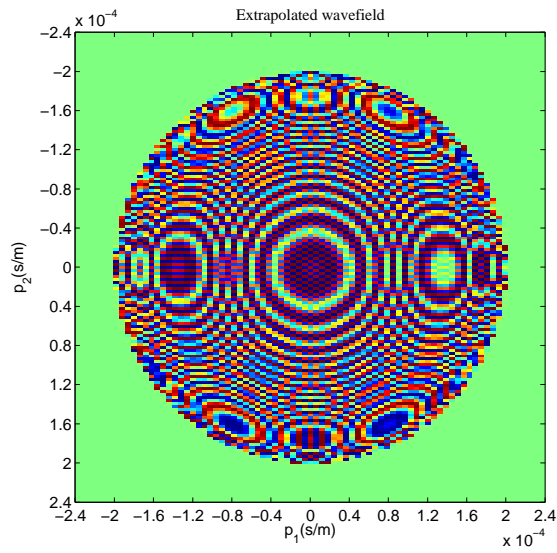
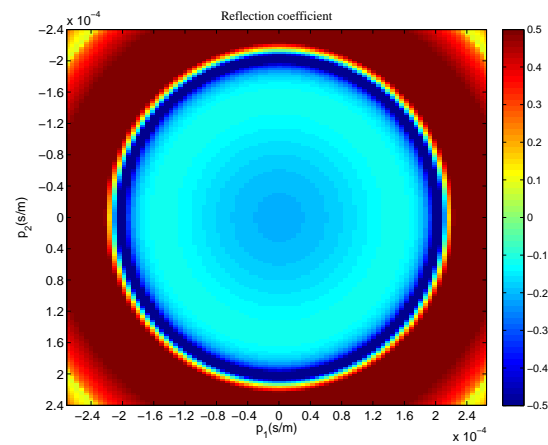


Figure 6.7: The cross-line slices of the extrapolated wavefield using (a) second approach (b) first approach are analogous to each other and demonstrate the authentication of the first approach too.

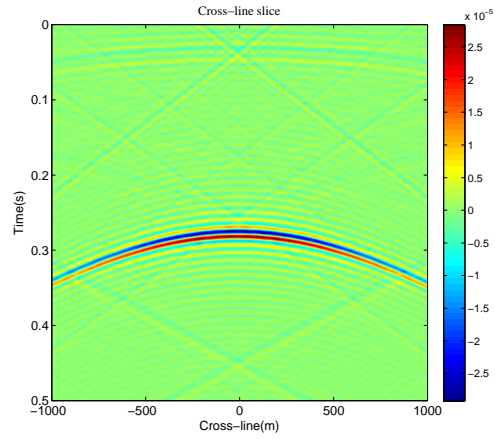


(a)

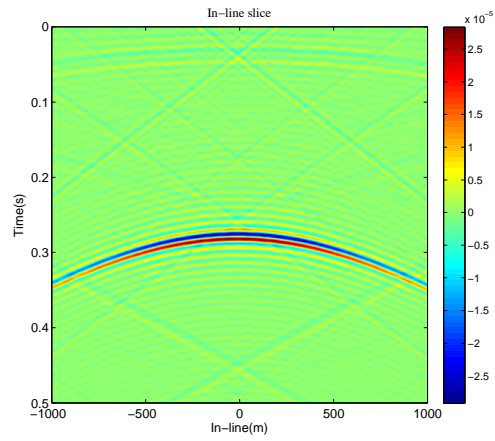


(b)

Figure 6.8: (a) Monochromatic extrapolated wavefield in plane wave domain at the reflector. (b) Monochromatic reflection coefficient as a function of horizontal slowness component.



(a)



(b)

Figure 6.9: (a) Cross-line slice (b) In-line slice of the extrapolated wavefield at the surface before rotation matrix is applied on it. Registered energy decreases with offset.

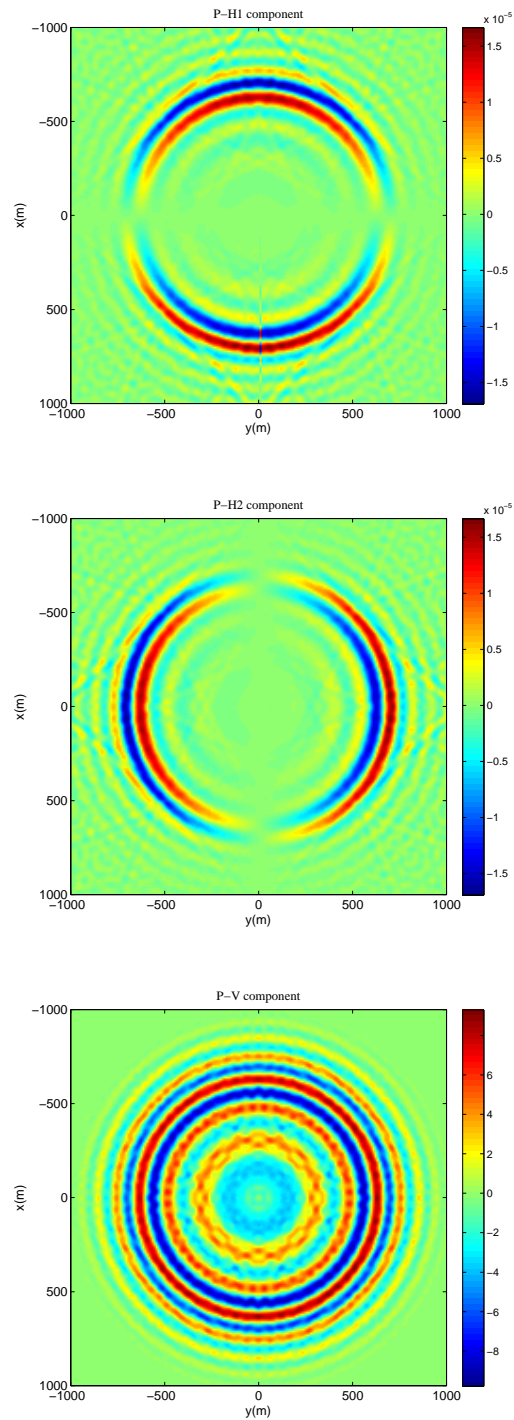


Figure 6.10: (a) Registered energy versus azimuth(REVA) analysis of P-wave at H1 component of $3C$ geophones situated at the surface, indicates that energy registration increases as azimuth increases from 0 to 90. Polarity reversal occur on the either side of a line that bisects the circle along in-line direction. (b) REVA analysis of P-wave at H2 component indicates that energy registration decreases as azimuth increases from 0 to 90. Polarity reversal occur on the either side of a line that bisects the circle along cross-line direction. (c) REVA analysis of P-wave on vertical component reveal the variation of recorded energy and polarity with azimuth.

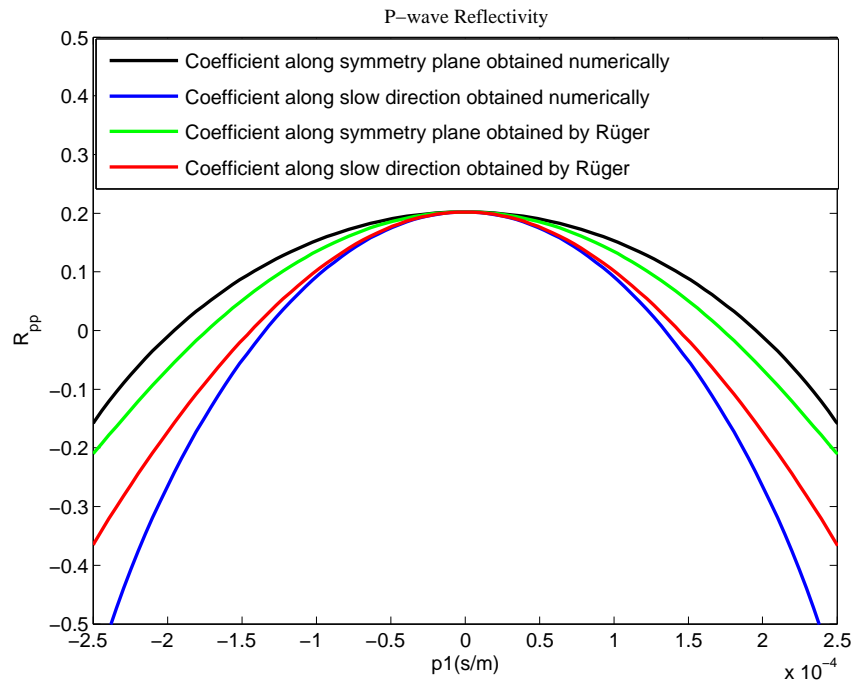


Figure 6.11: The obtained P-wave reflection coefficient along symmetry axis and normal to it. The black and blue colors indicate the results obtained numerically while red and green colors are corresponding to R uger's approach.

Chapter 7

Conclusions

By considering the importance of plane wave domain, I have demonstrated RSM in this domain. For the sake of simplicity, I have illustrated the R coefficient of SH-wave in the plane wave domain by considering isotropic media. The problem associated with the data acquisition geometry has been revealed here. It has been asserted that it is necessary to acquire the data with appropriate geometry for avoiding the wrong interpretation of the target horizon. The way of building the rotation matrix that is applied on the extrapolated wavefield for obtaining the multicomponent data has been represented too. For the case of anisotropy, I have presented $9C-3D$ seismic modelling for VTI media using the first data acquisition geometry. The verification of this modelling has been demonstrated kinematically. I have illustrated the multicomponent surface seismic data for known P-wave source. For doing so, I have shown the way of computing the R and T coefficients in plane wave domain. Additionally, the fidelity of the obtained R coefficient has been illustrated in reference to the R coefficient obtained by using classical methods. The influence of the anisotropy on AVO analysis has been described which makes it necessary to modify the conventional AVO analysis in the presence of anisotropy. For HTI media, initially, the first data acquisition geometry has been considered for performing the proposed modelling that has been verified kinematically and dynamically. Further, in order to obtain multi-component surface seismic data, P-wave has been taken into consideration. This choice resides on the fact that exploration community has been comfortable with P-wave data acquisition and processing. To execute the proposed modelling for obtaining the multi-component data, in case of HTI media, P-wave R coefficient has been calculated numerically and tested in reference to Rüger's approach. Additionally,

two more approaches have been proposed for HTI media in order to avoid the limitation of previously proposed modelling. The fidelity of these approaches has been illustrated in light of physical modelling.

Bibliography

- Aki, K., and Richards, P. G., 1980, Quantitative Seismology Theory and Methods: W.H.Freeman and Co.,San Francisco.
- Anderson, N., and Cardimona, S., 1995, Forward seismic modeling:the key to understanding reflection seismic and ground penetrating radar (gpr) techniques.: Department of Geology and Geophysics, University of Missouri-Rolla, Rolla, MO.
- Benxi, K., Zhenping, T., and Zhao, B., 2009, The application of seismic modeling : Case study from kela 2 gas field in tarim basin, china.: SEG International Exposition and Seventy-Third Annual Meeting.
- Berkhout, A. J., 1982, Seismic Migration: Elsevier.
- Berryman, J., G, 2008, Exact seismic velocities for VTI and HTI media and extended thomson formulas for stronger anisotropies.: Lawrence Berkeley National Laboratory.
- Borejko, P., 1996, R and T coefficients for 3d plane wave in elastic media.: Wave Motion, **24**.
- Cameron, B. W., James, L. B., and Geoffrey, A. K., 1984, Seismic modeling and inversion.: IEEE, **72**.
- Chopra, S., and Stewart, R., 2010, Introduction to this special section: Multicomponent seismic: The Leading Edge.
- Cooper, J. K., Lawton, D., and Margrave, G. F., 2007, Multiples and multimode events in a 2D marine zero offset survey: a physical modelling example: CREWES Research Report, **19**.

- Cooper, J. K., Margrave, G. F., and Maweu, J., 2008, Rayleigh Sommerfeld modelling with AVO: CREWES Research Report, **20**.
- Daley, P., and Hron, F., 1977, Reflection and transmission coefficients for transversely isotropic media.: Bulletin of the Seismological Society of America, **67**.
- Ersoy, O. K., 2007, Diffraction, Fourier optics, and Imaging: Wiley-Interscience.
- Ferguson, R. J., 2009, Geophone rotation analysis by polarity inversion: CREWES Research Report, **21**.
- Ferguson, R. J., and Margrave, G. F., 2008, 3D anisotropic phase shift operators: CREWES Research Report, **20**, 2–4.
- Ferguson, R. J., and Sen, M. K., 2004, Estimating the elastic parameters of anisotropic media using a joint inversion of p-wave and sv-wave travel time error.: Geophysical Prospecting.
- Graebner, M., 1992, Plane-wave reflection and transmission coefficients for a transversely isotropic solid.: Geophysics, **57**.
- Grechka, V., 2009, Application of Seismic Anisotropy in the Oil and Gas Industry.: EAGE.
- Hardage, B. A., 1983, Vertical seismic profiling Part A:Principles, vol. 14A: Geophysical Press, London-Amsterdam.
- Jilek, P., 2002, Modelling and inversion of converted-wave reflection coefficient.: Ph.D. thesis, Colorado School of Mines.
- Kennett, B. L. N., 2001, The Seismic Wavefield: Cambridge.
- Krebes, E. S., 2004, Seismic forward modeling: CSEG Recorder.

- Krebes, E. S., 2008, Seismic Theory and Methods: Course Notes.
- Lines, L., 2004, Fundamental of Geophysical Interpretation: Society of exploration geophysicists.
- Mahmoudian, F., Margrave, G. F., Daley, P. F., Wong, J., and Gallant, E., 2010, Determining elastic constants of an orthorhombic material by physical seismic modeling: CREWES Research Report, **22**.
- Margrave, G. F., and Cooper, J. K., 2007, Seismic modeling in 3D for migration testing: CREWES Research Report, **19**, 5–10.
- Mellmani, G., and Kunzinger, P. A., 1992, Development Geology Reference Manual.: Methods in Exploration.
- Nadri, D., 2009, Non linear estimation of thomson's parameters in transversely isotropic media.: CSIRO Petroleum Resources, –.
- Neufeld, C., and Clayton, C., 2000, Angle rotation in GLSB: Department of Civil and Environment Engineering-University of Alberta.
- Pao, Y. H., Ziegler, F., and Borejko, Y. S. W., 1984, generalized ray integral representation of transient sh in a layered half space with dipping structure.: ACTA Mechanica.
- Perez, M., 2010, Beyond isotropy-part i:a prestack: CSEG Recorder.
- Peter, C., L, and Crampin, S., 1990, Seismic fracture anisotropy in the earth crust: An overveiw: Journal of Geophysical Research., **95**.
- Rüger, A., 1998, Variation of p-wave reflectivity with offset and azimuth in anisotropic media.: Geophysics, **63**.

- Rüger, A., 2001, Reflection Coefficient and Azimuthal AVO analysis in Anisotropic Media.: Society of Exploration Geophysicists.
- Sayers, C., and Chopra, S., 2009, Introduction to this special section: Seismic modeling.: Leading Edge.
- Sharma, R. K., and Ferguson, R. J., 2009a, 9C-3D modeling for vti media.: CREWES Research Report, **22**.
- Sharma, R. K., and Ferguson, R. J., 2009b, R and T coefficients for SH wave in plane wave domain: CREWES Research Report, **21**.
- Shearer, P. M., 1999, Introduction to Seismology: Elsevier.
- Slawinski, M. A., 2003, Seismic Waves and Rays in Elastic Media: Pergamon.
- Sten, S., and Wysession, M., 2002, An Introduction to Seismology, Earthquakes, And Earth Structure: Blackwell.
- Suleiman, A., 2007, A comparison between numerically calculated and formula based scattering coefficient for anisotropic media.: Ph.D. thesis, Univ. of Calgary.
- Thomsen, L., 1986a, Weak elastic anisotropy: Geophysics, **51**, No. 10, 1954–1966, discussion in GEO-53-04-0558-0560 with reply by author.
- Thomsen, L., 1986b, Weak elastic anisotropy: Geophysics, **51**, 1954–1966.
- Thomsen, L., 2002, Understanding Seismic Anisotropy in Exploration and Exploitation: Distinguished Instructor Series, No 5.
- Tsvankin, I., 2001, Seismic Signatures and Analysis of Reflection data in Anisotropic Media.: Handbook of Geophysical Exploration Series.

Upadhyay, S. K., 2004, *Seismic Reflection Processing*: Springer.

Vernik, L., and Liu, X., 1997, Velocity anisotropy in shales: A petrophysical study.: *Geophysics*, **62**.

Xiang-Yangi, L., 1997, Fractured reservoir delineation using multicomponet seismic data.: *Geophysical Prospecting*, **45**.

Yang, J., 2003, Numerical and physical modelling of P-S converted waves in VTI media.: Ph.D. thesis, Univ. of Calgary.

Zheng, X., 2006, Seismic azimuthal anisotropy and fracture analysis from p-p reflection data.: M.Sc. thesis, Univ. of Calgary.

Appendix A

Chapter 2

A.1 To find the value of slowness at which reflected amplitude would be zero

From equation (2.6) reflection coefficient R_{SH} is zero when

$$\rho_1 v_1^2 q_1 = \rho_2 v_2^2 q_2, \quad (\text{A.1})$$

Where, in this example, density (ρ) is the same across the interface. Further, constant ρ simplifies equation (A.1) so that

$$v_1^2 q_1 = v_2^2 q_2, \quad (\text{A.2})$$

Using equations (2.10) and (2.11), replace q_1 and q_2 in equation (A.2) to get

$$v_1^2 [1 - (v_1 p_1)^2] = v_2^2 [1 - (v_2 p_1)^2], \quad (\text{A.3})$$

where we have squared both sides.

Solution p_1 for equation (A.3) corresponds to the ray parameter where R_{SH} is zero,

$$p_1 = \frac{1}{\sqrt{v_2^2 + v_1^2}}. \quad (\text{A.4})$$

A.2 Energy flux for reflected and transmitted waves

Earlier it is seen that the transmission coefficient exceeds 1 at critical slowness. The energy transported by the traveling wave is considered to see how it occurs because energy must be conserved. For a harmonic SH plane wave, the flux of energy per unit wavefront, E , in the direction of propagation is the product of the energy density (energy

per unit area) and the velocity (Sten and Wysession, 2002)

$$E = A^2\omega^2\rho\beta/2, \quad (\text{A.5})$$

where A is the amplitude of wave and ρ is the density of medium. Since welded contact of two medium is considered, there is no energy to be accumulated at the interface. According to law of energy conservation, energy flux of the incident wave would be equal to the reflected and transmitted waves energy fluxes. Energy fluxes for the constituent waves are

$$E_I = \omega^2\rho_1\beta_1 \cos j_1 dx/2, \quad (\text{A.6})$$

for the incident SH wave

$$E_R = R_{SH}^2\omega^2\rho_1\beta_1 \cos j_1 dx/2, \quad (\text{A.7})$$

for the reflected wave, and

$$E_T = T_{SH}^2\omega^2\rho_2\beta_2 \cos j_2 dx/2, \quad (\text{A.8})$$

for the transmitted wave, where an incident wave has unit amplitude, dx is the element of the interface, j_1 , j_2 are the angle of incidence and transmission, respectively. These fluxes satisfy the conservation of energy

$$E_I = E_R + E_T, \quad (\text{A.9})$$

and this expression can be written in terms of the incident, reflected and transmitted energy fluxes as

$$\rho_1\beta_1 \cos j_1 = R_{SH}^2\rho_1\beta_1 \cos j_1 + T_{SH}^2\rho_2\beta_2 \cos j_2, \quad (\text{A.10})$$

In terms of the vertical slowness, equation (A.10) is

$$\rho_1\beta_1^2 q_1 = R_{SH}^2\rho_1\beta_1^2 q_1 + T_{SH}^2\rho_2\beta_2^2 q_2, \quad (\text{A.11})$$

It is seen from in line and cross line slices of the R and T coefficients (Figure 2.4), at zero slowness the reflection and transmission coefficients are -0.25 and 0.75, respectively, while density is the same across the boundary and velocities $\beta_1=1500\text{m/s}$ and $\beta_2=2500\text{m/s}$ are used. To verify this result in terms of energy conservation, q_1 and q_2 are replaced by $1/\beta_1$ and $1/\beta_2$, respectively at zero slowness (normal incidence, $j_1 = 0$ and $j_2 = 0$), and equation (A.11) becomes

$$1 = R_{SH}^2 + T_{SH}^2 \frac{\beta_2}{\beta_1}. \quad (\text{A.12})$$

Using the value of variables used in above equation we get $1 = (-0.25)^2 + (0.75)^2 * 2500/1500$ from equation (A.12) and it reveals that energy is conserved at zero slowness. Now we consider the critical slowness case where reflected and transmitted amplitudes are 1 and 2, respectively. To verify this result the vertical slowness in medium 2, q_2 , is zero ($j_1 = \text{critical}$ and $j_2 = \pi/2$). Recalling the equation (2.7), the transmission coefficient goes to 2 as slowness approaches the critical value but according to equation (A.8), the energy of the transmitted wave vanishes at this slowness because wavefront factor $\cos j_2$ is vanished here. Thus, energy is conserved here also.

Appendix B

Chapter 3

Given the effective ray parameter, we obtain the vertical slowness from the analytic expression (Ferguson and Margrave, 2008) as

$$q_\alpha = 1/2 \sqrt{2\beta_0^{-2} + 2\alpha_0^{-2} - \mathcal{A}SP_I^2 - \mathcal{A}R}, \quad (\text{B.1})$$

and

$$q_{\beta_{SV^-}} = 1/2 \sqrt{2\beta_0^{-2} + 2\alpha_0^{-2} - \mathcal{A}SP_I^2 + 4R}, \quad (\text{B.2})$$

where

$$S = \left(1/2 \frac{\alpha_0^2}{\beta_0^2} + 1/2\right) \epsilon + 1 - \mathcal{I}/2 \frac{\delta \alpha_0^2}{\beta_0^2}, \quad (\text{B.3})$$

and

$$R = \frac{1}{2} 4P_I^4 [S^2 - 2\epsilon - \mathcal{I}] + 4 \left(\frac{P_I}{\beta_0}\right)^2 [2\epsilon - \mathcal{S} + 1] + 4 \left(\frac{P_I}{\alpha_0}\right)^2 [1 - \mathcal{S}] + \beta_0^{-4} + \alpha_0^{-4} - 2(\alpha_0\beta_0)^2, \quad (\text{B.4})$$

The vertical slowness for SH wave can be computed as

$$q_{\beta_{SH^-}} = \frac{1}{\beta_0^2} - P_I^2 [2\gamma + 1]. \quad (\text{B.5})$$

Appendix C

Chapter4

Parameters	Overburden(Shale)	Lower medium(Sand)
V_p (m/s)	3300	4200
V_s (m/s)	1700	2700
$Density(gm/cm^3)$	2.35	2.49

Table C.1: Model parameters for Class 1 AVO

Parameters	Overburden(Shale)	Lower medium(Sand)
V_p (m/s)	2960	3490
V_s (m/s)	1380	2290
$Density(gm/cm^3)$	2.43	2.14

Table C.2: Model parameters for Class 2 AVO

Parameters	Overburden(Shale)	Lower medium(Sand)
V_p (m/s)	2730	2020
V_s (m/s)	1240	1230
$Density(gm/cm^3)$	2.35	2.13

Table C.3: Model parameters for Class 3 AVO

Appendix D

Chapter 5

Using the Thomson's parameters, the following relationship between elastic stiffness constant and Thomson's parameters can be established as

$$c_{11} = \rho \alpha_0^2 (1 + 2\epsilon), \quad (\text{D.1})$$

$$c_{33} = \rho \alpha_0^2, \quad (\text{D.2})$$

$$c_{44} = \rho \beta_0^2, \quad (\text{D.3})$$

$$c_{55} = \rho \beta_0^2, \quad (\text{D.4})$$

$$c_{13} = \rho \frac{\alpha_0^2 - \beta_0^2}{(2\delta + 1)\alpha_0^2 - \beta_0^2} - \rho \beta_0^2. \quad (\text{D.5})$$

For given Thomson's parameters, the elastic stiffness constant can be obtained using above equations. As it's known that the elastic stiffness constant remains real for all physical situations, the obtained value of the elastic stiffness constant c_{13} is complex and violates the physical behavior of the elastic stiffness constants for the large negative value of δ . Thus, this condition leads to the unexpected behavior of the wavefield kinematically as well as dynamically.

D.1 Methodology for obtaining analytic curves

In order to obtain an analytic curve we follow the steps

α_0	β_0	ϵ	δ	γ
2950	1990	0.17	0.09	.14

Table D.1: Thomson's Parameters of a medium considered for P and SH waves propagation.

Model	α_0	β_0	ϵ	δ	γ
1	2950	1990	0.17	0.09	.14
2	3600	2000	0.14	0.08	0.16
3	3340	1860	0.49	0.30	0.59
4	3300	2300	0.58	0.84	0.39
5	3600	2100	0.36	-0.08	0.38
6	3377	1490	0.200	-0.282	0.510

Table D.2: Thomson's Parameters of models considered for SV wave propagation.

- First we define phase angles for a model that is characterized in terms of known Thomson's parameters.
- For known phase angle, we compute phase velocity and derivative.
- Compute group angles from known phase velocities.
- Now fit group angles and phase angles.
- Compute set of phase angles for given group angles.
- Further, compute phase velocity and derivatives based on new phase angles. Then compute group velocity again.
- Define a time(t) for a given depth z as ($t \geq z/\alpha_0$).
- Obtain radius component of polar co-ordinate system.
- For known radius, we compute Cartesian co-ordinate components and draw the analytic curve.

The MATLAB program for obtaining analytic curve is given below

$vp = \alpha_0$; $vs = \beta_0$; $epsilon = \epsilon$; $phi = 0$; $poly = 2$; $ia = 1$;

Define phase angles

$pang = [-pi/2 : 1/180 : pi/2]$;

$[rc] = size(pang)$;

Make matrices of anisotropic parameters

$vp = vp * ones(1, c)$;

$vs = vs * ones(1, c)$;

$\epsilon = \epsilon * ones(1, c)$;

$\delta = \delta * ones(1, c)$;

$\phi = pi * \phi / 180$;

Compute phase velocity

$aa = .5 * (vp.^2) * (1 - (vs./vp).^2)$;

$bb = 4 * \delta ./ (1 - (vs./vp).^2).^2$;

$cc = 4 * \epsilon * (1 - (vs./vp).^2 + \epsilon) ./ (1 - (vs./vp).^2).^2$;

$dd = vp.^2$;

$ee = (vp.^2) * \epsilon$;

$tivp = sqrt(dd * aa * sqrt(1 + bb * (sin(pang).^2) * (cos(pang).^2) + cc * (sin(pang).^4)) -$

$dd * aa + dd + ee * (sin(pang).^2))$;

$D = aa ./ dd * (sqrt(1 + bb * (sin(pang).^2) * (cos(pang).^2) + cc * (sin(pang).^4)) - 1)$;

$tivs = vs * sqrt(1 + \epsilon * (sin(pang).^2) * ((vp./vs).^2) - D * ((vp./vs).^2))$;

Make group angle

$dtivs = (vs * ((2 * \epsilon * vp.^2 * cos(pang) * sin(pang)) ./ vs.^2 + (vp.^2 * (vs.^2 ./ (2 * vp.^2) -$
 $1/2) * ((8 * \delta * cos(pang).^3 * sin(pang)) ./ (vs.^2 ./ vp.^2 - 1).^2 - (8 * \delta * cos(pang) *$
 $sin(pang).^3) ./ (vs.^2 ./ vp.^2 - 1).^2 + (16 * \epsilon * cos(pang) * sin(pang).^3 * (\epsilon - vs.^2 ./ vp.^2 +$
 $1)) ./ (vs.^2 ./ vp.^2 - 1).^2) ./ (2 * vs.^2 * ((4 * \delta * cos(pang).^2 * sin(pang).^2) ./ (vs.^2 ./ vp.^2 -$

```

1).^2 + (4.*ε.*sin(pang).^4.*(ε - ρs.^2./vp.^2 + 1))./(vs.^2./vp.^2 - 1).^2 + 1).(1/2))))./(2.* /
((vp.^2.*(vs.^2./(2.*vp.^2) - 1/2).*((4.*δ.*cos(pang).^2.*sin(pang).^2)./(vs.^2./vp.^2 - 1).^2 +
(4.*ε.*sin(pang).^4.*(ε - ρs.^2./vp.^2 + 1))./(vs.^2./vp.^2 - 1).^2 + 1).(1/2) - 1))./vs.^2 + (ε.*
vp.^2.*sin(pang).^2)./vs.^2 + 1).(1/2));
gang = atand(real(((tand(pang) + dtivs./tivs))./(1 - tand(pang).*dtivs./tivs))));
ind = isnan(gang);
gang(ind) = 90;
fori = 1 : length(gang)/2
if(gang(i) == 90)
gang(i) = -90;
end
end

```

Compute the group velocity

```
tivg = sqrt(tivs.^2 + dtivs.^2);
```

Now fit group angle and phase angle

```
p = polyfit(gang, pang, poly);
```

Compute set of phase angles for given group angles

```
npang = polyval(p, pang);
```

Compute a new vector of phase velocities and derivatives based on new phase angles

```
D = aa./dd.*(sqrt(1 + bb.*sin(npang).^2.*cos(npang).^2 + cc.*sin(npang).^4) - 1);
tivs = vs.*sqrt(1 + epsilon.*sin(npang).^2.*((vp./vs).^2) - D.*((vp./vs).^2));
```

Make group angle

```
dtivs = (vs.*((2.*ε.*ρp.^2.*cos(npang).*sin(npang))./vs.^2 + (vp.^2.*(vs.^2./(2.*ρp.^2) -
1/2).*((8.*δ.*cos(npang).^3.*sin(npang))./(vs.^2./vp.^2 - 1).^2 - 8.*δ.*cos(npang).*
sin(npang).^3)./(vs.^2./vp.^2 - 1).^2 + (16.*ε.*cos(npang).*sin(npang).^3.*(ε - ρs.^2./vp.^2 +
1))./(vs.^2./vp.^2 - 1).^2))./(2.*ρs.^2.*((4.*δ.*cos(npang).^2.*sin(npang).^2)./(vs.^2./vp.^2 -
```

$$\begin{aligned}
& 1)^2 + (4 * \epsilon * \sin(npang)^4 * (\epsilon - vs.^2/vp.^2 + 1)) / (vs.^2/vp.^2 - 1)^2 + 1)^{(1/2)})) / (2 * / \\
& ((vp.^2 * (vs.^2 / (2 * \rho p.^2) - 1/2) * ((4 * \delta * \cos(npang)^2 * \sin(npang)^2) / (vs.^2/vp.^2 - / \\
& 1)^2 + (4 * \epsilon * \sin(npang)^4 * (\epsilon - vs.^2/vp.^2 + 1)) / (vs.^2/vp.^2 - 1)^2 + 1)^{(1/2)} - 1)) / vs.^2 + \\
& (\epsilon * \rho p.^2 * \sin(npang)^2) / vs.^2 + 1)^{(1/2)});
\end{aligned}$$

Compute group velocity

$$tavg = \text{sqrt}(tivs.^2 + dtivs.^2);$$

Define the depth z_1 , time t_1 and compute

$$r = (\text{sqrt}(tivs.^2 * t_1^2 - z_1^2));$$

$$x1 = r * \sin(pang);$$

$$y1 = r * \cos(pang);$$

$$X = [x1 - \hat{x}1];$$

$$Y = [y1 - \hat{y}1];$$

$\text{plot}(Y, X, 'b', 'linewidth', 4)$ (**Impulse response using phase velocity**)

$$r3 = (\text{sqrt}(tavg.^2 * t_1^2 - z_1^2));$$

$$x4 = r3 * \sin(gang);$$

$$y4 = r3 * \cos(gang);$$

$$X3 = [x4 - \hat{x}4];$$

$$Y3 = [y4 - \hat{y}4];$$

$\text{plot}(Y3, X3, 'm', 'linewidth', 4)$ (**Analytic curve**)

Appendix E

Chapter6

The orthorhombic medium considered in Chapter6 is defined as

$$A_{\alpha\beta} = \begin{bmatrix} 12.67 & 6.13 & 6.68 & 0 & 0 & 0 \\ 6.13 & 8.7 & 5.79 & 0 & 0 & 0 \\ 6.68 & 5.79 & 12.67 & 0 & 0 & 0 \\ 0 & 0 & 0 & 2.34 & 0 & 0 \\ 0 & 0 & 0 & 0 & 2.89 & 0 \\ 0 & 0 & 0 & 0 & 0 & 2.28 \end{bmatrix} \quad (\text{E.1})$$

The two HTI media for obtaining the R coefficient are defined as

Parameters	Overburden(Shale)	Lower medium(Sand)
$\alpha_0(\text{m/s})$	5029	3292
$\beta_0(\text{m/s})$	2987	1768
ϵ	0.005	0.195
δ	-0.032	-0.45
γ	0.041	0.10

Table E.1: Model parameters for HTI media

Appendix F

Abbreviation and list of symbols

P-waves: Primary waves known as compressional waves and displace the ground in the direction of propagation. That's why P-waves are longitudinal in nature.

Shear-waves: Secondary waves are known as shear waves. These waves follow P-waves and displace the ground perpendicular to the direction of propagation. If shear waves move medium's particles up and down (perpendicular to the direction of propagation), these are known as SV-waves. SH-waves move medium's particles side to side, perpendicular to the direction of propagation.

VTI: Vertical Transverse Isotropy.

HTI: Horizontal Transverse Isotropy.

Ψ : Source wave-field.

ω : Angular frequency.

R : Reflection coefficient.

T : Transmission coefficient.

$\vec{\mathbf{k}}$: Wavenumber vector.

$\hat{\mathbf{p}}$: Slowness vector.

$\hat{\mathbf{a}}$: Unit vector normal to the interface.

$\vec{\mathbf{n}}$: Unit wavefront normal.

Ψ_0 : Spectra of source wave-field.

$\Psi_{\Delta z}$: Source wave-field at depth Δz .

p_1 and p_2 : Horizontal components of slowness vector.

q : Vertical slowness.

V : Phase velocity.

ρ : Density.

θ_a and ϕ_a : Dip and azimuth of the unit vector normal to the interface.

θ : Propagation or phase angle.

θ_I : Effective angle of incidence.

ϕ : Angle between horizontal projection of slowness-vector and y axis.

θ_1 : Polarization angle.

τ : Stress tensor.

ϵ : Strain tensor.

$\vec{\mathbf{u}}$: Displacement vector.

\mathbf{c} : Fourth rank stiffness tensor.

$\vec{\mathbf{U}}$: Polarization vector.

α_0 : P-wave velocity along the symmetry axis.

β_0 : Shear-wave velocity along the symmetry axis.

ϵ, γ and δ : Thomsens's parameters.

W : Vector source wave-field.

S_1 : In-line component of a source.

S_2 : Cross-line component of a source.

P : Vertical component of a source.

D : Recorded vector wave-field.

H_1 : In-line component of a 3C geophone.

H_2 : Cross-line component of a 3C geophone.

V : Vertical component of a 3C geophone.

ψ : Group angle.

\mathbf{g} : Group-velocity vector.

\mathbf{p} : Phase-velocity vector.

ϵ^V, δ^V and γ^V : Thomsen's parameters of an equivalent VTI media for HTI media.